



“Characterization and Application of Aromatic Self-Assembled Monolayers”

Thesis  
To award Ph.D in physics

Supramolecular system  
Faculty of Physics  
University of Bielefeld

Submitted by  
Mohamed El-Desawy

June 2007

## In the name of Allah, Most Gracious, Most Merciful

“Soon will We show them our Signs in the (furthest) regions (of the earth), and in their own souls, until it becomes manifest to them that this is the Truth. Is it not enough that thy Lord doth witness all things?”

Holy Qur'an

Detailed (Fussilat)-Sura 41

## **Dedication**

I dedicate this work to my father, my wife and my daughters, Toka and Naira. I am thankful for their love, patience, understanding, and support.

## Table of contents

|  |    |
|--|----|
| Chapter 1 Introduction.....  | 7  |
| Chapter 2 Analytical techniques.....                                     | 14 |
| 2-1 X-ray Photoelectron Spectroscopy.....                                | 14 |
| 2-2 Atomic Force Microscopy.....   | 22 |
| 2-3 Proximity printing.....  | 26 |
| 2-4 Scanning Electron microscopy.....                                    | 28 |
| Chapter 3 Experimental aspects.....                                      | 30 |
| 3.1 Materials.....   | 30 |
| 3.1.1 Substrates.....  | 30 |
| 3.1.2 Laboratory Equipment.....  | 30 |
| 3.1.3 Substrate cleaning .....   | 31 |
| 3.1.4 Chemicals.....   | 33 |
| 3.2 Sample preparation.....  | 34 |
| 3.3 XPS measurements.....  | 37 |
| 3.4 Low electron energy irradiation.....                                 | 39 |
| 3.5 Heating Samples.....   | 40 |
| 3.6 AFM measurements.....  | 40 |
| Chapter 4 E-beam lithography of HBP.....                                 | 42 |
| Chapter 5 Thermal stability of aromatic SAMs.....                        | 46 |
| Section A: Thermal stability of pristine BPT and ODT.....                | 47 |
| 1-Characteristic of pristine BPT film.....                               | 47 |
| 2- Pristine BPT as function of Temperature.....                          | 49 |
| 3- ODT as function of Temperature.....                                   | 52 |
| Section B: Thermal stability of cross-linked BPT.....                    | 56 |
| 1-Characteristic of cross-linked Biphenylthiol film.....                 | 56 |
| 2-Cross-linked BPT as function of Temperature.....                       | 56 |
| 3-Thermal desorption lithography.....                                    | 62 |
| Section C: Thermal stability of pristine and cross-linked NBPT.....      | 65 |
| 1-Characteristic of pristine NBPT as a function of temperature.....      | 65 |
| 2- Characteristic of cross-linked NBPT as a function of temperature..... | 74 |

|  |    |
|--|----|
| Chapter 6 High-affinity protein chip fabrication by chemical e-beam nanolithography..... | 78 |
| 1-Introduction.....  | 79 |
| 2-XPS measurements.....  | 82 |
| 3-AFM measurements.....  | 89 |
| Summery.....   | 92 |
| References.....  | 93 |

## **Chapter 1**

### ***Introduction***

#### **1.1 Self-Assembled Monolayers**

The interactions between molecules and surfaces are some of the most exciting and widely studied aspects of modern surface science<sup>[1]</sup>. The strengths of the interactions between molecules and substrates are highly dependent upon their chemical natures, ranging from very weak (e.g., n-alkanes adsorbed on gold or graphite<sup>[2]</sup>) to strong enough to break chemical bonds within the molecule (e.g., ethylene on platinum<sup>[3]</sup>). One of the most remarkable molecule–substrate interactions is the spontaneous self organization of atoms and molecules on surfaces into well-ordered arrays; the supramolecular assemblies that form often possess both short- and long-range order. In particular, the spontaneous organization (self-assembly) of surfactant molecules adsorbed on transition metal surfaces has been of growing importance over the past two decades. The field of self-assembly has grown rapidly since the discovery of these structures and their ability to modify the physical and chemical properties of a surface.

In a general sense, self-assembled monolayers can be defined as well-ordered and oriented organic molecular films formed spontaneously upon a substrate<sup>[4]</sup> (Fig.1). The respective molecules consist of three units: a surface-active head group which binds strongly to the substrate, a specific functional tail group that constitutes the outer surface of the film and modifies bulk surface properties, and a chain or backbone that connects the head and tail groups. It is well known that the lateral density and structure of self-assembled monolayers are the result of a delicate interplay between the substrate-adsorbate interactions, the nonbonded interactions between adsorbate – electrostatic and Van der Waals forces, – and the intramolecular interactions such as bond stretches, angle bends, and torsions. Tail groups can also affect the self-assembled monolayers' structure significantly, providing it has a strong polar

characteristic or is sufficiently large. The process to prepare self-assembled monolayers is simple and only minimum amounts of organic molecules are needed. The flexibility to design self-assembled monolayers with various functional tail groups to accomplish desired surface properties and to possibly control the structure in the nanometer regime is an attractive feature of self-assembled monolayers. These features created significant research activity in the area of self-assembled monolayers, and progress in the understanding of these self-assembled monolayers on a microscopic level has advanced significantly since the 1980s<sup>[3]</sup>.

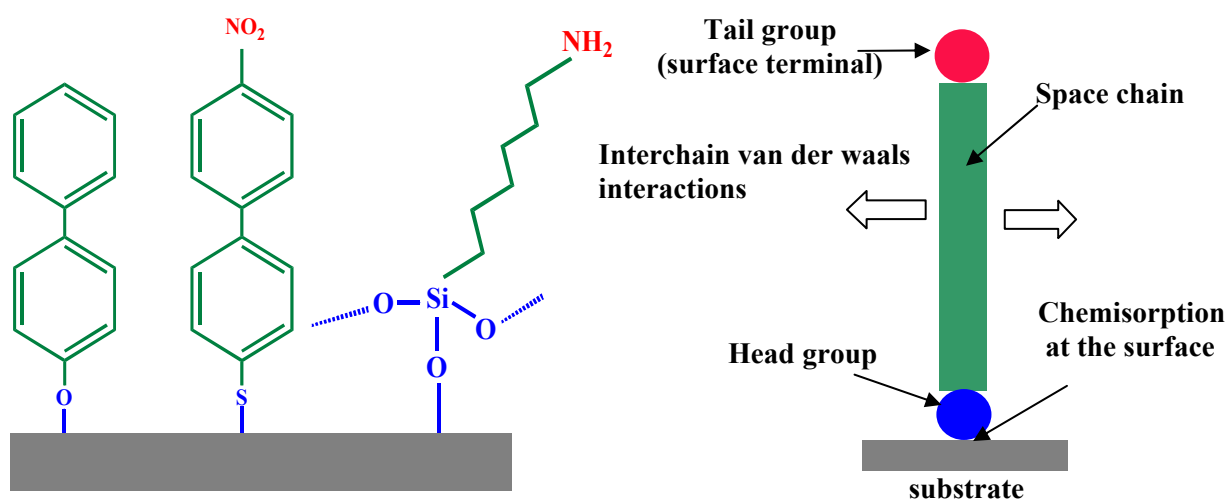


**Figure1.** Schematic of Self-assembled monolayer

There are several types of SAMs that have been synthesized and studied in detail. These include organosilicon on oxidized surfaces (SiO<sub>2</sub> on Si, Al<sub>2</sub>O<sub>3</sub> on Al, glass, etc.); alkanethiol on Au, Ag, and Cu; alcohols and amines on Pt; dialkyl sulfides and dialkyl disulfides on Au; and carboxylic acids on Al<sub>2</sub>O<sub>3</sub> and Ag<sup>[4]</sup>. Recently, self assembled monolayers of aromatic thiols have also attracted attention and became very popular<sup>[5-19]</sup>.

Pattern generation with self-assembled monolayers<sup>[5,20]</sup> has attracted growing in order to understand the fundamental interactions and organization of mixed monolayers on surfaces, but an additional reason for patterning SAMs is to create functional nanostructures completely or in part from the “bottom up”. Using

particular chemical functional groups or using mixed component SAMs, features of interest such as nanoparticles, cells, proteins, or other biomolecules can be patterned for the creation of higher-ordered structures and architectures if they possess particular affinities for parts of the SAM. Many techniques have been employed to fabricate lateral patterned SAMs, among them UV lithography<sup>[21]</sup>, ion lithography<sup>[22]</sup>, microcontact printing<sup>[23]</sup>, and scanning probe lithography,<sup>[24,25]</sup> as shown in Fig.2.

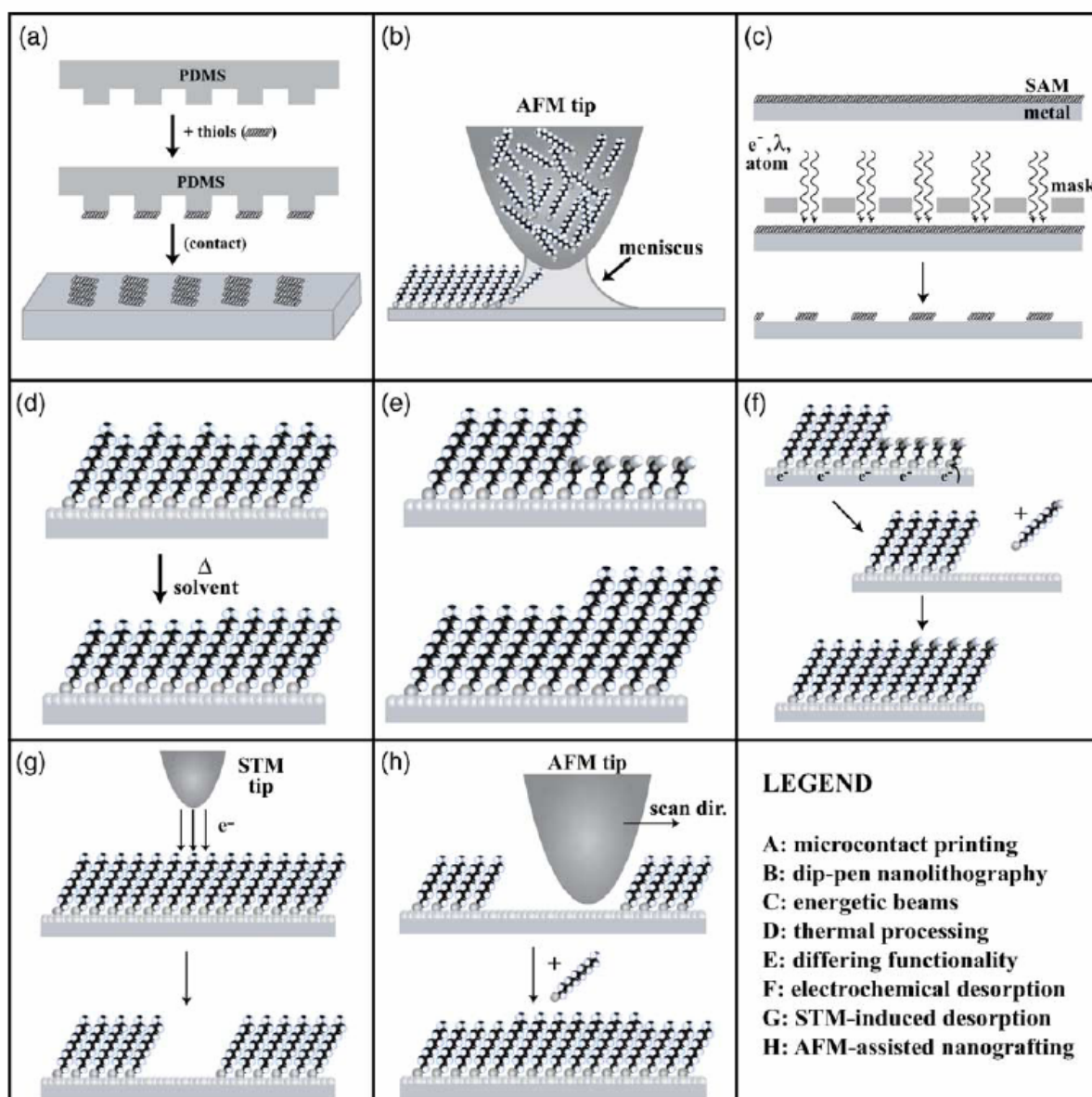


**Fig.2.** Schematics of several techniques employed to pattern SAMs<sup>[1]</sup>

Among them electron-beam (e-beam) lithography<sup>[26-29]</sup> is a powerful and practical tool for nanoscale SAM patterning. In e-beam lithography the achievable resolution is usually not limited by the focus of the e-beam but by secondary processes, such as forward scattering and proximity effects. E-beams can be focused into very small spots (<3nm) and e-beam lithography can produce precisely aligned patterns and is easily combined with other micro fabrication techniques. The response of SAMs to electrons can be controlled by specifically tailoring the self-assembling molecules<sup>[29]</sup>. The electron induced reactions of aliphatic and aromatic SAMs show distinct differences. In case of aliphatic<sup>[30-32]</sup> SAMs the electron induce the cleavage of C-H bonds , which leads to orientation and conformation disorder of the chains, the desorption of material, and the formation of C=C double bonds in the fragments remaining on the surface and can be used as positive resists<sup>[29,33,34]</sup>. In case of aromatic SAM , electron cleavage C-H bonds for and neighbouring aromatic units form a cross-linked overlayer on the surface and can be used as negative resists<sup>[35,29]</sup>. In case of nitobiphenylthiol (NBPT) not only cross-linking of the aromatic units, but also their terminal nitro groups are converted to the amino groups<sup>[36]</sup> as shown in Fig.3.

Self-assembled monolayers (SAMs) on metallic surfaces have been intensively studied as model systems for potential use in different applications such as surfaces lubrication<sup>[37,38]</sup>, corrosion protection<sup>[39-43]</sup>, wetting<sup>[44-46]</sup>, micro-/nanolithography and biomedical, and microelectronic devices<sup>[47]</sup>. However, because of their poor stability, their technological applications are still limited. The mostly studied alkanethiol-based SAMs decompose up on heating temperatures above 353 K<sup>[48]</sup>.

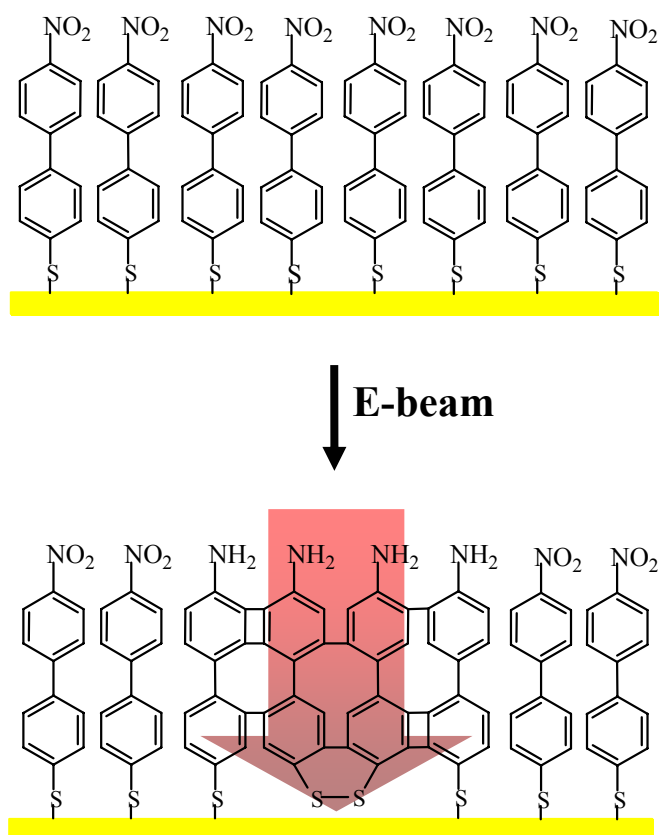


**Fig.3.** Schematic representation of NBPT SAM and e-beam induced cross linking

To improve the thermal stability, different approaches have been tested destined to enhance both the lateral stability within SAMs and their coupling to substrates. Examples include lateral polymerization<sup>[49]</sup> or hydrogen bonding<sup>[50]</sup>, multiple sulfur-substrate coupling,<sup>[51]</sup> underpotential metal deposition,<sup>[52]</sup> and the utilization of more rigid aromatic SAMs.<sup>[5]</sup> Nevertheless, only a moderate increase of the thermal stability was achieved, showing thermal decomposition and desorption of the monolayers in the range from 373 to 473 K.

## 1.2 Immobilization of protein on cross-linked SAMs

The cross-linked biphenyl SAMs were used as ultrathin (1.2 nm) negative resists for structuring of gold<sup>[29,35]</sup> and silicon substrates<sup>[53]</sup>, and have such a high stability, that they even could be organized to free-standing nanosheets.<sup>[54]</sup> The generated well-ordered templates of amino groups can be used for specific covalent coupling of biomolecules using various spacer molecules<sup>[55]</sup>. This novel technology enables tethering of molecules at specific sites on nanostructure surfaces down to lateral dimensions of 20 nm<sup>[56-58]</sup>. An affected experiment was covalent coupling of streptavidin to the amino groups of these cross-linked SAMs<sup>[55]</sup>.

Systematic approaches to explore the plethora of protein-protein interactions and myriads of dynamic protein networks are at the forefront of biological sciences. Highly parallel protein chip technologies deliver promising tools for this challenge even down to single molecule level.<sup>[59,60]</sup> Whereas DNA molecules are exceptional robust and easy to immobilize in a functional manner – as seen in the triumph of DNA chip technology<sup>[61]</sup> proteins are highly sensitive and chemical heterogeneous entities denaturing rapidly *in vitro*.

Using multivalency as a design principle, a chemical recognition unit with exceptionally high affinity for proteins was designed, while maintaining their functionality<sup>[62]</sup>. These multivalent chelator heads consist of nitrilotriacetic acid (NTA) moieties, which provide chemical recognition for histidine-tagged proteins by complexation of transition metal ions, e.g. Ni(II). A tris-NTA unit coordinates six imidazole moieties and thus perfectly matches the coordination demands of a hexahistidine tag with binding affinities in the nanomolar range<sup>[63]</sup>. For the generation of protein arrays, the application of a lithography step is necessary. Chemical e-beam nanolithography is an efficient method for controlled attachment of molecules and molecular complexes at various surfaces (e.g. metals, silicon, indium tin oxide).

In this thesis, chapter 2 gives a brief description of the analytical techniques used in this work, putting emphasis on the theoretical background. Chapter 3 describe the experimental detail, including sample preparation, heating procedure, experimental setups, and measurement protocols. Chapter 4 present the sensitivity of hydroxybiphenyl (HBP) to irradiation dose. Chapter 5 investigate the thermal stability of the pristine and cross-linked aromatic Biphenylthiol(BPT) and nitrobiphenylthiol(NBPT) SAMs using in situ UHV XPS/SEM and ex-situ AFM . To show what temperature can withstand these monomolecular film. Also, to study desorption mechanisms of pristine aromatic SAM and to compare this with the results for classical alkanethiol SAMs. Finally, to study the ability of temperature processing of e-beam patterned aromatic SAMs yields molecular surface nanostructures.

Chapter 6 present a novel approach to the fabrication of functional protein chip by the combination of electron induced chemical lithography with aromatic SAMs and His-tag/multivalent chelator techniques.

## Chapter 2

### *Analytical techniques*

#### **X-ray photoelectron spectroscopy (xps)**

Surface scientists have long used XPS to obtain information about the composition of materials<sup>[64]</sup>. X-ray photoelectron spectroscopy based on the photoelectric effect<sup>[65]</sup> was developed in the mid 1960s by K. Siegbahn and his research group. For his work in XPS K. Siegbahn was awarded the Nobel Prize for physics in 1981. X-ray photoelectron spectroscopy is conceptually very easy to understand. When a sample is placed within a beam of X-ray, photoelectrons are ejected from the atoms within the material. X-rays have enough energy to eject electrons from the core orbitals of all atoms as shown in Fig.2-1. By dispersing the ejected electrons according to energy, a spectrum of binding energies is obtained.

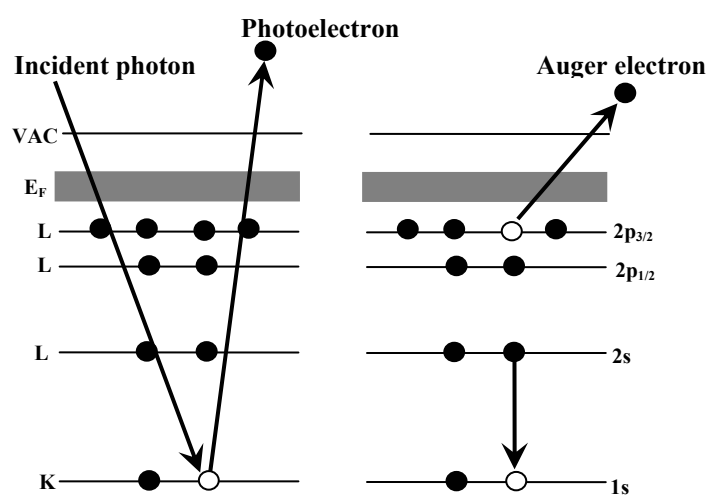
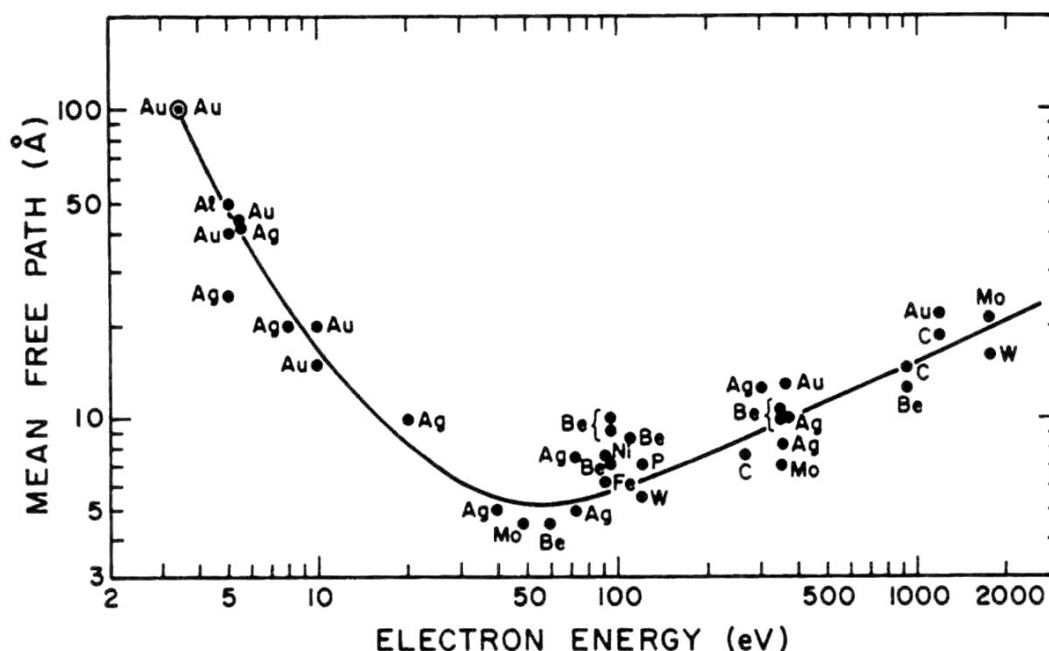


**Fig. 2-1.** X-ray photoemission and Auger electron emission

The locations of peaks in the XPS spectrum indicate both the presence of specific elements and their respective oxidation states. Furthermore, the binding energy of core electrons is very sensitive to the chemical environment of the corresponding element. When the same atom is bonded to a different chemical species, this leads to a change in the binding energy of its core electrons. The variation of binding energy results in a shift of the corresponding XPS peak. This effect is termed as chemical shift, which can be applied to study the chemical status of all elements in the surface. Therefore, XPS is also known as electron spectroscopy for chemical analysis (ESCA). The intensity of photoelectron peak varies with the surface concentration of the corresponding element, allowing quantitative determination of the composition of the surface.

Many applications of XPS for the study of the surface structure can be attributed to its extreme surface sensitivity, typically sampling the top~ 50-100 Å of the material. This is a direct consequence of the short mean free path (5~20 Å, as shown in Fig.2-2) of the low energy electrons through the sample.



Although the X-ray themselves penetrate quite deeply into a material, the resulting photoelectrons can only escape from roughly the first 4 nm. For Self-assembled monolayers, which typically less than 3nm thick the entire monolayer can easily be probed.

There are different X-ray sources. **Non-monochromatic** sources utilise the  $K\alpha$  radiation from Aluminium (Al) and Magnesium (Mg). The energy of  $AlK_{\alpha}$  lines is 1486.6 eV and  $MgK_{\alpha}$  1253.6 eV<sup>[66]</sup>. When the X-ray source is non-monochromatic, the output consists of a broad continues distribution (Bremsstrahlung radiation) with much higher intensity at characteristic line  $K\alpha_{1,2}$  and there are weaker satellite lines  $K\alpha_{3,4}$  and  $K\beta$ .

Al  $K\alpha$  radiation can be **monochromatic** by using quartz crystals. This allows the energy spread of the exciting radiation to be significantly reduced. At the same time, all satellite lines and the Bremsstrahlung radiation are removed, producing a cleaner spectrum with reduced background intensity.

Fig.2-3, shows the energy level diagram applying to XPS. The binding energy ( $E_B$ ) of an electron of the core level is most simply related to the kinetic energy ( $E_{kin}$ ) of the ejected photoelectron by

$$E_B = h\nu - E_{kin} - e\phi_{sp} \quad 2-1$$

where  $h\nu$  is the X-ray energy and  $e\phi_{sp}$  is the work function of the spectrometer.

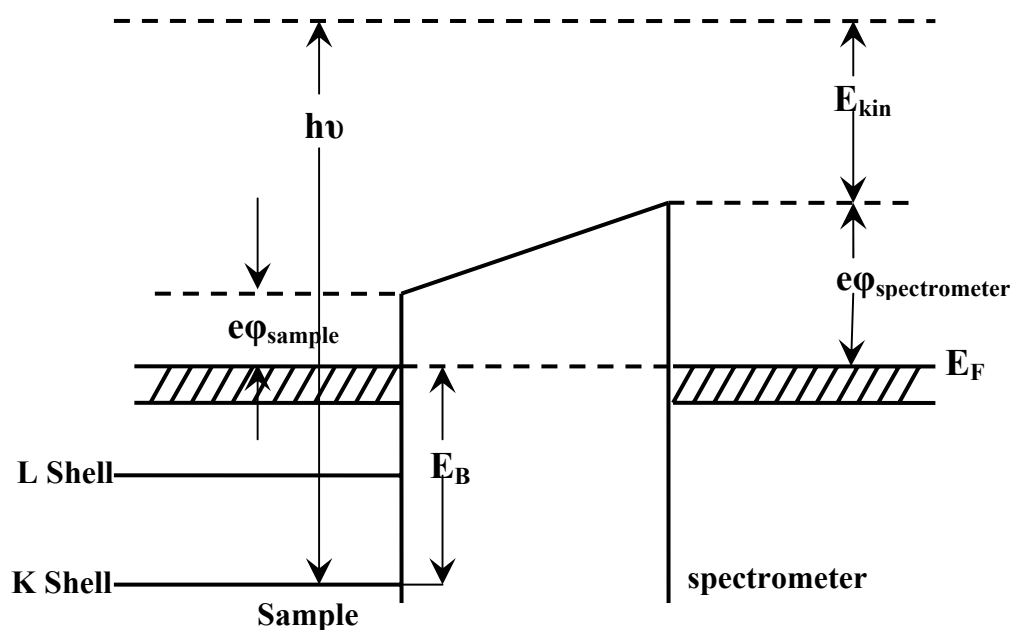


**Fig. 2-3.** Energy level diagram for the XPS process.  $e\phi_{\text{spectrometer}}$ ,  $e\phi_{\text{sample}}$  are the work function of the spectrometer and the sample, respectively.

### The X-ray photoelectron Spectrum

Equation 2-1 assumes that the photoemission process is elastic. Thus each characteristic X-ray will give rise to a series of photoelectron peaks which reflect the discrete binding energies of the electrons present in the solid. Thus at binding energy close to zero, the closely-spaced valence band appear and with increasing binding energy the increasingly tightly-bound core levels. The core levels have variable intensities and widths and non-s-levels are doublets. The doublets arise through spin-orbit ( $j-j$ ) coupling. Two possible state characterized by the quantum number  $j$  ( $j=l+s$ ) arise when  $l>0$  as shown in table 1. Finally the decay of core holes resulting from photoemission can give rise to Auger electron emission and the appearance of Auger peaks.

**Table 1.** Spin-orbit splitting parameters

| Subshell | l | S         | j=l+s      | Area ratio (2j+1) |
|----------|---|-----------|------------|-------------------|
| s        | 0 | $\pm 1/2$ | j=1/2      | -                 |
| p        | 1 | $\pm 1/2$ | j=1/2, 3/2 | 1:2               |
| d        | 2 | $\pm 1/2$ | j=3/2, 5/2 | 2:3               |
| f        | 3 | $\pm 1/2$ | j=5/2, 7/2 | 3:4               |

### Quantitative analysis:

The intensity of the XPS signal derived from a particular core level of a homogeneous sample can be expressed as following:

$$I_A = \sigma_A D(E_A) \int_{\gamma=0}^{\pi} \int_{\varphi=0}^{2\pi} L_A(\gamma) \int_x \int_y J_0(x,y) T(x,y,\gamma,\varphi,E_A) \int_z N_A(x,y,z) \exp\left[-\frac{d}{\lambda_A(E_A)} \cos\theta\right] dz dx dy d\varphi d\gamma \quad 2-2$$

$\sigma_A$  is the photoionization cross section and Fig.2-4 shows the cross section calculated by Scofield for many core lines using Al K $\alpha$  radiation.,  $D(E_A)$  is the detection efficiency for each electron transmitted by the electron spectrometer,  $L_A(\gamma)$  is the angular asymmetry of the emitted intensity with respect to the angle ( $\gamma$ ) between the the direction of incidence x-ray and the analyzer,  $\varphi$  is the azimuthal angle,  $J_0(xy)$  is the flux of the X-ray characteristic line per unit area at point (x,y) on the sample surface,  $T(x,y,\gamma,\varphi,E_A)$  is the transmission of the electron analyser, and  $N_A(x,y,z)$  is the density of atoms A at position (x,y,z). If the spectrometer has small entrance aperture and if

the sample is uniformly illuminated and  $J_0$  became constant, then the equation 2-2 simplifies to

$$I_A = \sigma_A \cdot N_A \cdot L_A(\gamma) \cdot T(E_A) \cdot \lambda_A(E_A) \cdot \cos \theta \quad 2-3$$

The angular asymmetry  $L_A(\gamma)$ , which describes the intensity distribution of the photoelectrons ejected by unpolarized X-rays from atoms or molecules, is given<sup>[67]</sup> by

$$L_A(\gamma) = 1 + \frac{1}{2} \beta_A \left( \frac{3}{2} \sin^2 \gamma - 1 \right) \quad 2-4$$

where  $\beta_A$  is a constant for a given subshell of a given atom and X-ray photoelectron. Fig. 2-5 shows the  $\beta$  values for Al  $K\alpha$  radiation.

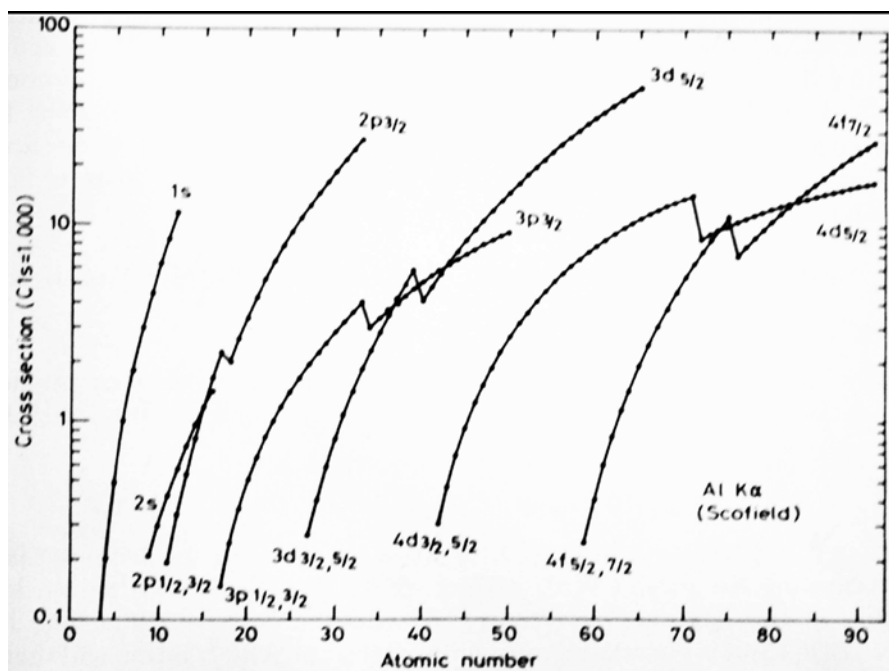


**Fig.2-4.** Calculated values of the cross section  $\sigma_A$  for Al  $K\alpha$  radiation in terms of the C1s cross-section<sup>[68]</sup>.

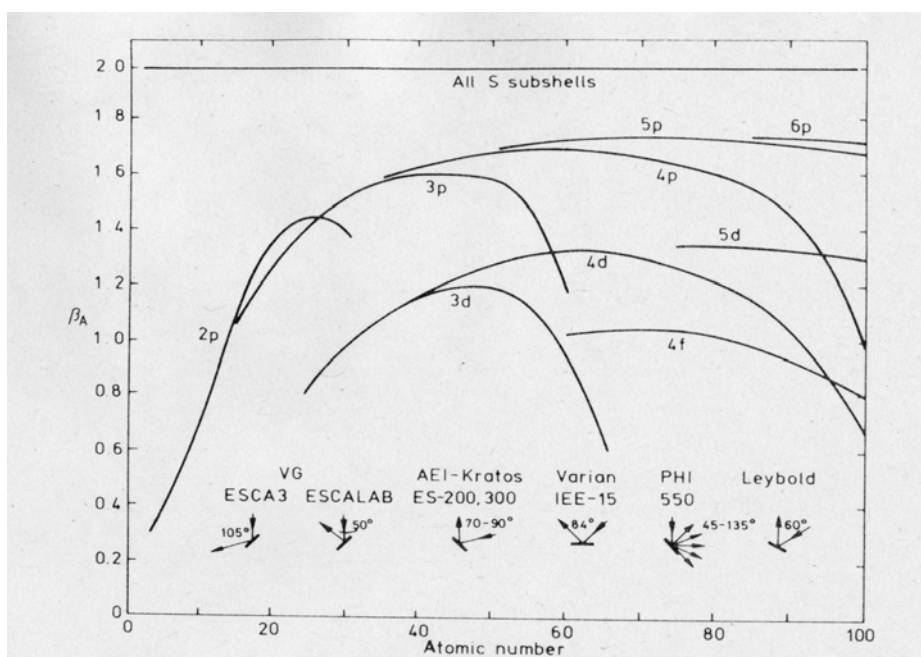


Fig. 2-5 . Calculation values of  $\beta_A$  .from Reilman et al.

### Thickness and Stoichiometric determination

The attenuation of the substrate signal by the adsorbate overlayer can be used to determine the thickness  $d$  of the overlayer according to the equation<sup>[69]</sup>

$$I_d = I_0 e^{-\frac{d}{\lambda \cos \theta}} \quad 2-5$$

Where  $I_0$  and  $I_d$  are XPS signals from the clean and adsorbate-covered substrate, respectively. In accordance with Equation 2-5, we calculate the thickness  $d$  as

$$d = -\lambda \cos \theta \ln \left( \frac{I_d}{I_0} \right) \quad 2-6$$

Most samples are homogeneous monolayers on bulk substrates,  $I_0$ ,  $I_d$  and  $\lambda$  in equation 2-6 can be obtained by experiments. Thus, the thickness of the monolayer can be determined.

In order to determine the stoichiometry, the monolayer film can be computed with two different models. With defined well ordered film, the stoichiometric relationship can give by

$$\frac{N_A}{N_B} = \frac{I_A}{I_B} \cdot \frac{\sigma_B}{\sigma_A} \cdot \frac{L_B(\gamma)}{L_A(\gamma)} \cdot \frac{d_A}{\lambda_A \cos \theta} \cdot \left[ \frac{\exp\left(\frac{-d_A}{\lambda_B \cos \theta}\right)}{\left(1 - \exp\left(\frac{-d_A}{\lambda_A \cos \theta}\right)\right)} \right] \quad 2-7$$

for unknown systems the statistic model is used, with a homogeneous distribution of two elements A and B on a substrate, then

$$\frac{N_A}{N_B} = \frac{I_A}{I_B} \cdot \frac{\sigma_B}{\sigma_A} \cdot \frac{\lambda_B}{\lambda_A} \quad 2-8$$

## Atomic force microscopy (AFM)

The atomic force microscope (AFM) has become a powerful tool for surface observation and investigation of nanomaterials. The AFM was developed 21 years ago<sup>[70]</sup> and is an instrument which probes the interaction forces between a sharp tip and the surface of the sample. AFM gives real space images with high resolution not only in air or in vacuum but also in liquid<sup>[71-74]</sup> including electrolytes or biological solutions<sup>[75,76]</sup>. The ability of this microscope to achieve high resolution in liquids and to probe the mechanical properties of the sample at a nanometre scale makes this instrument increasingly interesting for studies of biological specimens.

### Working principle

The principle of the AFM is simple: a sharp tip fixed at the end of a flexible cantilever is raster-scanned over the surface of the sample. As the tip interacts with the surface, the cantilever deflects and its deflections are measured using a laser spot reflected from the top of the cantilever into an array of photodiodes to reconstruct the topography of the sample<sup>[77]</sup> as shown in Fig 2-5.

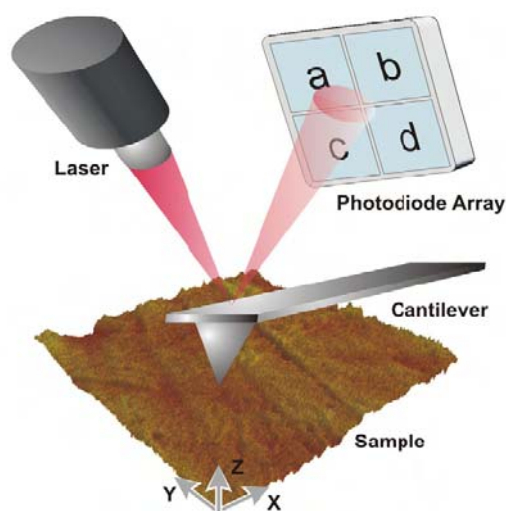


**Fig. 2-5.** Schematic representation of an atomic force microscope.

AFMs use one of two basic types of scanning mechanism: there are some that scan the sample, and the others that scan the tip. Both however, rely upon piezoelectric transducers

### **Imaging modes**

Depending on the sign of the interaction between the tip and the sample, the AFM can work in two different modes, repulsive (contact mode) or attractive (noncontact mode) as shown in Fig 2-6

#### **Contact mode.**

Contact mode imaging is obtained if the tip is operated at the repulsive part of a Lennard-Jones type potential as shown in Fig.2-6. Topography data can be collected in two ways with this mode. a) In **constant force mode**, where the tip scans the sample and the feedback loop keeps the cantilever deflection constant. b) In **constant height mode**, where the cantilever is held at the same height during the scan with the feedback off. The topography of the sample is obtained by monitoring the cantilever deflection.

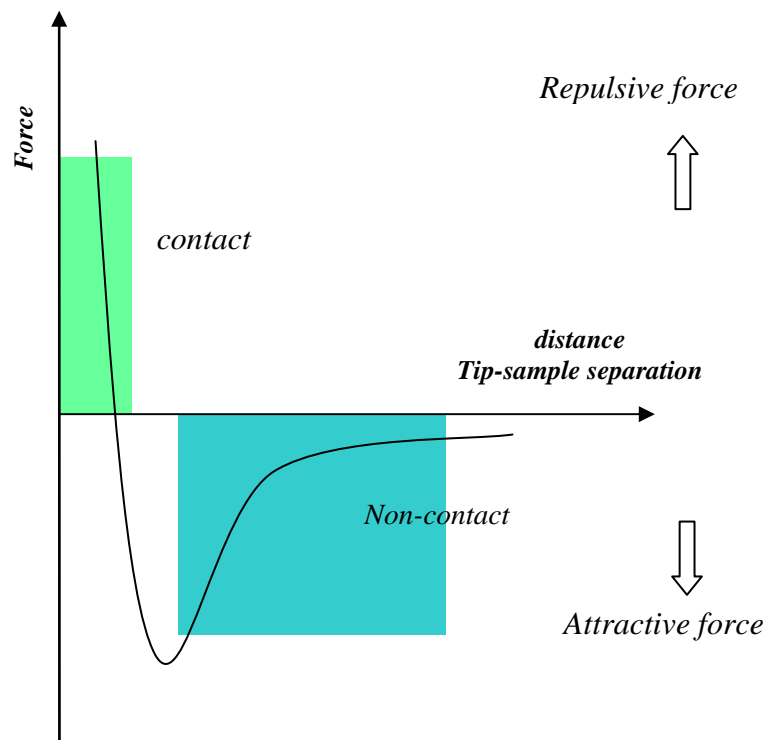


**Fig.2-6:** A Lennard-Jones-type potential. The AFM will operate in the attractive or the repulsive mode, depending on the part of the curve the AFM tip is held.

### **Lateral Force Microscopy (LFM)**

When the cantilever is scanned over the sample in contact mode, a lateral (fractional) force parallel to the surface is observed. The difference signal between top two and bottom quadrants in segment photodiode (see Fig.2-5) is needed to determine the vertical cantilever deflection. When scanning an area of the sample with a frictional component, the AFM tip is deformation in its motion by lateral force, so twisting of the cantilever occurs and the friction is detected. Variation in surface friction can arise from inhomogenities in the surface materials, or from any edge-enhanced surfaces. AFM and LFM data can be collected simultaneously.

## Non-contact mode

The cantilever in this case is oscillated at or close to its resonant frequency at a distance of 1-10 nm above the sample. The relatively long range Van der Waals attractive force (Fig. 2-6) induce changes in the amplitude, phase and resonance frequency of the cantilever. The forces involved in the noncontact mode are much lower than those in contact mode, therefore it is possible to image softest samples without damage.

## Tapping mode

**In air:** The purpose of using this mode is to prevent the AFM tip from being trapped by the capillary force caused by the extremely thin film of water surrounding samples in air. In this mode, the cantilever is also oscillated above the sample but the tip periodically touches the surface. It is a compromise between the non-contact and contact modes. It allows scanning soft fragile materials with better resolution than in the non-contact regime, but with less interaction between the cantilever tip and the material surface. It has been extensively applied to biological system.

**In liquid:** In this case there is no capillary force to cause imaging difficulties because the sample is immersed under liquid. Operating an AFM with the sample under liquid has many advantages. First, the samples can scan with lower forces under liquid because some of the force acting between the tip and the sample are reduced<sup>[27,28]</sup> -disruptive influence of the lateral force- or eliminated<sup>[75]</sup> - adhesion force due to the water film on the sample-. Secondly, allows samples that are normally found in liquid environments to be imaged in their natural states.

## Proximity printing

Many techniques have been employed to fabricate lateral patterned SAMs. A powerful and practical tool for nanoscale SAM patterning is electron-beam (e-beam) lithography<sup>[26-29]</sup>. In e-beam lithography the achievable resolution is usually not limited by the focus of the e-beam but by secondary processes, such as forward scattering and proximity effects. E-beams can be focused into very small spots (< 3nm) and e-beam lithography can produce precisely aligned patterns and is easily combined with other micro fabrication techniques.

The proximity printing<sup>[57]</sup> with low energy electrons ( $\leq 1\text{kV}$ ) is a parallel patterning technique in which a stencil mask is laid directly over a sample that is irradiated with an electron flood gun. Fig.2-7 shows a schematic view of the irradiation chamber for proximity printing. This technique is well suited for the fast fabrication patterns of large areas when no alignment with other structure is required.

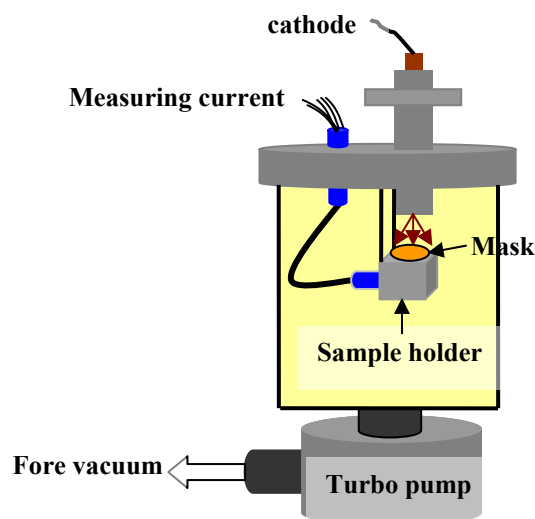


**Fig.2-7.** Scheme diagram of irradiation chamber.

Basically, the resolution of the pattern is limited by the size of the holes in the masks. Generally, low energy electron proximity printing is performed in high vacuum systems at a base pressure of  $10^{-7}$  mbar. The electrons are generated with a flood gun (Specs type 15/40) placed approximately 4 cm above the sample, as shown in Fig 2-7. The irradiation dose  $D$  can be calculated from the equation

$$D = \frac{I \cdot t}{A}$$

$I$  is measured current,

$t$  is the time

$A$  is the area of faradycup

## Scanning Electron Microscopy (SEM)

The scanning electron microscopy (SEM) provides the investigator with a highly magnified image of the surface that is very similar to what one expects if one could actually see the surface visually. The resolution of the SEM can approach a few nm and it can operate at magnifications from 10x – 1000000x

### Physical Basis of operation

In the SEM electrons are focused into a fine probe that is raster over the surface of the sample, Fig.2-8.

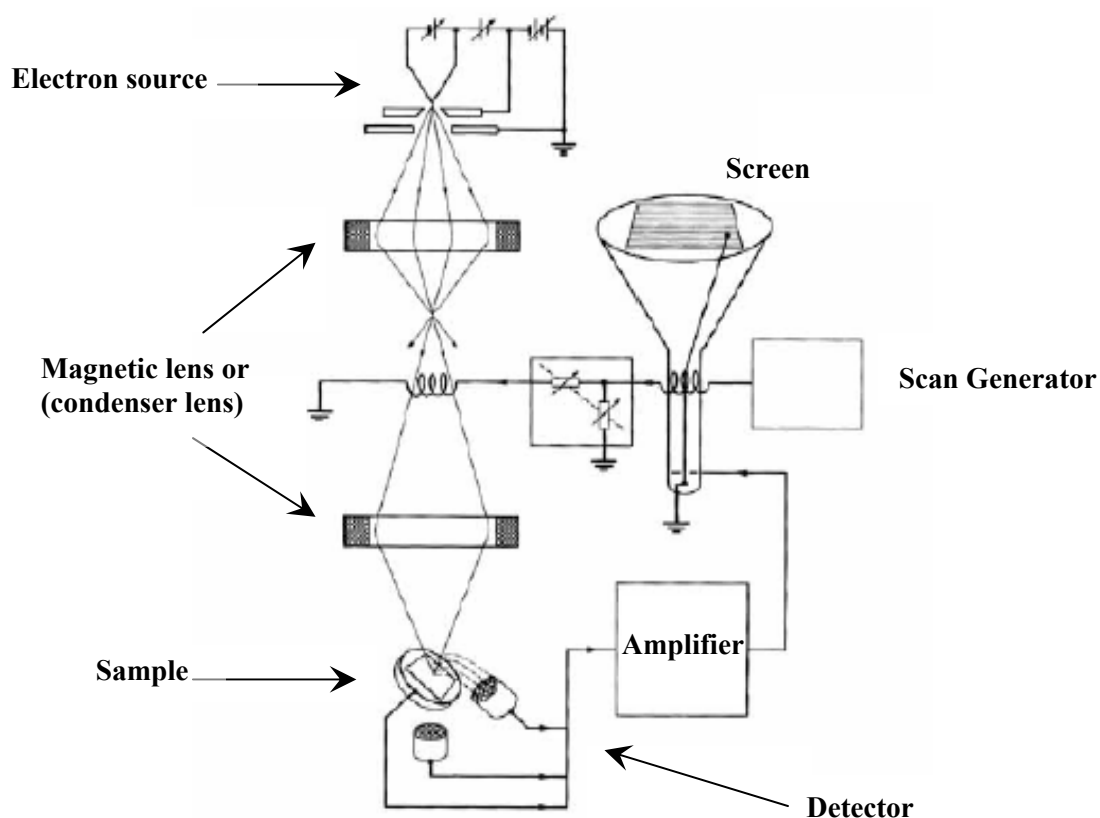
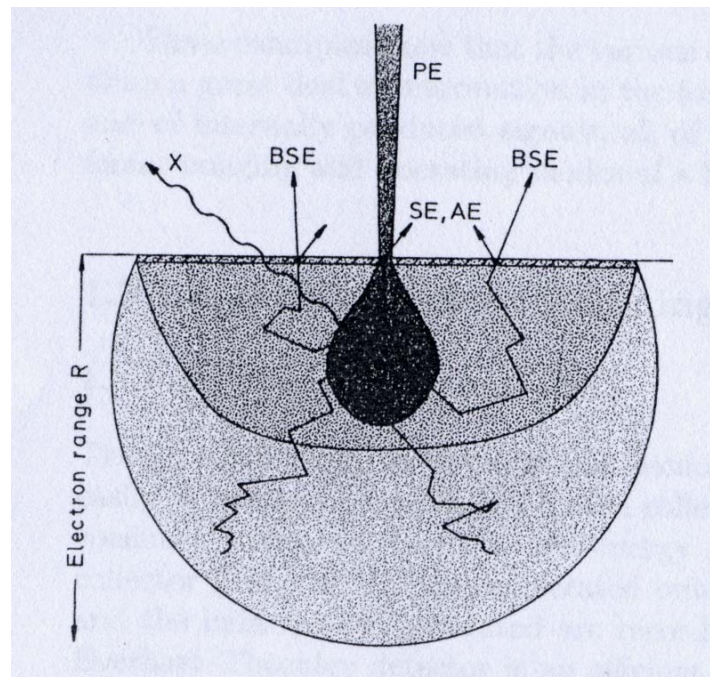


Fig.2-8: Schematic describing SEM

Three kinds of images produced in the SEM: secondary electron images, backscattered electron images, and elemental X-ray maps<sup>[78]</sup>. Secondary and backscattered electrons are conventionally separated according to their energies. They are produced by different mechanisms. High-energy primary electrons (PE) undergo either elastic scattering with the atomic nucleus or inelastic scattering with atomic electrons. In an elastic collision, a high-energy primary electron interacts with an atom causing scattering without loss of kinetic energy. Backscattered electrons (BSEs) are considered to be the electrons that exit the specimen with energy greater than 50 eV, as shown in Fig.2-9.



**Fig. 2.9** Secondary electrons (SE), backscattered electrons (BSE), Auger electrons (AE), and X-ray (X) in the diffusion cloud of electron range R for normal incidence of the primary electrons (PE).

In an inelastic collision some amount of the energy is transferred to another electron. If the energy transfer is very small, the emitted electron will not have enough energy to exit the surface. If the energy transferred exceeds the work function of the material, the emitted electron can exit the solid. It is referred to as a secondary electron (SE) with emitted energy of less than 50 eV. Most of the emitted secondary electrons are produced within the first few nm of the surface. The secondary electrons contributions into three groups SEI which result from the interaction of the incident beam with sample at the point of entry. SEII are produced by Backscattered electrons (BSEs) on exiting the sample. SEIII are produced by BSEs which have exited the surface of the sample and further interact with components on the interior of the SEM. SEII and SEIII come from regions far outside the spot defined by the incident probe and can cause serious degradation of the resolution of the image. An additional electron interaction in the SEM occurs when the primary electron collides with an atom and ejects a core electron from an atom in the solid. The excited atom will decay to its ground state by emitting either a characteristic X-ray photon or an Auger electron (Fig.2-9).

A reasonable fraction of the electrons emitted can be collected by appropriate detectors, and the output can be used to modulate the brightness of a cathode ray tube (CRT). In this way an image is produced on the CRT.

## **Chapter 3**

### ***Experimental aspects***

#### **3.1 Materials**

##### **3.1.1 Substrates**

**a)** Gold substrates: we used three different gold substrate depending on the type of experiment.

**I)** Gold /quartz : a 250 nm thick polycrystalline gold layer thermally evaporated on 2.5 nm Cr-primed, quartz substrate with grain sizes around 100 nm and RMS values of about 2.5 nm

**II)** Gold/mica : 300 nm thick Au(111) layer evaporated on mica

**III)** Gold/silicon: 30 nm polycrystalline gold layer evaporated on a silicon (111) wafer because the adhesion between the deposited gold film and the silicon wafers is weak, an interlayer of titanium 9 nm thick was used to enhanced the adhesion.

**b)** Silicon substrate. Boron-doped silicon (100), (110) and (111) wafers were purchased from Silicon Sense.

##### **3.1.2 Laboratory Equipment**

All items used in the laboratory were precleaned in a bath of KOH/2-propanol, fine cleaned in a second in H<sub>2</sub>SO<sub>2</sub> (PH~1) bath. The items were rinsed between the immersion steps by deionized water and also in the last step. Then the equipment was stored in an oven at 120 °C until used.

### 3.1.3 Substrate cleaning

The Au/quartz substrates were cleaned by oxygen plasma. This was done in a home-build glow discharge unit in accordance with Aebi et al<sup>[79]</sup>. In contrast to their work, we used a vacuum chamber creating controlled and defined oxygen atmospheres. The sample was placed on a grounded aluminium plate, and an oxygen atmosphere of 0.1 mbar was created. The tesla coil (BD-10ASV Electro-Technic Products Inc.(USA)) operating at 50kV at 500kHz was attached to the second parallel electrode, separated by 6.2 cm from the aluminium electrode, providing a high voltage glow discharge.

For the Au /Si treatment by UV light in ambient atmosphere, the samples were placed in an UVO cleaner (model 42-220, Jelight, USA) for 3 min under ambient atmosphere. Au/mica was cleaned by flame annealing. The respective XPS survey spectrum (Fig.3-1) shows a characteristic of clean gold substrate without any carbon or oxygen contaminations.

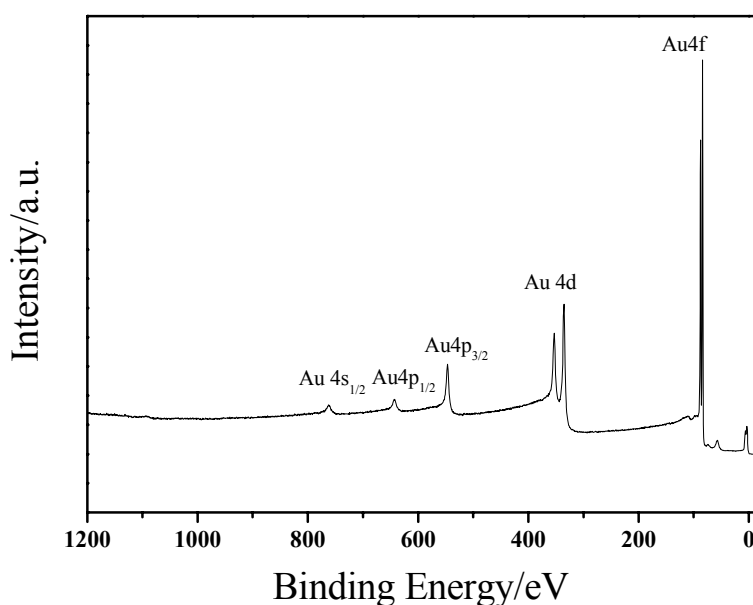


**Fig. 3-1:** XPS survey spectra of a clean gold substrate.

### 3.1.4 Chemicals

All the solvents and chemical compounds used in this work with their sources and their purities are listed in table 1.

**Table 1.** List of the chemicals with their sources and purities used in this work.

| Chemicals                          | Source                 | Purity    |
|------------------------------------|------------------------|-----------|
| Ethanol                            | Baker                  | ≥99.98%   |
| N,N-Dimethylformamid (DMF)         | ROTH                   | ≥ 99.97%. |
| H <sub>2</sub> O <sub>2</sub>      | VWR                    | 30%       |
| BPT                                | A. Küller, Heidelberg  | P.A.      |
| NBPT                               | A. Küller, Heidelberg  | P.A.      |
| HBP                                | A. Küller, Heidelberg  | P.A.      |
| Chloroform                         | Fisher scientific      | 99.99%    |
| N,N-Diisopropyl Carbodiimide (DIC) | Merck                  | ≥ 98%     |
| Tris-NTA                           | Ali Tinazli, Frankfurt | P.A.      |
| HS- EG3                            | Ali Tinazli, Frankfurt | P.A.      |
| Octadecanthiol                     | Aldrich                | 98%       |
| Acetonitril                        | Merck                  | 99.9%     |
| Sulfuric acid                      | Merck                  | 97%       |
| Toluene                            | Merck                  | ≥ 99.9%   |
| Ethylacetat                        | Fisher scientific      | 99.99%    |
| Hydrofluoric acid (HF)             | Fluka                  | 48%       |
| Acetone                            | Merck                  | ≤99.9%    |
| 2-propanol                         | Fisher Scientific      | 99.97%    |

## 3.2 Sample preparation

### 3.2.1. Preparation of HBP SAM

HBP SAM was synthesized according to the procedures described by Küller et.al<sup>[53]</sup>. First, the Silicon wafer (100), (110), and (111) were cleaned by an oxidative treatment in  $\text{H}_2\text{SO}_4/\text{H}_2\text{O}_2$  (3:1) to remove organic surface impurities. Subsequently, the wafer were rinsed with deionized water, dried in a nitrogen stream and etched for 10 min with 48% hydrofluoric acid in a polyethylene dish, rinsed with water and blown dry with nitrogen. After drying the wafer were stored in vacuum to avoid reoxidation. To form SAMs, as shown in figure1, the degassed and dried 0.05 molar toluene solution of HBP was added to the hydrogenated silicon surface in a dry nitrogen atmosphere. After the addition, the solution was degassed again by applying a weak vacuum until the solvent began to boil and the flask was flooded again with nitrogen. This procedure was repeated four times and the flask were kept there at  $100^\circ\text{C}$  for 16h. After cooling, the samples were rinsed with ethyl acetate, treated with ultrasound in this solvent for 3 min, and rinsed again. After a final rinse with ethanol, they were dried in a nitrogen stream and introduced immediately into a dry nitrogen atmosphere.

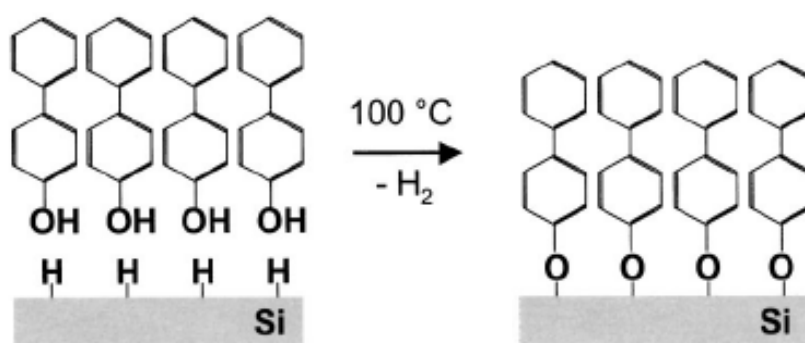


**Fig.3-2.** Hydroxybiphenyl self-assembled monolayer on Hydrogen- terminated Si surface.

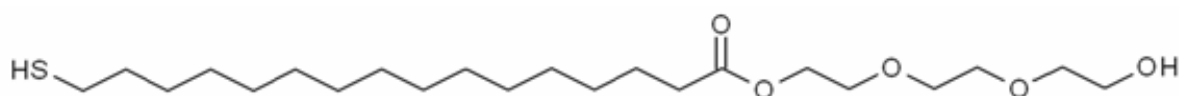
### 3.2.2. Preparation of aromatic thiol SAMs on gold

The 4-nitro-1,1-biphenyl-4-thiol (NBPT) and 1,1-biphenyl-4-thiol (BPT) were synthesized according to the procedures described by Eck et al.<sup>[36]</sup>. The different types of gold substrates were immersed in a degassed solution of 15 mM BPT or NBPT in N,N-dimethylformamide (DMF) for 72 h under nitrogen, followed by 5min sonication in DMF, rinsing with ethanol and drying in a nitrogen stream.

### 3.2.3. Preparation of alkanethiol SAMs on gold

**Octadecanethiol (ODT):** The freshly cleaned Au substrates were immersed in a 1mM ethanolic octadecanethiol solution for 24h at room temperature. After that, the samples were rinsed with ethanol and treated with ultrasound in this solvent for 3 min, and rinsed again then dried in a nitrogen stream and introduced immediately into a dry nitrogen atmosphere.

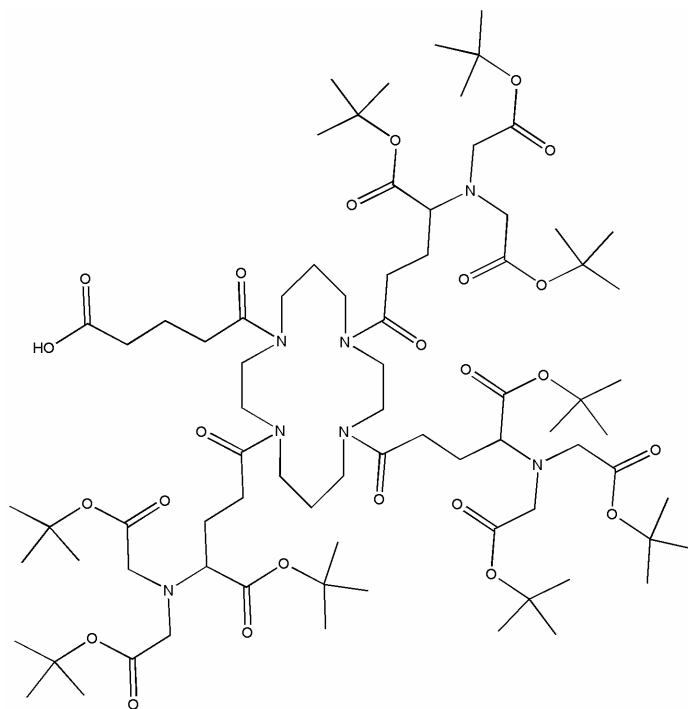
**Matrix-thiol (HS-C16-EG<sub>3</sub>-OH):** The fresh samples were immersed in 1mM ethanol HS-C16-EG<sub>3</sub>-OH solution for 5 days. Rinsed with ethanol and treated with ultrasound in ethanol for 3 min, rinsed again and dried in a nitrogen stream.



matrix thiols: HS-C16-EG<sub>3</sub>-OH

### 3.2.4. Coupling of Tris-NTA Modules to Amino Biphenyl SAMs

A mixture in the following sequence was prepared: 1.0 mL Chloroform + 0.03 mL tert-butyl protected *tris*-NTA (10 mM) + 1.0 mL DIC. The mixture was pre-heated at 75 °C for 5-8 min. E-beam treated NBP-SAM chips were put into the glass vial with the mixture and kept at 75 °C for 30 min. Rinsing 5 times with chloroform was followed by a deprotection in TFA at room temperature for 3-4 h. The chips with deprotected *tris*-NTA groups were rinsed 10 times with Millipore water and stored until usage at 4 °C.



Multivalent tris-NTA chelator with protected carboxyl functionality.

### 3.3. XPS measurement

XPS measurements were acquired using an Omicron Mutli-probe MXPS. The system processes a SPHERE energy analyser, a Monochromator x-ray XM1000 MKII and a SL1000 Electron gun as shown in the Fig.3-3.

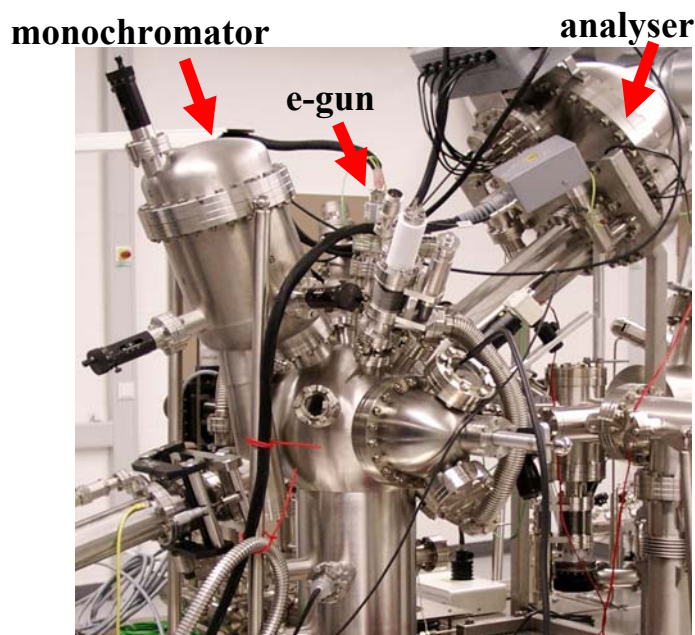


**Fig.3-3.** Omicron Mutli-probe MXPS

Monochromator Al  $K_{\alpha}$  irradiation (300W) was utilized. Table (2) and table (3) show all measuring parameters and constant values which are used in this work. The binding energy was calibrated using Au  $4f_{7/2}$  photoemission which was set at 84.0 eV as an energy standard. For deconvolution of XP peaks a Shirley background and symmetric Voigt factions were employed<sup>[80]</sup>. All peaks were resolved by a mixture of Gaussian and Lorentzian, using spectral processing program (multipak program) in the XPS system.<sup>[81]</sup>

**Table(2)** : The XPS parameters

|           | Start<br>[eV] | End<br>[eV] | Step<br>[eV] | Sweeps | Dwell<br>[s] | Passenergies<br>[eV] |
|-----------|---------------|-------------|--------------|--------|--------------|----------------------|
| Wide scan | 800           | -13.4       | 0.5          | 1      | 0.200        | 50                   |
| Au4f      | 92            | 80          | 0.05         | 2      | 0.200        | 25                   |
| N1s       | 414           | 393         | 0.05         | 3      | 0.200        | 25                   |
| O1s       | 545           | 525         | 0.05         | 3      | 0.200        | 25                   |
| C1s       | 300           | 275         | 0.05         | 3      | 0.200        | 25                   |
| S2p       | 175           | 155         | 0.05         | 5      | 0.200        | 25                   |
| Ni2p      | 860           | 845         | 0.05         | 3      | 0.200        | 25                   |

**Table(3)** : Constant values which used in this work.

|             | Au4f   | N1s    | O1s    | C1s    | S2p    |
|-------------|--------|--------|--------|--------|--------|
| $\lambda$   | 36.00  | 21.1   | 19.3   | 23.8   | 27.7   |
| $\sigma$    | 17.47  | 1.77   | 2.85   | 1.77   | 1.74   |
| $E_{kin}$   | 1402.6 | 1087.6 | 955.6  | 1201.9 | 1324   |
| $L(\gamma)$ | 1.1859 | 1.3718 | 1.3718 | 1.3718 | 1.2231 |

### 3.4. Low electron energy irradiation

The samples irradiated by two ways. First samples with large area were introduced in situ Ultra high vacuum (UHV) ( $p \sim 1 \times 10^{-10}$  mbar) and irradiated by electron flood gun (SL1000), at electron energy 50 eV and the irradiation doses between  $10000 \mu\text{C}/\text{cm}^2$  and  $100000 \mu\text{C}/\text{cm}^2$  were applied. Second samples were irradiated by using proximity printing. This samples were patterned with  $1 \mu\text{m}$  and  $1.2 \mu\text{m}$  circles through the stencil mask (Quantifoil, Jean) as shown in Fig.3-4 in high vacuum ( $p \sim 5 \times 10^{-7}$  mbar) at electron energy 100eV and with different doses between  $10000 \mu\text{C}/\text{cm}^2$  and  $45000 \mu\text{C}/\text{cm}^2$ .

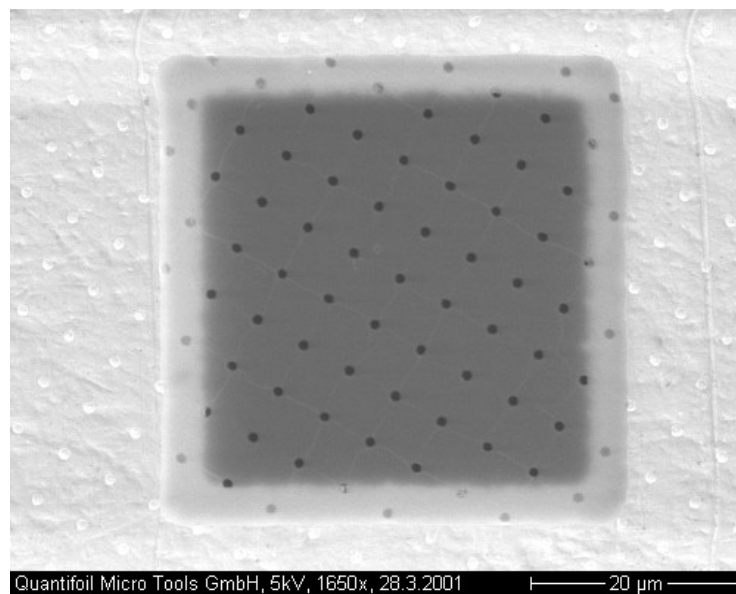


**Fig.3-4:** Quantifoil R 1/4 from [www.quantifoil.com](http://www.quantifoil.com)

### 3.5. Heating Samples



**Fig.3-5.** The sample stage

The Samples were mounted on the heatable manipulator of the photoelectron spectrometer (Omicron) which is shown in Fig.3-5. The thermocouple at the manipulator was calibrated with melting points of pure metals (lead and bismuth). The samples were heated in steps of 20-50 K from room temperature up to 1000 K, and kept for ~3-12 h for every temperature to be sure that the sample is in thermal equilibrium before the XPS measurement was performed.

### 3.6. Atomic Force Microscopy

Atomic force microscopy (AFM) was performed with a NT-MDT NTegra atomic force microscope (NT-MDT, Moscow). Measurements were done by using two different modes, contact mode for thermal stability experiments and Tapping mode for protein immobilization experiments.

In contact mode, the images were taken at constant force using silicon cantilever with force constant 0.1 N/m and in the case of tapping mode, imaging was taken at resonance frequencies of around 20-30 kHz in HBS buffer and at drive amplitudes of 100 to 150 mV. In this case silicon nitride cantilevers with a force constant of 0.06 N/m (Veeco Instruments) were used. Imaging of the chip surfaces was always performed in HBS buffer.

### 3.7. Scanning Electron Microscopy

Scanning electron microscope (REM) images were acquired using Omicron Mutliscan STM VT. The images are performed at 10keV and 400pA.

### 3.8. Fluorescence Microscopy:

Patterned chips were imaged by confocal laser scanning microscopy (LSM 510, Carl Zeiss, Jena). Atto565-labelled, His<sub>10</sub>-tagged maltose binding protein (<sup>At565</sup>MBP-His<sub>10</sub>) was immobilized specifically on the chip. After rinsing, the chips were immediately mounted into a self-built liquid cell and imaged using a Plan-Neofluor 63×oil-immersion objective (NA 1.4) and an inverted microscope set-up (Axiovert 200M, Carl Zeiss, Jena). An argon laser (488nm, 25mW) was used for the excitation of both Oregon Green and QuantumDot 655. Fluorescence image data were processed with LSM Zeiss software (Zeiss).

## Chapter 4

### *E-beam Lithography of Hydroxybiphenyl (HBP)*

#### Sensitivity of Hydroxybiphenyl to irradiation doses.

HBP SAMs can be cross-linked under irradiation with electrons according to the scheme depicted in figure 4-1, and HBP has been used as negative e-beam resist for fabrication of single lines and line grating with nominal line widths between 500 and 10 nm<sup>[53]</sup>.

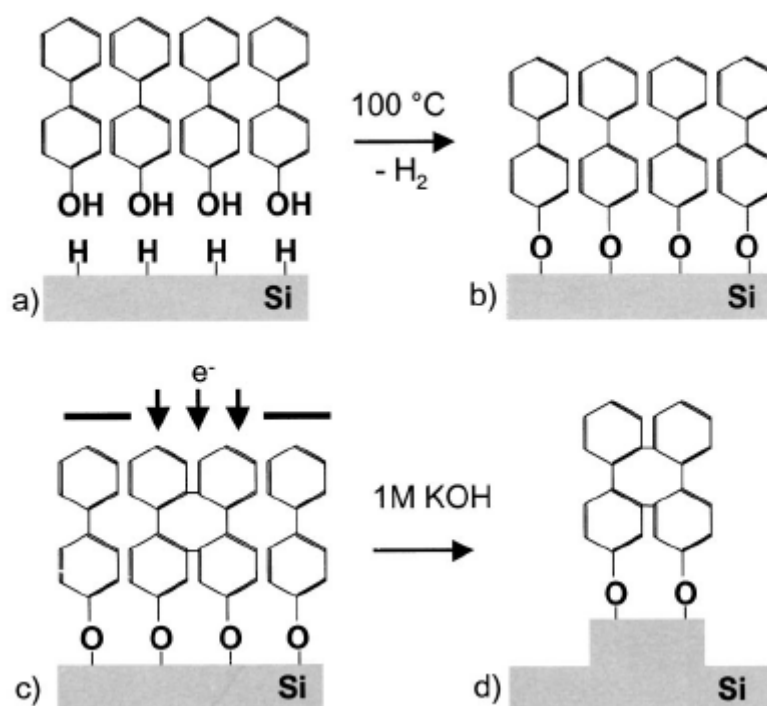


**Fig. 4-1.** (a) and (b) well-ordered monolayers of HBP SAM of H-terminated Si surfaces.

(c) E-beam induces cross-linking of the SAM. (d) Etched SAM for 1min in KOH.

On this basis, the sensitivity of HBP SAM to electron-beam was investigated. Fig.4-2 shows patterns of isolated 1 $\mu\text{m}$  long single lines with varied dose from left to right in steps 2000 $\mu\text{C}/\text{cm}^2$ . The e-beam energy was chosen at 3keV, which was a reasonable choice to minimize proximity effects while keeping the e-beam size small<sup>[53]</sup>. The sample was irradiated from starting dose with 2,000  $\mu\text{C}/\text{cm}^2$  (Fig.4-2 left above) to the final dose 80,000  $\mu\text{C}/\text{cm}^2$  (Fig.4-2 second line right). In the top of the Fig.4-2 an AFM profile has been determined from the same pattern.

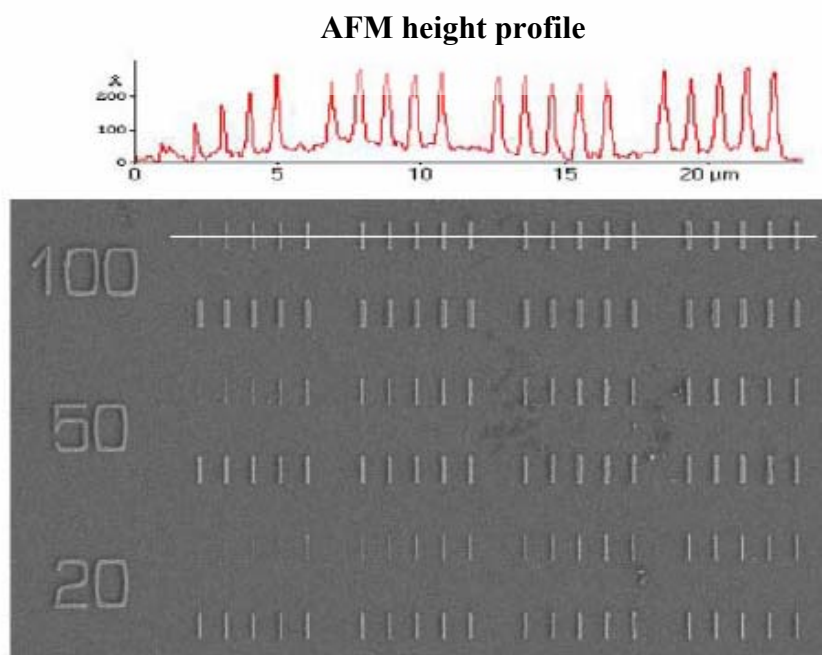


**Fig.4-2.** SEM image of an array of single lines after a 3 min KOH etch. The nominal linewidth is indicated at the left-hand side. The area dose was varied from line to line in increments of 2  $\text{mC}/\text{cm}^2$ . Top: AFM-height profile along the lines indicated in the figure.

The lines have been etched for 3 min and the height profile clearly shows how the line height increases with the area dose and the line broadens at high doses due to proximity effects. To minimize these unwanted exposures nominally 6nm wide lines etched in KOH for 1min are investigated. An AFM image of a part of the Structures is shown in Fig.4-3.

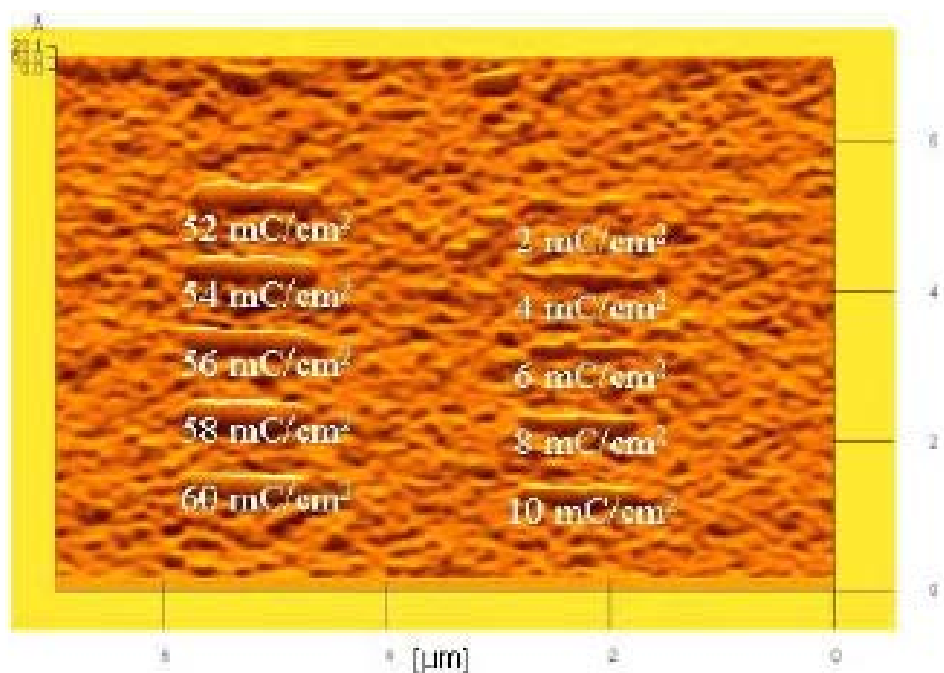


**Fig.4-3.** AFM image of part of the nominal 6nm lines structure.

**Fig.4-3** shows a plot of the line heights as a function of the applied electron dose. The width of the nominal 6nm wide lines is  $\sim 10$ nm. The height  $H$  of the irradiated lines after 1 min KOH etched has been fitted exponentially by:

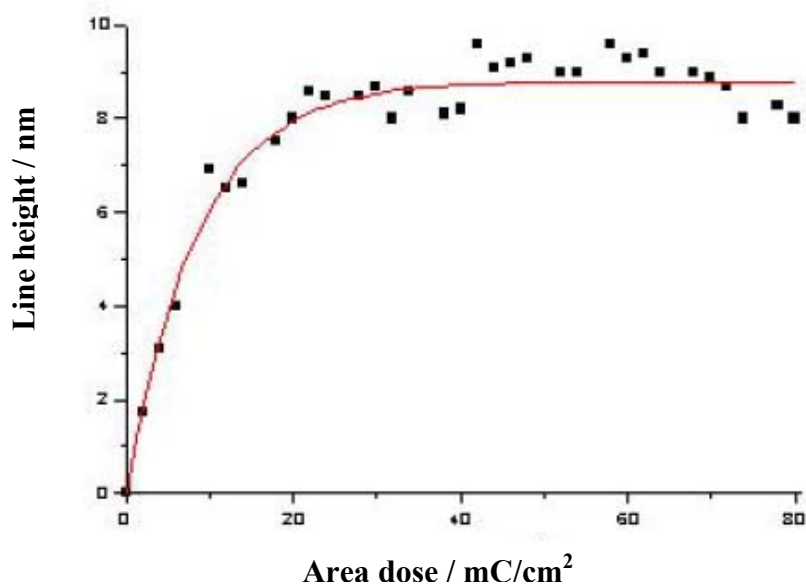


**Fig.4-4.** Plot of the AFM line heights as a function of area dose for single lines with a nominal width 6nm, after a 1 min KOH etch.

$$h = h_0 \left( 1 - \exp\left(-\frac{D}{D_0}\right) \right)$$

Where  $h_0$  is the measured line height corresponding to saturation,  $D$  is the applied electron dose,  $D_0$  is a measure for the efficiency of the processes. From the fit, we obtain values of  $D_0 = 8800 \mu\text{C}/\text{cm}^2$  and  $h_0 = 8.9 \text{ nm}$ . We can estimate from the plot, the dose required for complete cross linking of HBP to be  $\sim 20000 \mu\text{C}/\text{cm}^2$ , which is in the same order of magnitude as the dose for Biphenylthiol on gold<sup>[57]</sup>. The height of the lines exposed at doses below  $20000 \mu\text{C}/\text{cm}^2$  results from the difference between etching of the silicon without resist and silicon that was protected for some time by an incomplete cross linked SAM.

## **Chapter 5**

### ***Thermal stability of pristine and cross-linked aromatic SAMs***

## Section A

### *Thermal stability of pristine Biphenylthiol (BPT) and Octadecanethiol (ODT)*

Knowledge of thermal stability of self-assembled monolayers molecules, leads us to better design and selection of these molecules for specific applications. In this chapter we investigate the thermal stability of pristine and cross-linked aromatic SAMs.

#### 1- Characteristic of pristine Biphenylthiol (BPT) film:

The XPS measurements were carried out to determine the film quality. The wide scan, C1s and S2p XP spectra of BPT/Au are presented in Fig.5-1. Besides Au substrate signals the wide scan spectrum exhibits only characteristic emission of S2p and C1s and no oxygen contamination was detected. The thickness of BPT/Au determined from the attenuation of the Au4f<sub>7/2</sub> signal ( $\lambda=36$  °A) is  $10\pm 0.7$  Å; the C/S ratio is  $12\pm 1/1$ , which corresponding to a high quality BPT monolayer.

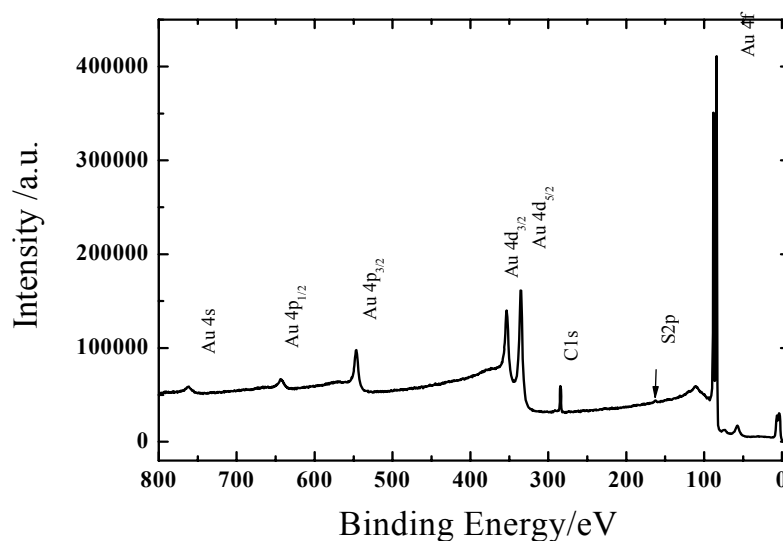


Fig.5-1. Wide scan, C1s and S2p XPS spectra of BPT/Au.

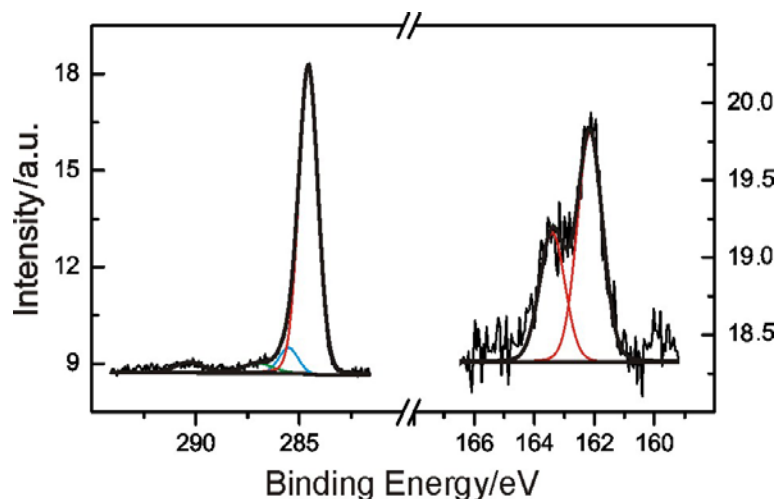


Fig.5-1. Wide scan, C1s and S2p XPS spectra of BPT/Au.

The C1s signal composes of four constituents. The main one C1s (I), at 284.2 eV with a full width at half maximum (FWHM) of 1.15 eV, is assigned to the 11 carbon atoms in the aromatic rings; the C1s(II) at 285.1 eV (FWHM=1.15 eV) corresponds to remaining carbon atom in the C-S bond; C1s (III) at 286.8 eV (FWHM=1.7 eV) and C1s (IV) at 290.3 eV (FWHM=1.7 eV) have much lower intensities and are assigned to aromatic shake up satellites.

S2p spectra exhibit two strong peaks at around 162eV and 163.2 eV. The sulfur spectrum consists of S2p<sub>3/2</sub> and S2p<sub>1/2</sub> peaks with an intensity ratio of 2:1 according to the spin-orbit coupling<sup>[82,83]</sup> and is assigned to thiolate species<sup>[84]</sup> Besides thiolate species 2Sp<sub>3/2</sub> at 162 eV, there are different sulfur species were reported in SAMs on Au surfaces. Among them disulfide or sulfide and unbound thiol<sup>[82]</sup> species at binding energies between 163-164 eV, atomic sulfur (isolate sulfur)<sup>[83,85]</sup> at 161 eV and oxidized sulfur<sup>[86]</sup> > 166 eV.

## 2- Characteristic changes of pristine BPT as a function of Temperature

Fig.5-2 shows the S2p and C1s photoelectron spectra for the BPT after thermal annealing at different temperatures. The S2p spectra, before the sample was annealed, exhibited doublet at 162.0 and 163.2 with a full width at half maximum (FWHM) of 0.9 eV which is assigned to the thiolate bound. After the sample was annealed to 384K there is no change in the S2p peaks. Above 430K the S2p signal shows the formation of a new S2p doublet at 161.3 and 162.5 with a FWHM of 1.3 eV. Compared to the thiolate doublet at room temperature, its position is shifted by  $\sim 1$ eV to lower binding energy, which reflects the formation of atomic sulfur that is bound only to metallic substrate. At higher temperature 558K only atomic sulfur is observed. Thus, the thiolate bonds do not sustain such high temperatures and the C-S bond cleavage can be observed at temperatures above 400K.

In Fig.5-2, at room temperature the C1s signal consists of four constituents at 284.2 eV as C1s (I), the C1s (II) at 285.1eV, C1s (III) at 286.8 eV and C1s (IV) at 290.3 eV. At 384K as shown in Fig. 5-2, a little decrease in C1s signal can be noticed. The C1s signal shows further decrease after heating to 430K. At 558K only 10% of initial intensity remains corresponding to an almost complete loss of the SAM.

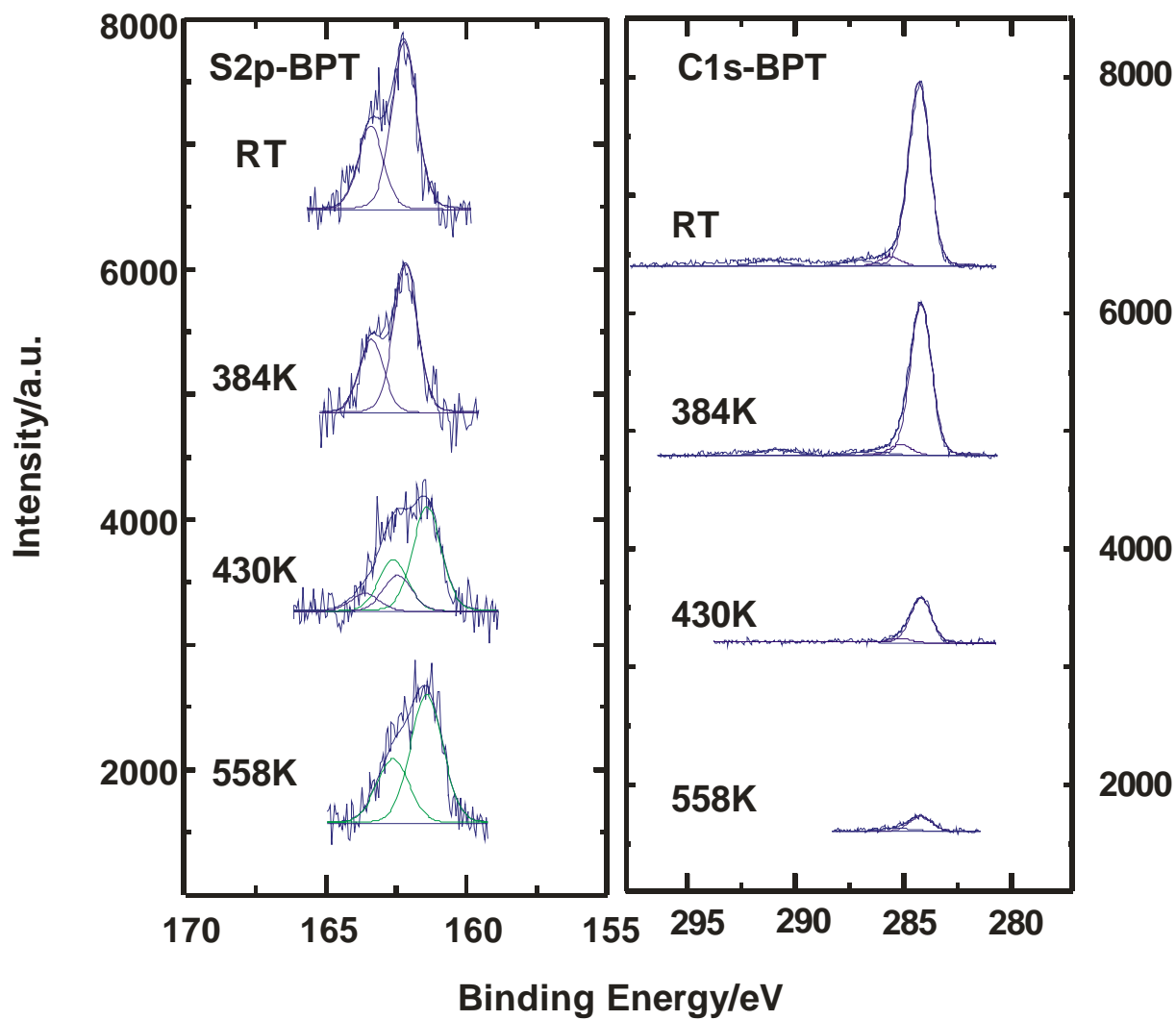
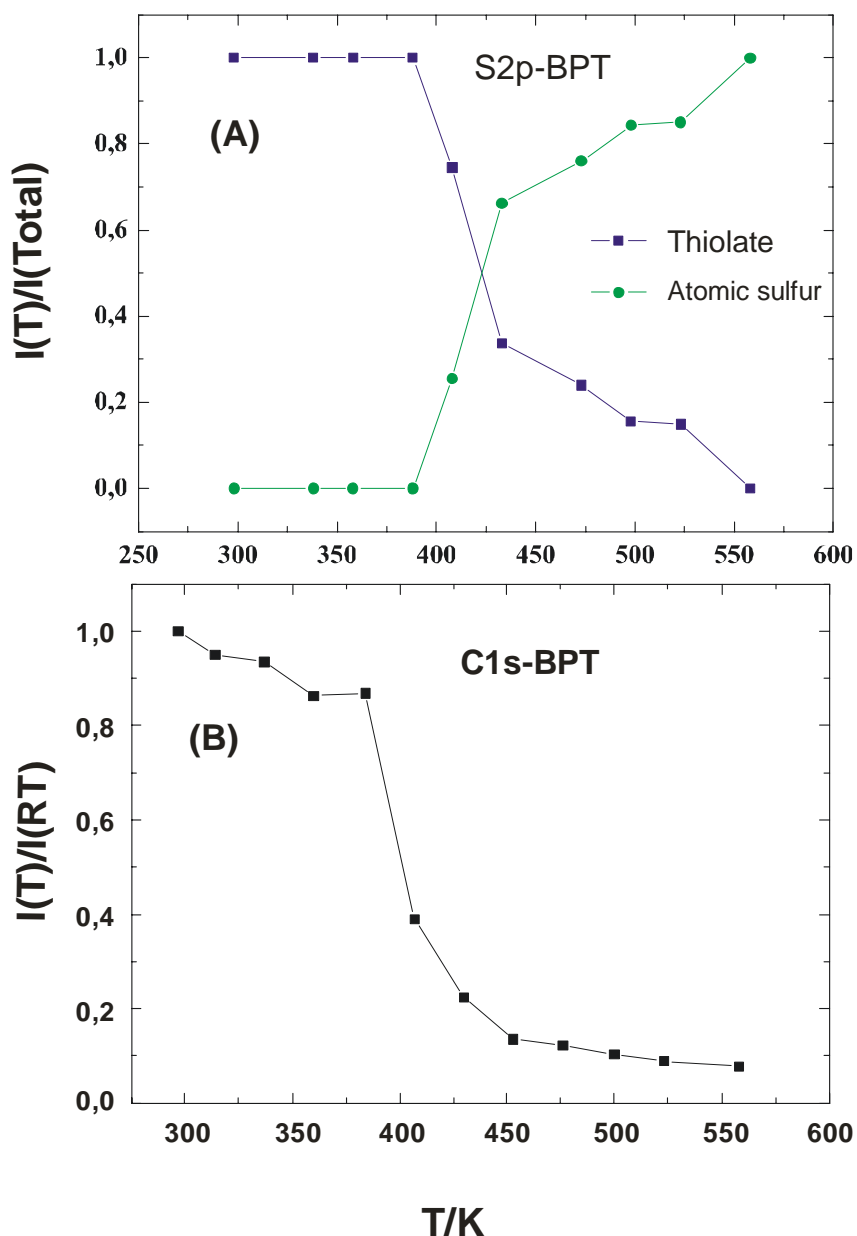


Fig.5-2. Variation of S2p and C1s X-ray photoelectron spectra with annealing temperature.



**Fig.5-3.** Relative peak area of S<sub>2p</sub> and total C<sub>1s</sub> signal intensity as a function of temperature.

Fig.5-3, shows the variation of two S<sub>2p</sub> species and the total intensity in C<sub>1s</sub> signal as a function of temperature. Below 384K only thiolate bound present at the surface. Above this temperature the atomic sulfur forms and its intensity increased with the increasing temperature, whereas the thiolate intensity is decreasing. At 558 K only atomic sulfur can be observed. The total C<sub>1s</sub> peak decreasing with the increasing the temperature as shown in Fig.5-3 (B). The pristine biphenyl SAM desorption occurs

at temperature above 400K via C-S bond breaking and also, can be judged from the S2p intensity direct desorption of thiolate occurs.

### 3- Characteristic changes of Octadecanethiol (ODT) as a function of Temperature

To get more insight in the desorption mechanisms of aromatic SAMs we compared that with the desorption of a classical alkanethiol SAM like octadecanethiol (ODT).

The thickness of ODT/Au determined from the attenuation of the Au4f<sub>7/2</sub> signal ( $\lambda=36^\circ\text{A}$ ) is  $26\pm 0.7 \text{ \AA}$  and the C/S ratio is  $21\pm 1/1$  which is higher than the theoretical values obtained which may be related to inaccuracy of  $\lambda$ -value, since no additional S2p species (e.g. unbound thiol) are observed in the XP spectra as shown in Fig.5-4. The S2p and C1s XPS spectra of ODT film at room temperature and after annealing at different temperatures are presented in Fig.5-4. The poor quality of the S2p signal is related to signal/to noise ratio of alkyl chain of octadecanethiol.

In the S2p XP spectra shows only a thiolate doublet peak at binding energies (BEs) 162.0eV and 163.2 eV (FWHM=0.9eV). We observed at above 400K another S2p doublet peaks at low binding energy at 161.0 eV and 162.2 eV (FWHM =0.90eV), which is denoted as atomic sulphur similar to behaviour of BPT at the same temperature range. At above 476 K only atomic sulfur peak was observed. In the C1s XP spectra, a single C1s sharp peak at 284.950eV was observed with a FWHM of 1.15eV attributed to the alkyl chain of ODT molecules was observed at room temperature (RT). After annealing and above 372K the C1s signal decreases due to ODT molecules desorption from the Au surface and notice another C1s signal peak at lower binding energy 284.0 eV which assigned to the striped alkyl chains and molecular decomposition<sup>[83]</sup>

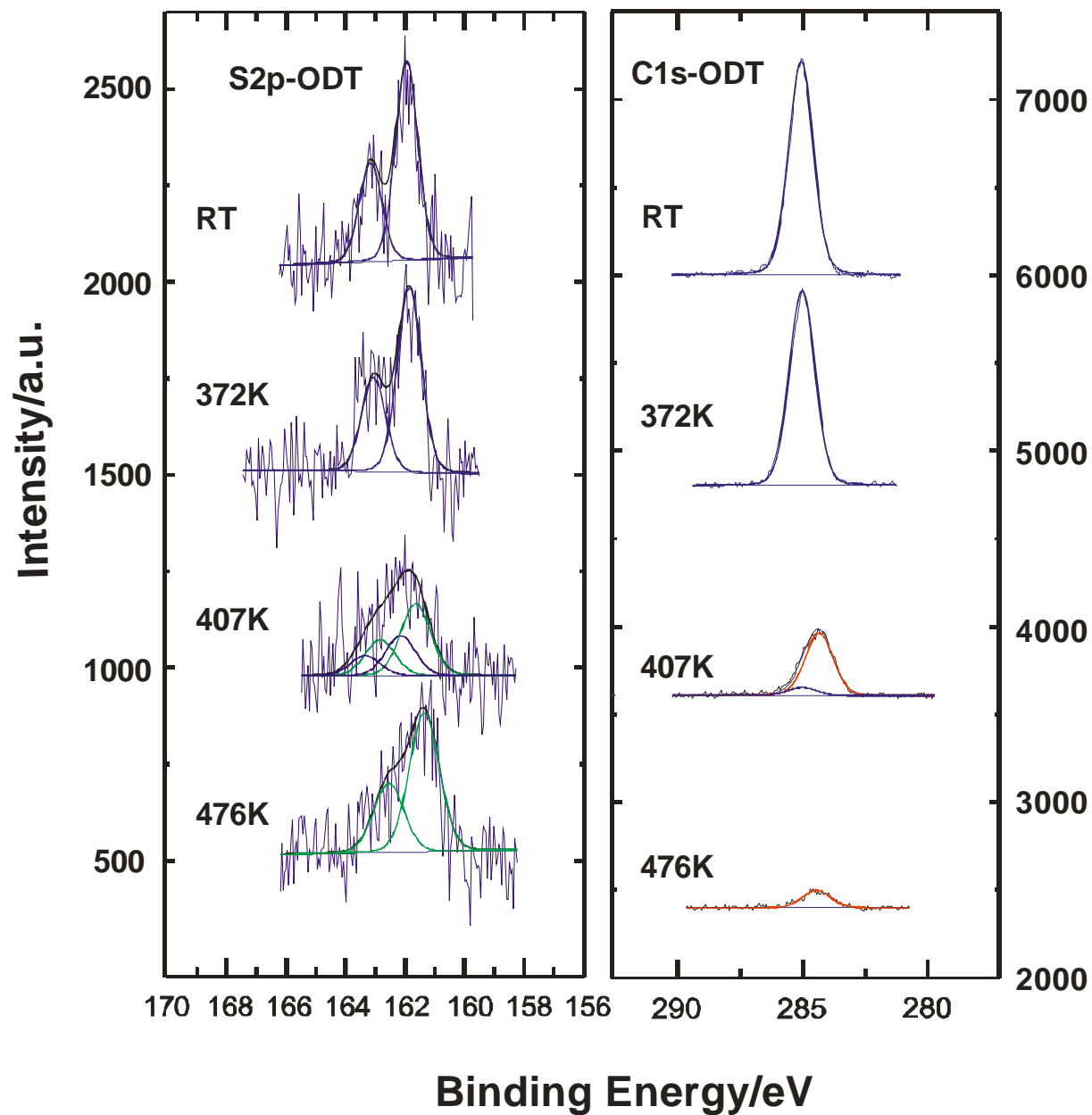


Fig. 5-4. The S2p and C1s XP spectra of ODT/Au with different temperatures.

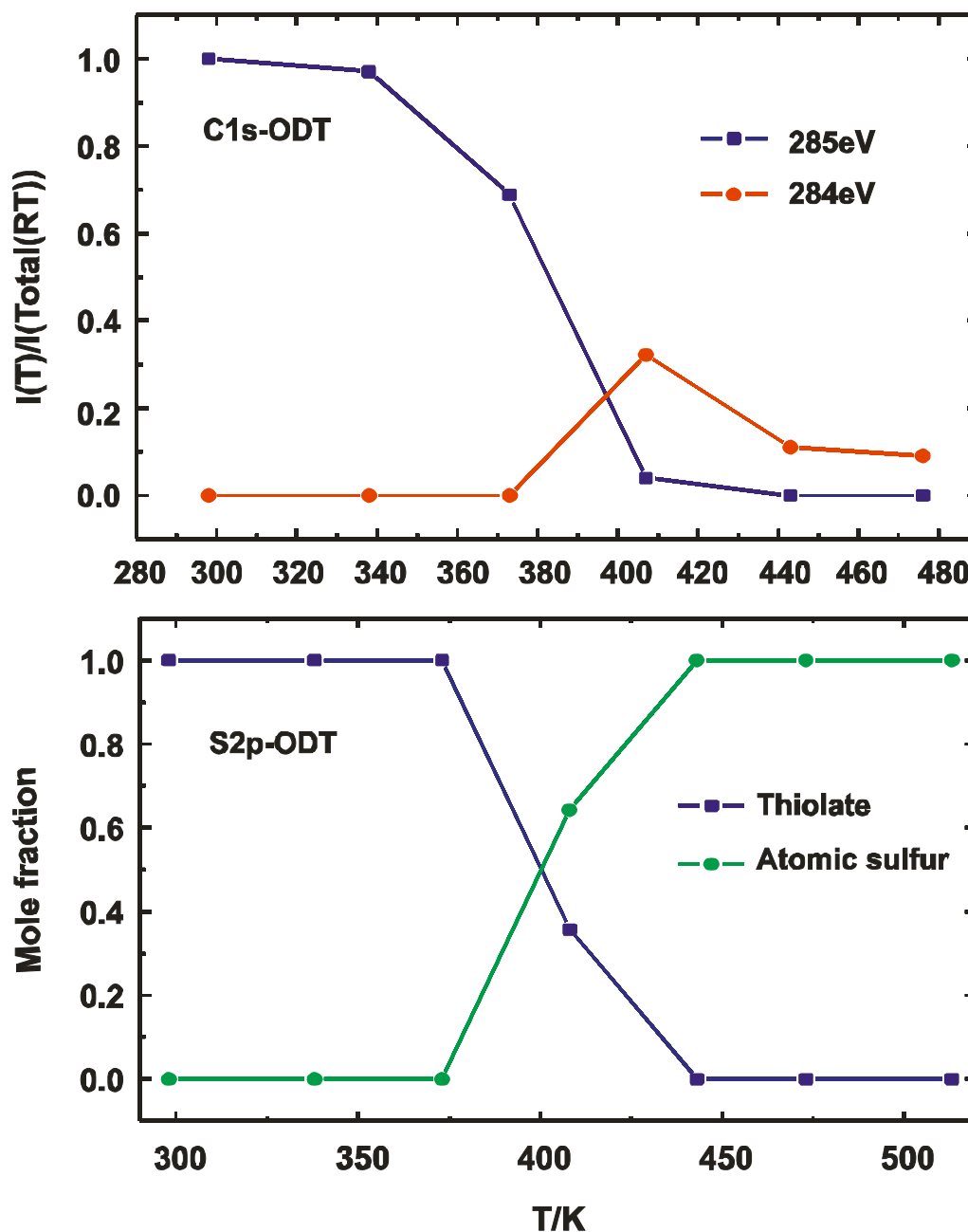
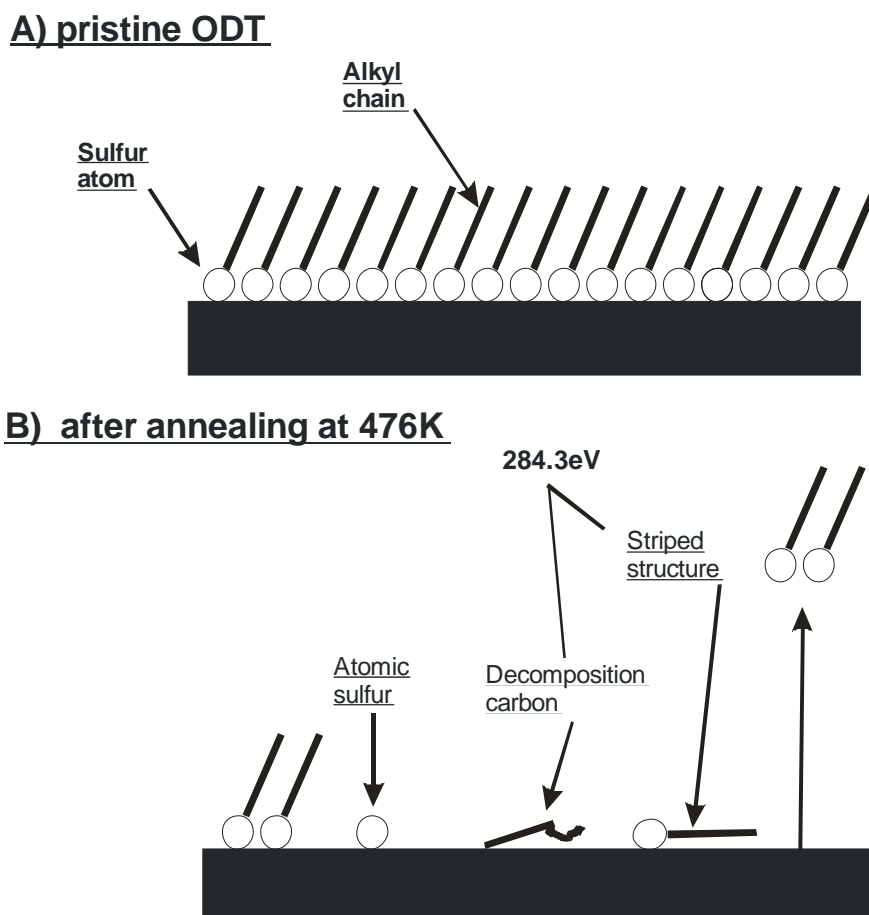


Fig. 5-5. Relative peak areas of C1s and S2p as a function of temperature.

Fig.5-5, shows the variation of different S2p and C1s signals as a function of temperature. Similar to BPT SAM the atomic sulphur formed above 400 K and decreased the thiolate signal. The C1s (alkyl chain) signal at binding energy 285eV decreased with high temperature and another C1s signal formed at 476K at binding energy 284eV at low intensity about 9% from total C1s intensity. The desorption

mechanism of ODT SAM is the same to pristine BPT. Whereas, ODT desorption occurs above 400K via C-S bond cleavage and desorption of thiolate.



**Fig.5-6.** Schematic of a) pristine ODT on Au and b) after annealing to 476K<sup>[83]</sup>

Fig.5-6 shows a schematic of the ODT-SAMs before and after annealing to 558K. After the annealing the atomic sulphur and striped ODT molecules exist on the Au surface.

## ***Section B***

### ***Thermal stability of cross-linked Biphenylthiol (BPT)***

In this section we present the effect of e-beam induced corresponding to the BPT SAM on their thermal stability.

#### **1- Characteristic of cross-linked Biphenylthiol film:**

Fig. 5-7 shows S2p and C1s XPS spectrum of not irradiated and irradiated BPT with different doses, 10, 25, 45 and 100mC/cm<sup>2</sup>. S2p signals show the formation of a second doublet at higher binding energy 163.5 and 164.7 at FWHM=1.6eV, which is indicative for the formation of sulfide or disulfide<sup>[82,87]</sup> This second doublet S2p signal grows with increasing irradiation doses. Its intensity corresponds to ~ 45% of the total sulfur signal at electron dose 100mC/cm<sup>2</sup>.

In the C1s XPS spectra in Fig.5-6, a signal C1s (I) decreases and C1s(II) increases with increasing irradiation doses, which can be associated with the irradiation-induced related to form sulfide or disulfide species. The reduction of the C1s (I) is 17% from original C1s(I) at 100 mC/cm<sup>2</sup>.

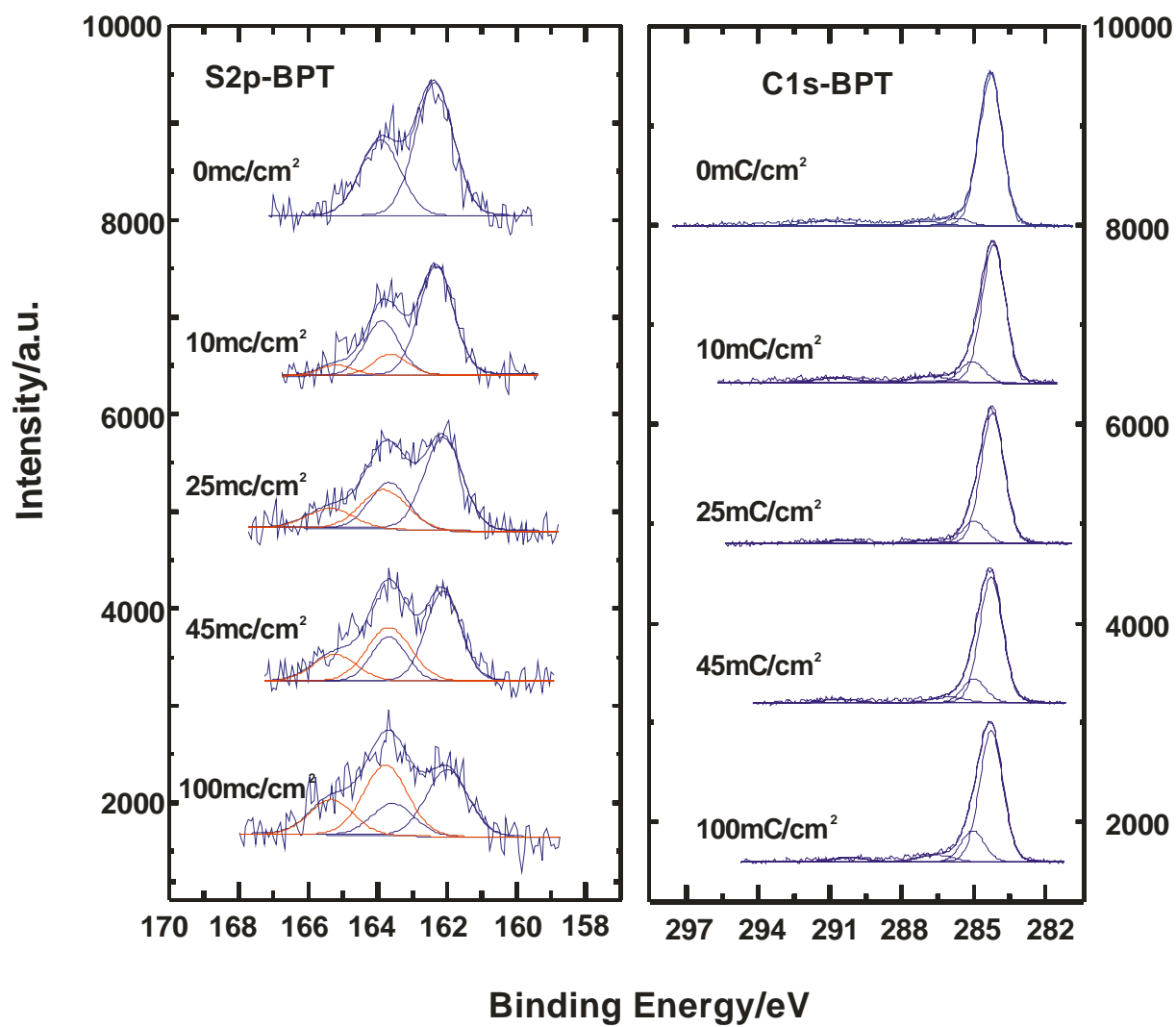
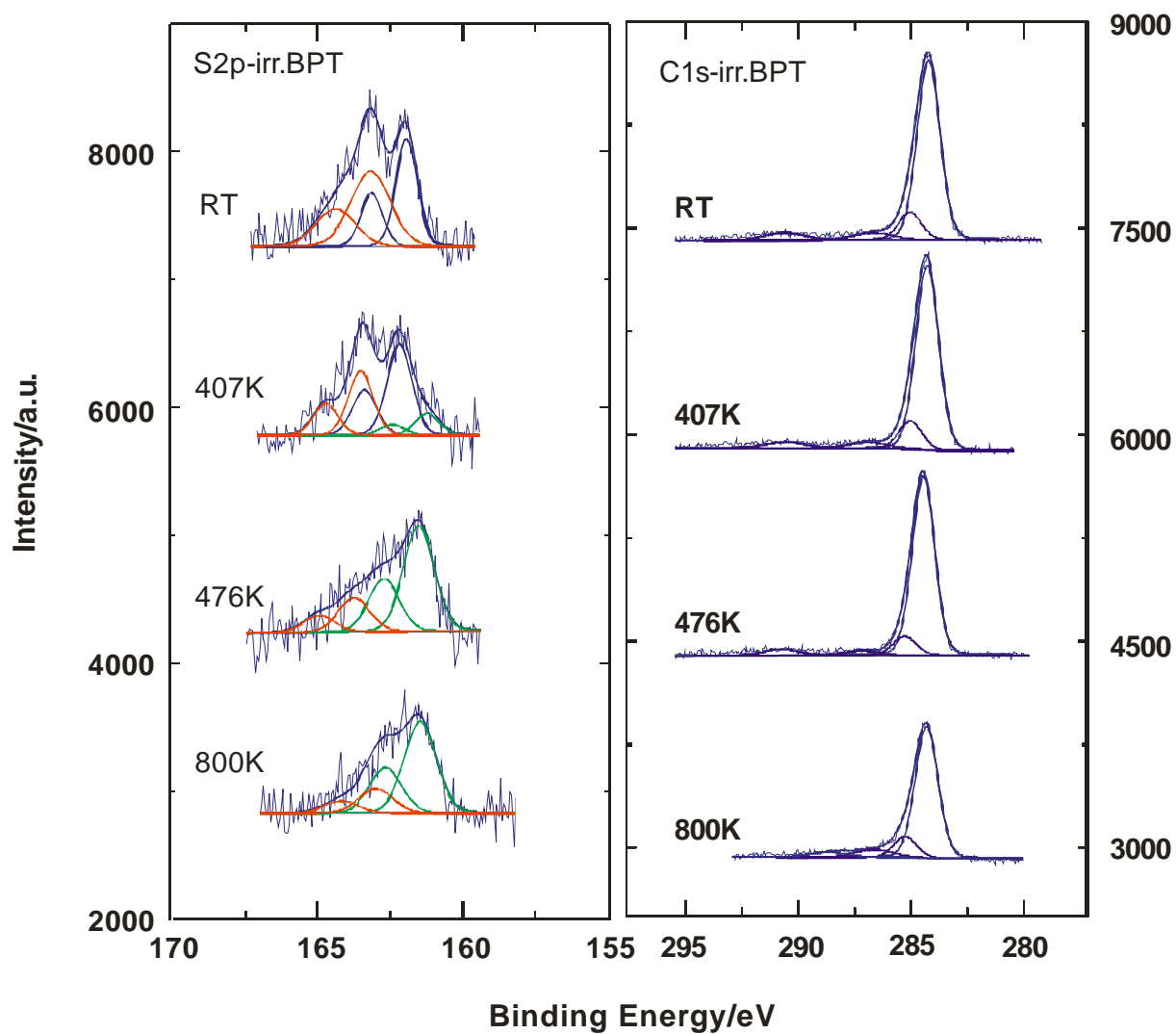


Fig.5-7. The S2p and C1s of BPT with different irradiated doses

## 2- Cross-linked BPT as function of Temperature

Figures 5-8 and 5-9, show XPS spectra and variation intensity of the S2p and C1s of BPT as a function of temperature, respectively. At room temperature S2p signal consist of thiolate bond at binding energy 162.2eV and sulfide or disulfide bond at binding energy 163.0eV. The main C1s (I), at 284.2 eV with a full width at half maximum (FWHM) of 1.15 eV, is assigned to the 11 carbon atoms in the aromatic rings; the C1s(II) at 285.1 eV(FWHM=1.15 eV) corresponds to remaining carbon atom in the C-S bond; C1s (III) at 286.8 eV (FWHM=1.7 eV) and C1s (IV) at 290.3 eV (FWHM=1.7 eV) have much lower intensities and are assigned to final state effects. Below 400K no changes in the S2p and C1s signal peaks. At 408K the third doublet S2p signal formation at low binding energy 161.0eV which assigned as atomic sulfur with decreasing the thiolate and increasing disulfide signals and no changes happened in C1s peaks. At the 475K, atomic Sulfur signal increased, the cross-linked monolayer loses most of its thiolate bonds and the intensity of disulfide decreased. The C1s intensity shows only little changes. With raised the temperature to 1000K (the highest temperature our experimental set up permits) the dominating S2p signal is the atomic sulfur. The C1s signal shows 80% (see Fig.5-9) of its initial intensity and the binding energy of the aromatic C1s(I) species remain as at room temperature.



**Fig.5-8.** XPS spectra of S2p and C1s signals of cross-linked BPT (45mC/cm<sup>2</sup>) as a function of temperature.

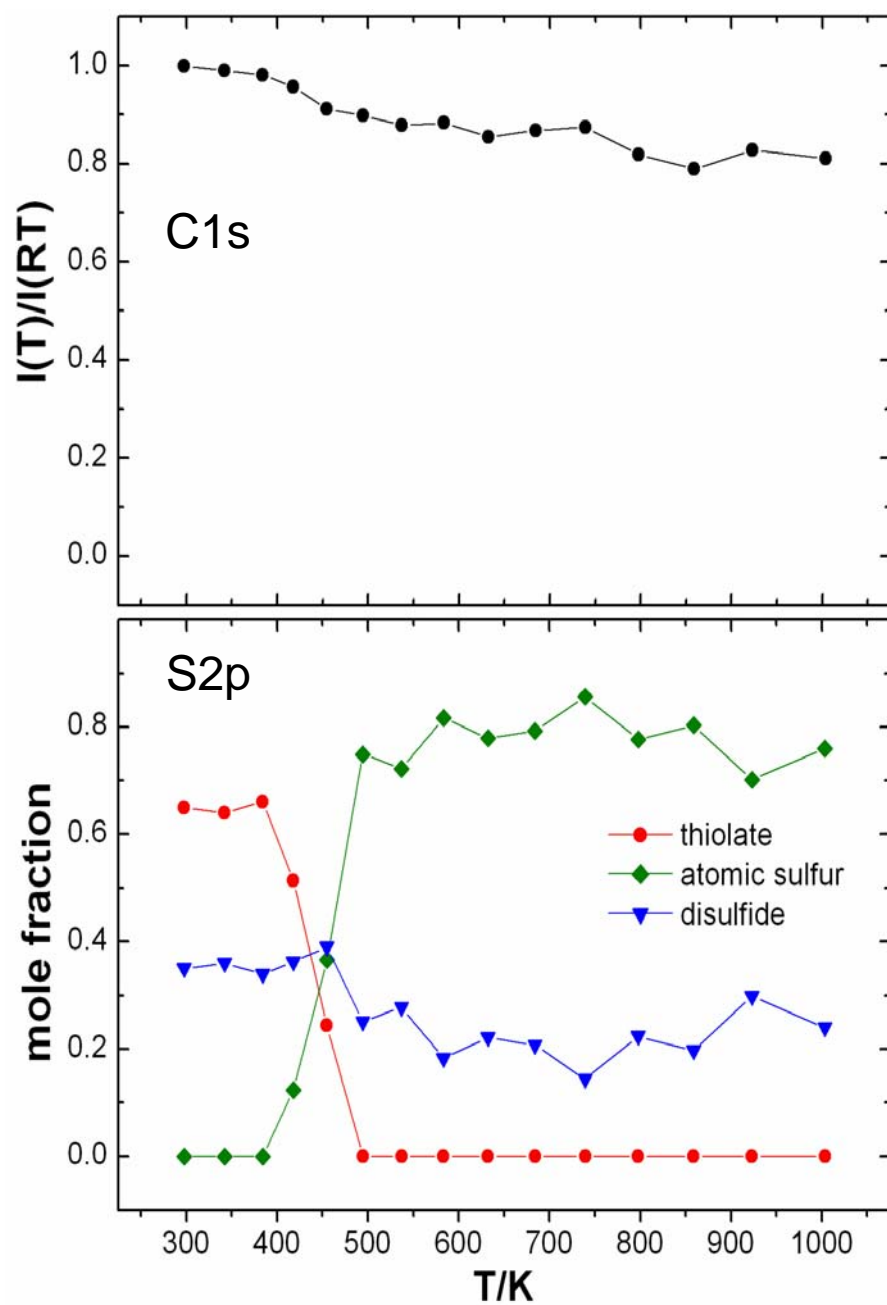


**Fig.5-9.** Relative peak area of S2p and total C1s signal intensity as a function of temperature.

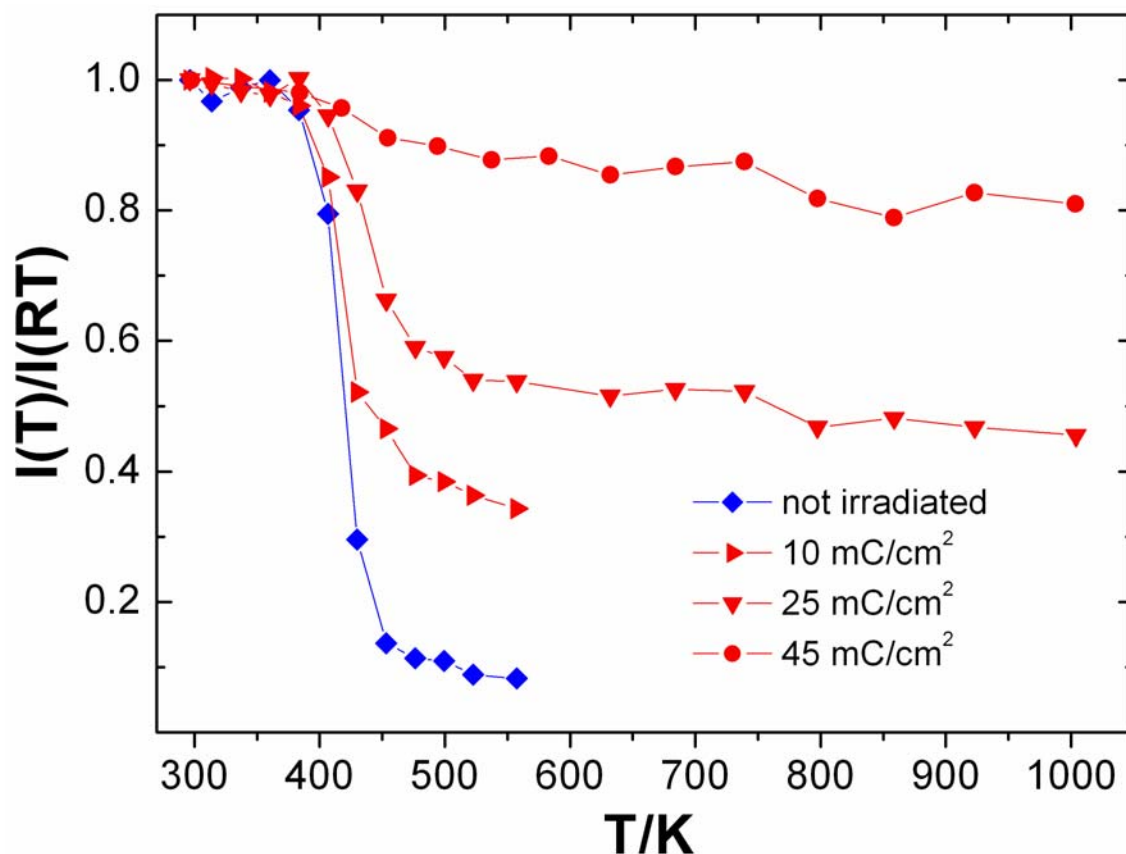


**Fig.5-10.** Temperature dependence of the C1s signal of Biphenthylthiol SAMs as a function of irradiation dose.

Fig.5-10 shows the intensities of the C1s signal of pristine and cross-linked BPT as a function of temperature and electron dose. The pristine BPT SAM desorbs at about 400 K. SAMs cross-linked at 25 mC/cm<sup>2</sup> are more stable than pristine ones, and a 50% loss of material is found. The XPS intensity of SAMs cross linked at 45 mC/cm<sup>2</sup> remains above 80% up to the highest temperatures. We thus conclude that at an electron dose of 45 mC/cm<sup>2</sup> cross-linking is complete and almost no carbon loss is observed. Lower electron doses lead to partially cross-linked SAMs, from which BPT molecules can

### 3-Thermal desorption lithography (TDL):

The above described temperature stability of cross-linked SAMs can be utilized for the creation of molecular surface patterns. In a novel scheme called “thermal desorption lithography” (TDL), a pattern is written in an aromatic SAM by e-beam or extreme ultraviolet lithography. The structure is then heated in vacuum above the desorption temperature of the pristine SAM, so that non-cross-linked molecules desorb, whereas the cross-linked structures remain on the surface. TDL is a simple and efficient method to create molecular patterns in a vacuum environment. Fig.5-11 shows scanning electron microscopy (SEM) and atomic force microscopy (AFM) images of 1  $\mu\text{m}$  circles made by electron (100 eV) exposure of a BPT SAM through a stencil mask (Quantifoil) in high vacuum ( $p < 5 \times 10^{-7}$  mbar) at room temperature and subsequent thermal desorption of the non-cross-linked regions in UHV at 620 K and 1050 K. The SEM measurements were conducted *in situ*; the AFM study was performed *ex situ* in air. Both techniques clearly show the presence of the cross-linked monolayer pattern on gold produced by selective thermal desorption. AFM line scans confirm the expected thickness of  $\sim 1$  nm of the cross-linked BPT SAM. As cross-linked aromatic SAMs can be fabricated by e-beam lithography with a resolution below 40 nm<sup>[53]</sup>, TDL may be capable to fabricate temperature stable surface carbon nanostructures with a similar resolution. Regions not covered by the cross-linked SAMs may be used for the adsorption of other molecules, to generate a chemically diverse.

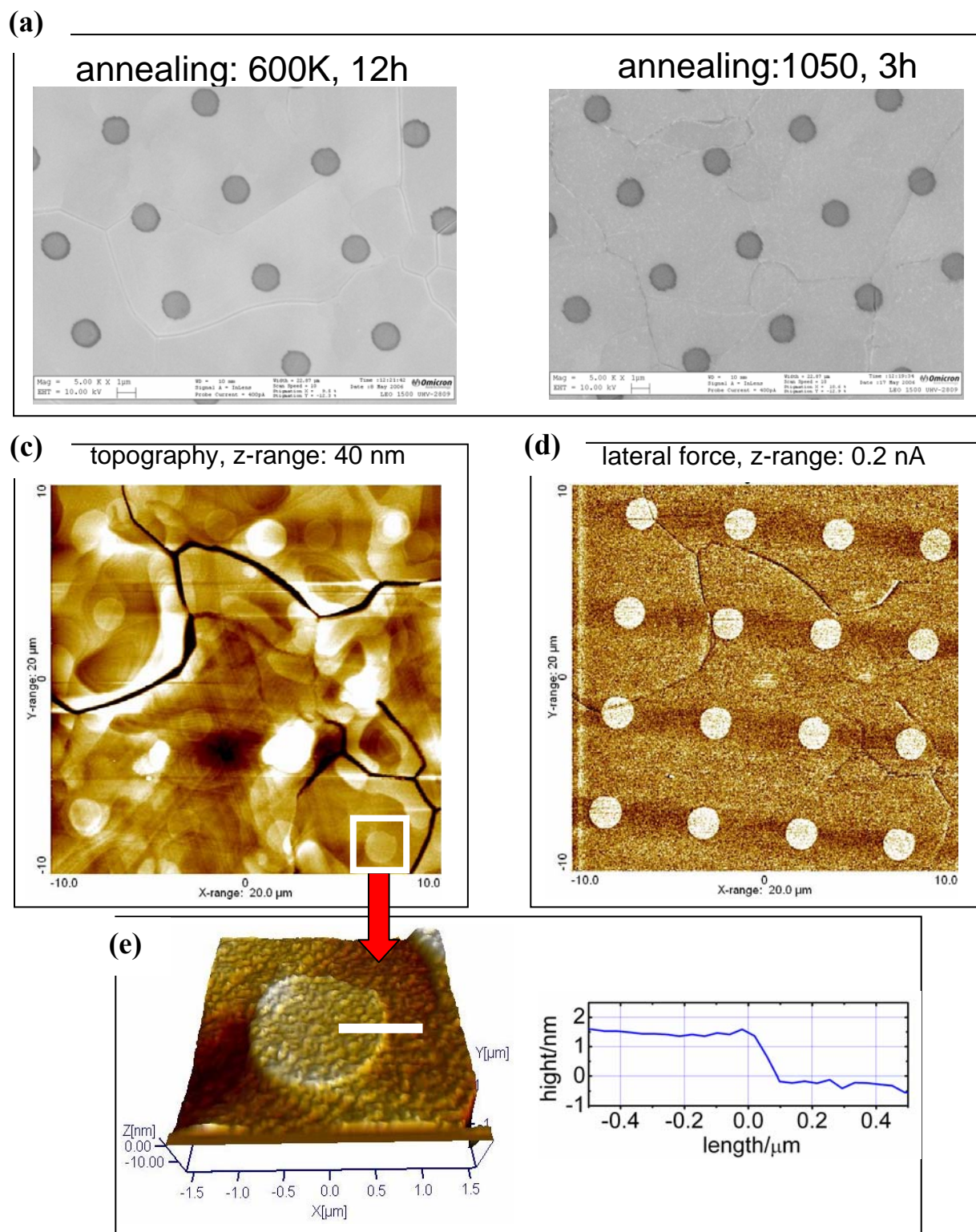
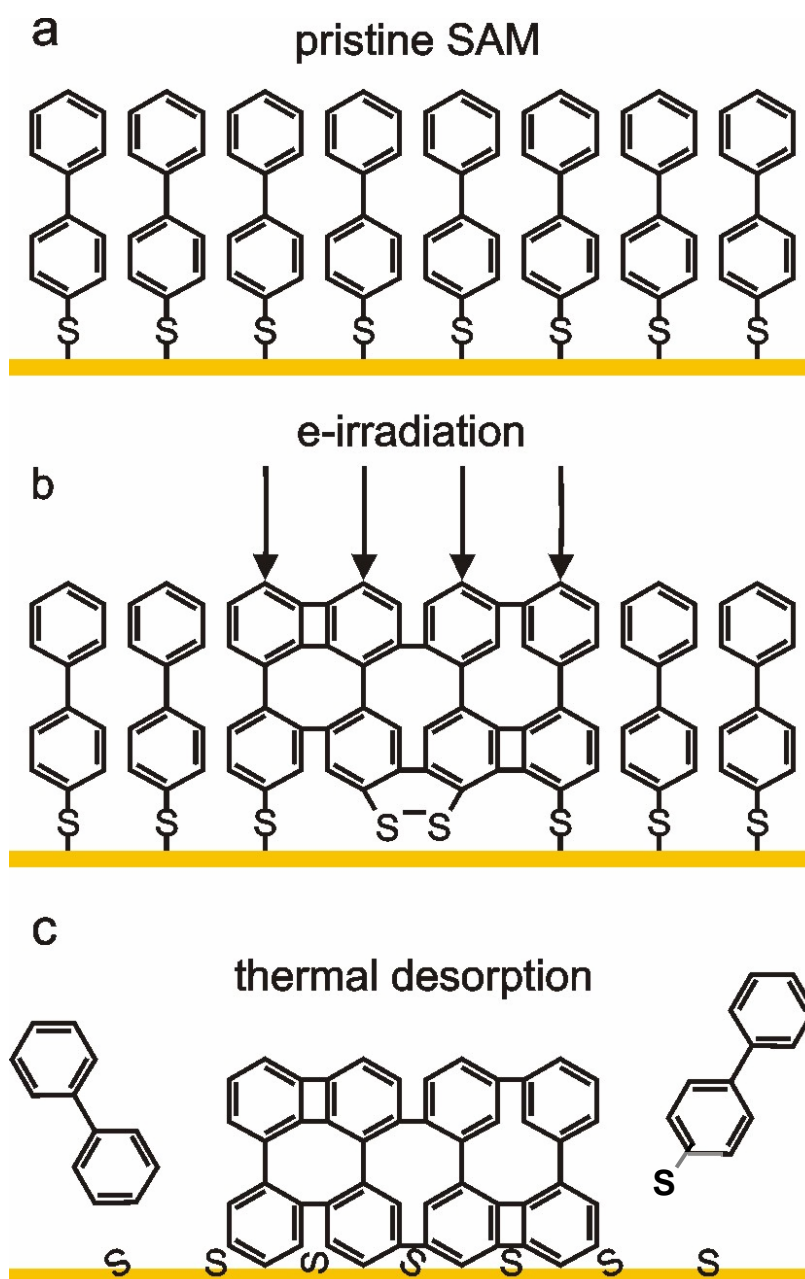


**Fig.5-11.** Molecular pattern by selective desorption (600K and 1050k) of an e-beam processes BPT SAM on Au (111) surface. (a) SEM micrograph (10 keV, 400pA). (c) and (d) AFM topography and lateral force micrograph. (e) AFM topography micrograph and line profile across the cross-linked BPT monolayer of the inset in contact mode measurements



In conclusion, we have shown an extremely high (up to 1000 K) thermal stability of cross-linked aromatic self-assembled monolayers on Au surfaces. This is the highest thermal stability which has been reported for monomolecular films on surfaces. Desorption of pristine Biphenylthiol SAMs occurs already at temperatures above 400K via C-S bond breaking and desorption thiolate. Thermal processing of e-beam patterned Biphenylthiol SAMs results in the fabrication of monomolecular pattern by selective thermal desorption. The reported results are not limited to the studied model system but can be extended to other aromatic SAM

## *Section C*

### *Thermal stability of pristine and cross-linked nitrobiphenylthiol (NBPT)*

NBPT SAMs show by electron irradiation not only cross-linking of the aromatic units but also their terminal nitro groups are converted to the amino groups. This functionalization can be used for creation of chemical patterns by e-beam lithography<sup>[26-29]</sup>. In this section we investigated thermal stability of pristine and cross-linked NBPT.

#### **1- Characteristic of pristine nitrobiphenylthiol (NBPT) as a function of temperature:**

We annealed pristine NBPT/Au from RT to 250°C with 20°C increment. Fig.5-12, Show the ARXPS measurement of NBPT. Angular dependence of the S2p, C1s, N1s, and O1s signal exhibit the correct longitudinal structure of a NBPT monolayer. Fig.5-13 and 5-14 show the S2p, C1s, N1s and O1s XP spectra of NBPT/Au as a function of temperature. From the attenuation of the Au 4f signal, we calculated the thickness of the pristine SAM to 12.5±0.8 Å. At room temperature (RT) the S2p signal shows a doublet peak at binding energies (BEs) of 162.0 and 163.2 with a full width at half maximum (FWHM) of 0.9 eV, which is characteristic for thiolate. The C1s signal of the NBPT SAM consists of a main peak, C1s(I), at 284.2 eV (FWHM=1.2 eV) that is assigned to the 10 adjacent carbon atoms in the aromatic rings, a C1s(II) peak at 285.3 eV (FWHM=1.4 eV) that originates from the carbon atoms in C-S and C-N bonds, and of aromatic shake-up satellites at 287.0 eV and 290.5 eV (FWHM=1.7 eV). The N1s and O1s signals at 405.5 eV (FWHM=1.4 eV) and 532.3 eV (FWHM=1.7 eV), respectively, are assigned to the SAMs terminal nitro group.

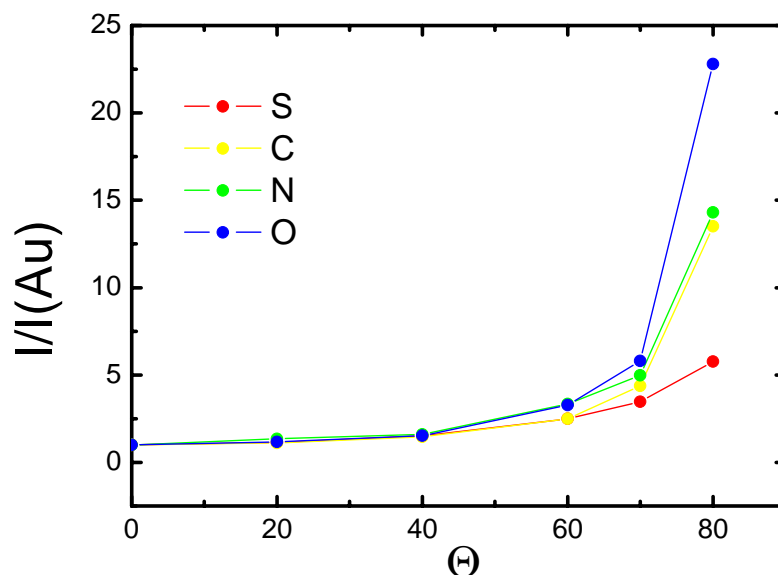


**Fig.5-12.** the ARXPS measurement of NBPT.

As can be seen from Fig.5-13, sulphide/disulfide signals formed at temperature above 400 K in S2p Xp spectra Fig.5-13. Their intensity increase at temperature above 543K (see Fig.5-14). At 453K the atomic sulphur peak forms and increases with raising the temperature. At 558K the atomic sulphur becomes a dominant signal in S2p peak. At the same time the intensity of thiolate bond decreases with increasing temperature and disappear completely at temperature above 476K. The C1s signal in the Fig.5-13, C1s decreases with raising temperature and shows only 45% of its initial intensity at 558K, Fig5-14. At 453K the binding energy of the aromatic [C1s(I)]species shifts by ~ 0.30 eV to higher binding energy. The C1s(II) signal decreases with increasing temperature which is in agreement with the by decreasing amount of thiolate signals and sulphide/disulfide bonds.

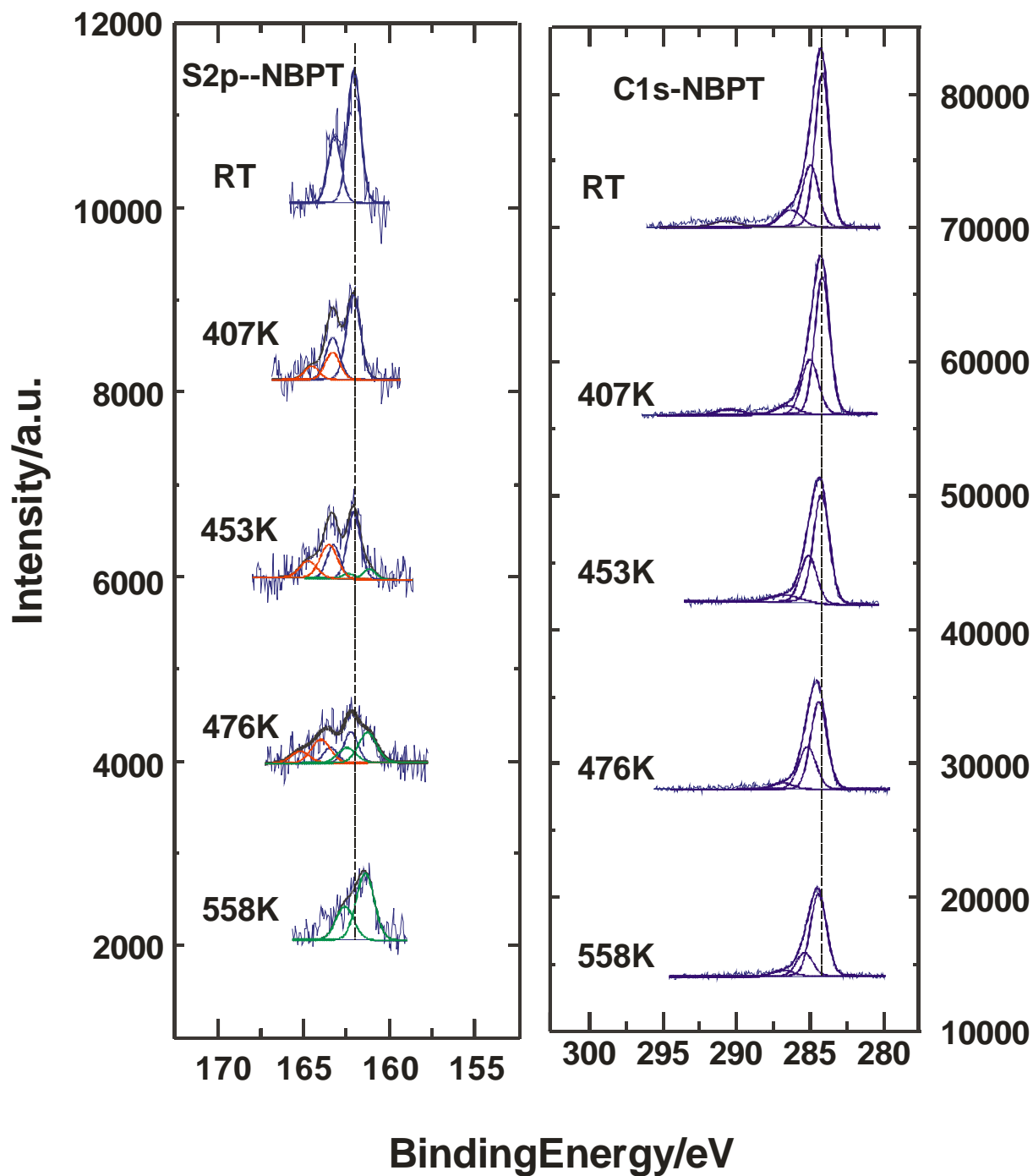
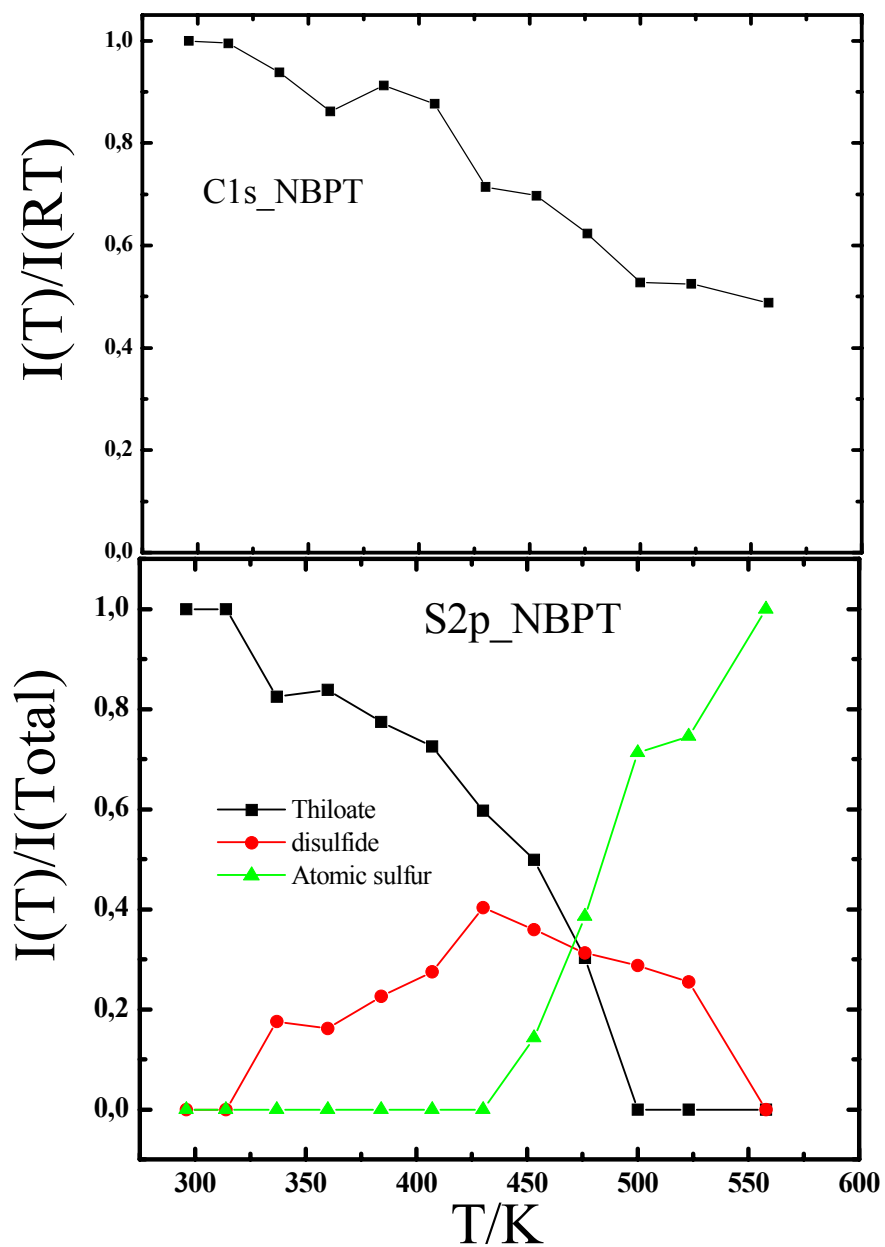


Fig.5-13. XPS spectra of S2p and C1s signals NBPT as a function of temperature.



**Fig.5-14.** Relative peak intensities of S2p and total C1s signal intensity as a function of temperature.

The O1s and N1s XP spectra of the NBPT/Au are presented in Fig.5-15. In the N1s signal, at room temperature there is a single peak at 405.5eV denoted as nitro peak. Above 400K, another N1s peak forms at 399.3eV (FWHM=1.7eV). At 407K the component 405,5 eV(nitro group) decreases, which suggests the loss of some nitrobiphenyl moieties. This process continues upon heating to 453k where another peak at 399.3eV grows. At higher temperature (558K) the N1s (399.3eV) remains at the surface with somewhat decreased intensity, showing a transformation of the nitrogen species occurred. In the O1s XP spectra for the pristine NBPT/Au, a single O1s emission at 532.3 eV FWHM=1.70eV, which assigned as nitro group, is observed at room temperature. At 407K small peak appears at low binding energy of 530.5eV with FWHM=1.70eV. Above 450K the 530.5eV peak increases and decreases the peak at 532.3eV decreases. The N1s can be fitted with two nitrogen species at 399.3 and 400.8eV, which are characteristic of amine and a protonated amine group<sup>[88]</sup>, respectively. and N1s oxide NO<sup>[89]</sup> at 397.6eV Fig.5-16 shows the relative intensity of the N1s and O1s species as a function of temperature. The nitro group decreases below 400K the amine group decreases above 400k. The protonated and NO peaks growth with increasing temperature. At 558K the NO intensity has a maximum which is confirmed by increase of NO contribution in O1s and disappearance of peaks for protonate and not protonate amine group.

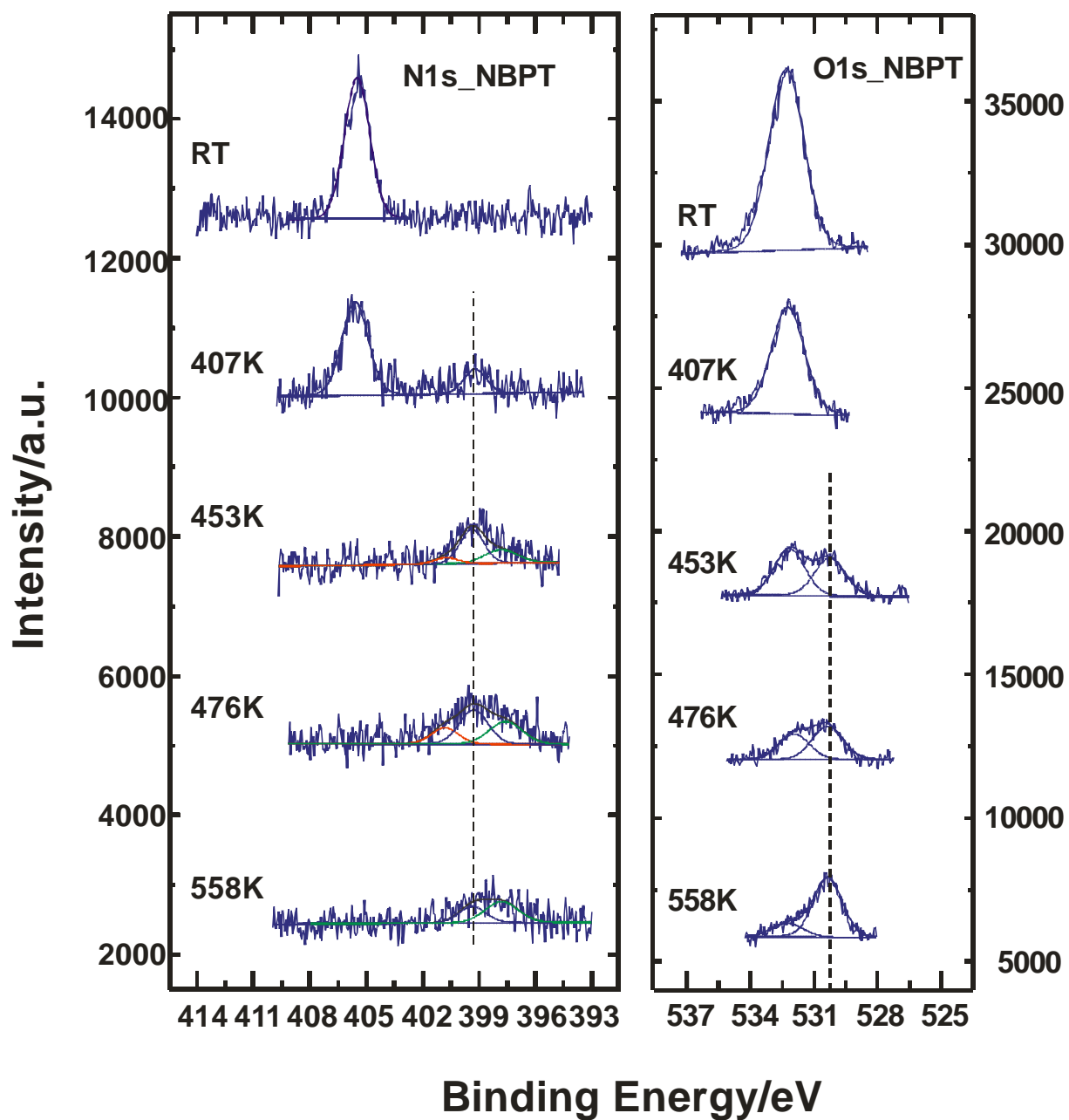
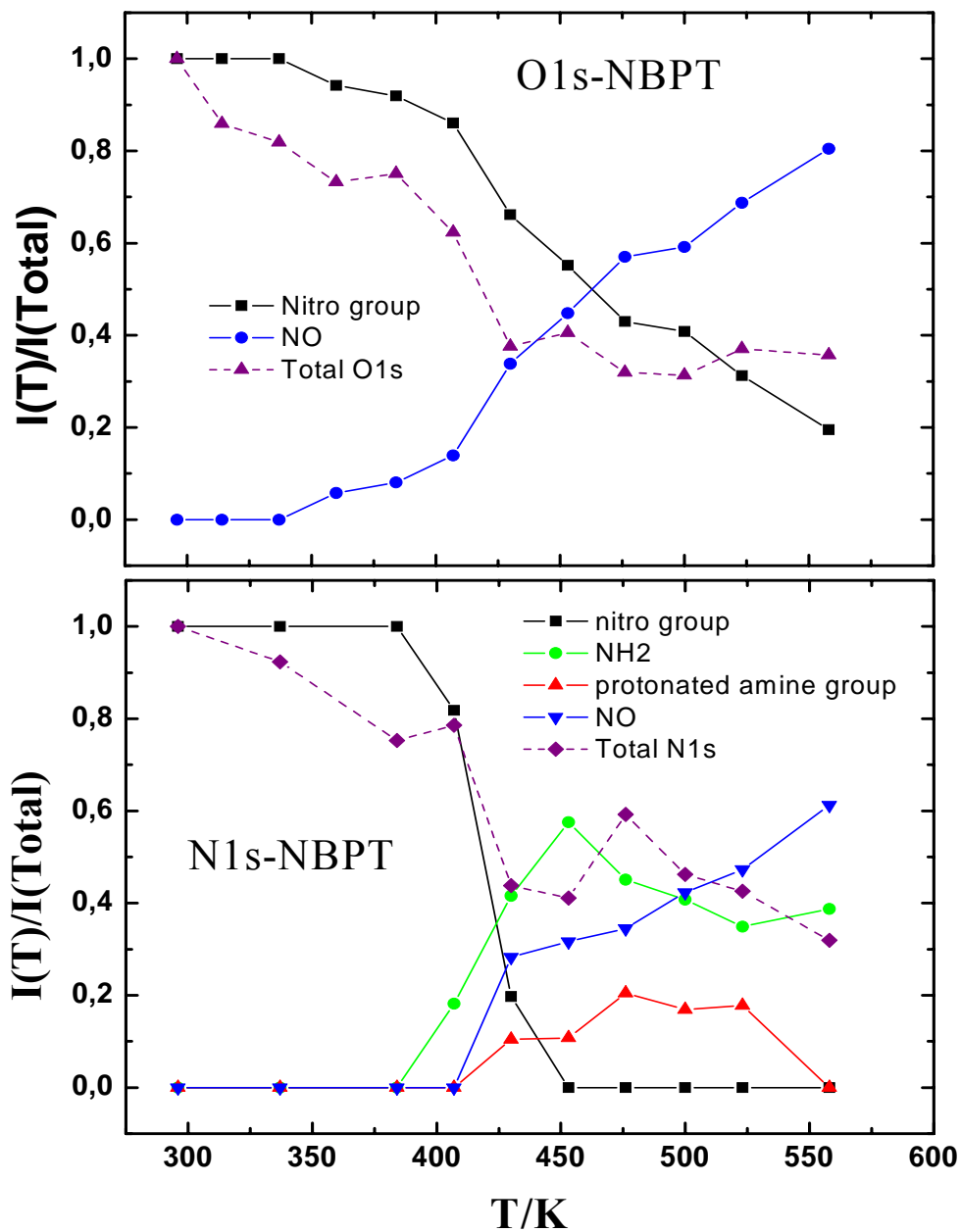


Fig.5-15. XPS spectra of N1s and O1s signals of NBPT as a function of temperature.



**Fig.5-16.** Relative peak intensities of O1s and N1s signals intensity as a function of temperature.

Although XPS has been widely used to obtain information on the formation and composition of films, several studies have demonstrated that x-rays induce damage and modification of SAMs<sup>[90-98]</sup>. This damage can either limit the utility of x-ray irradiation or be used as a lithographic approach to pattern surfaces<sup>[99]</sup>.

Kim and co-workers<sup>[100]</sup> studied visible laser light irradiation effects on nitro-terminated monolayers on silver. The results indicated the conversion of the nitro group to amine functionality by laser irradiation, preserving the overall structural integrity of the monolayer. Grunze and co-workers<sup>[36]</sup> investigated NO<sub>2</sub>-terminated biphenyl SAMs on gold substrates. They reported the transformation of surface nitro groups to amine groups by low energy electron irradiation while the underlying aromatic layer is dehydrogenated and cross-linked. They suggested that the hydrogen atoms required for reduction of the nitro groups are generated by the electron-induced dissociation of the C–H bonds in the biphenyl units. Where in S2p signal have sulphide/disulfide peak. Preece and coworkers<sup>[101]</sup> investigate the influence of x-ray irradiation on 3-(4-nitrophenoxy)-propyltrimethoxysilan (NPPTMS) at different irradiation times. At longer irradiation times 447min, almost all NO<sub>2</sub> groups under irradiation converted to NH<sub>2</sub> groups.

Taking into consideration these previous studies and from our results there a possibility that the transition from nitro to amino occurs by X-ray irradiation. The evidences for this possibility are the formation of sulfide/disulfide peaks, which is similar to the effect of e-beam irradiation as shown in Fig.5-7, the C1s 45% of initial intensity total carbon stay on the surface similar to C1s at electron dose of 25mC/cm<sup>2</sup> of irradiated BPT, Fig5-10 in section B. The exposure time of our sample to x-ray is ~ 200 min and depending on the results from ref.[101] at this time the transformation occurred.

Another possibility for this conversion is the influence of the temperature. The evidences of this possibility are we used Monochromatic XPS for measuring, we measured another NBPT/Au sample to reduce the exposure time to X-ray by measuring the sample from RT to 150 °C directly, the same transformation occurs. NO signal formed and the O:N ratio does not change where the total intensity of O1s and N1s approximately the same at 558K as shown in Fig5-16. We assume the nitro group

converted to amino group because of the effect of heating NBPT-SAM. Such transformations confirmed by appearance of NO peak in O1s signal.

### **1- Characteristic of cross-linked nitrobiphenylthiol (NBPT) as a function of temperature:**

Irradiation of NBPT SAMs with electrons results in the lateral cross-linking of adjacent aromatic molecules and in the conversion of the terminal nitro groups into the amino groups<sup>[36]</sup>. These changes can be seen in the XP spectra, Fig.5-17. The N1s region shows the formation of a new signal at 399.0 eV, accompanied with a low intensity shoulder at 400.8 eV, and the nitro signal at 405.5 eV disappears completely. Similar to biphenylthiol SAMs upon irradiation<sup>10</sup> a broadening of the C 1s signals by ~0.3 eV is observed. The S2p signal shows the formation of a second doublet at higher binding energies (~163.5 and 164.7, FWHM~1.5 eV), which is indicative for the formation of sulfide or disulfide in the cross-linked SAM. The O1s signal decreases to ~20 % of its initial value. As expected from the enhanced N:O ratio in the pristine SAM, the residual oxygen may result from impurity during prepared the sample. The thickness of the SAM decreases by ~1 Å, which is in agreement with the oxygen loss.

The behaviour of cross-linked NBPT/Au is similar to cross-linked BPT/Au. Fig.5-17 and 5-18 show the C1s and S2p as a function of temperature. While the atomic sulphur is formed above 400K and growth with increasing temperature the total C1s has small decrease at the same temperature and shows 75% of the initial intensity without changing the binding energy of the aromatic species as at the room temperature as shown in Fig.5-18.

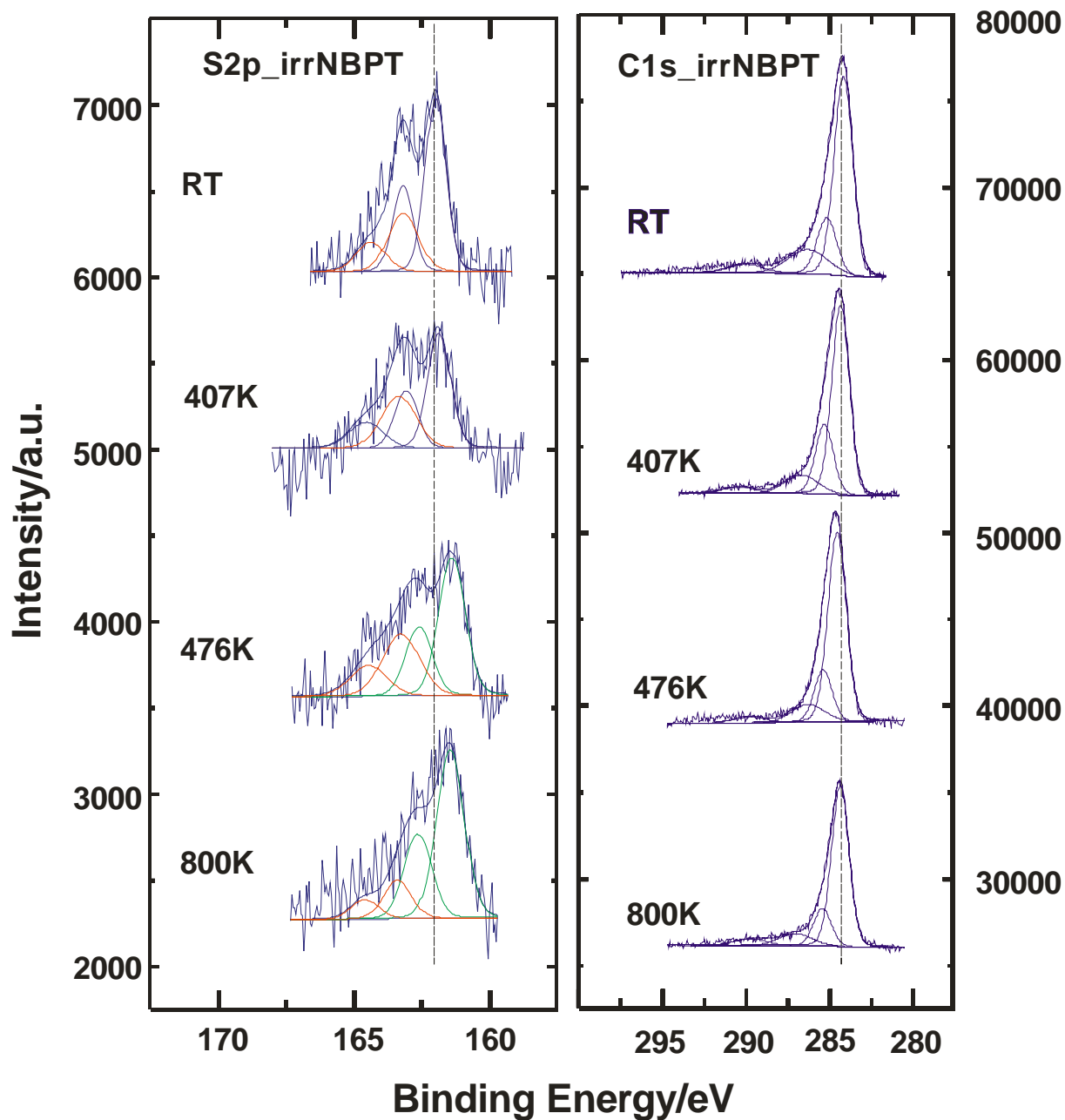


**Fig.5-17.** XPS spectra of S2p and C1s signals irradiated ( $45\text{mC}/\text{cm}^2$ ) NBPT as a function of temperature.

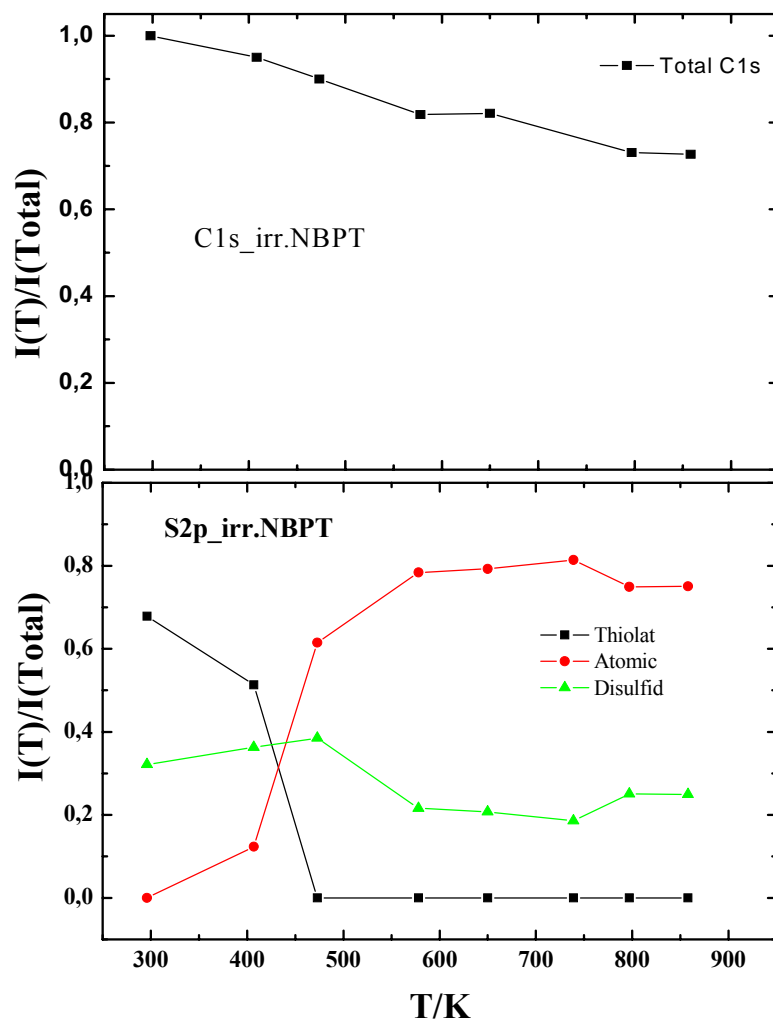


**Fig.5-18.** Relative peak area of S2p and total C1s signal intensity of cross-linked NBPT as a function of temperature.

At room temperature (RT) the N1s XPS spectra shows the formation amino group(NH<sub>2</sub>) at binding energy 399.3 with low intensity shoulder at 400.8 eV which is characteristic as protonated amine group (NH<sub>3</sub>) as shown in Fig5-19a.

Figure 23b shows relative intensity of N1s species where below the temperature at 400K a little decreases occurred in the N1s intensity. The total N1s intensity remain above 50% of its initial intensity up to highest temperatures and the total N1s peak shifted 1 eV to lower binding energy.

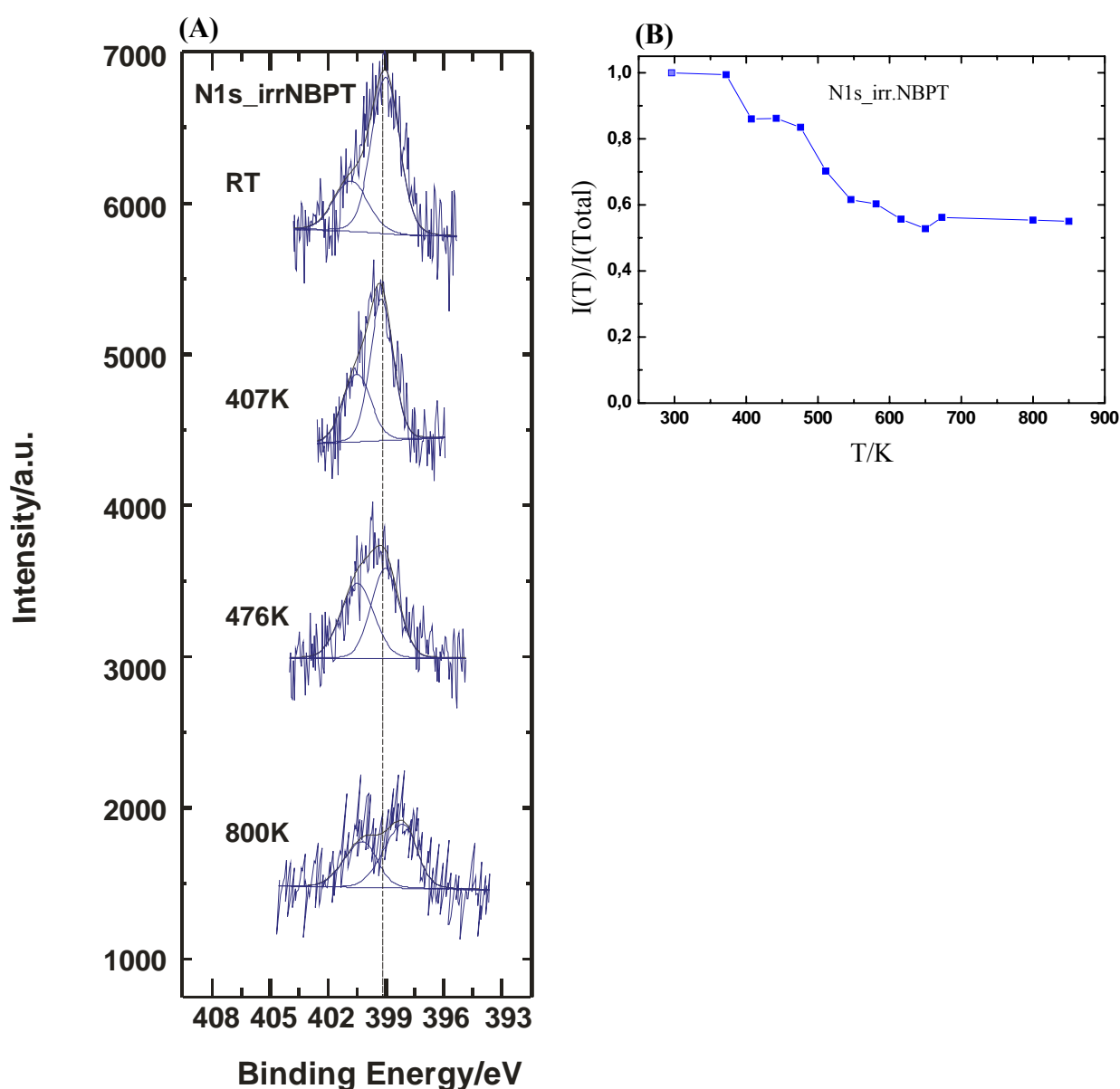


**Fig.23.** (A) XPS spectra of S2p and C1s signals of cross-linked NBPT (45mC/cm<sup>2</sup>).

(B) Relative peak area of N1s species intensity as a function of temperature.

## *Chapter6*

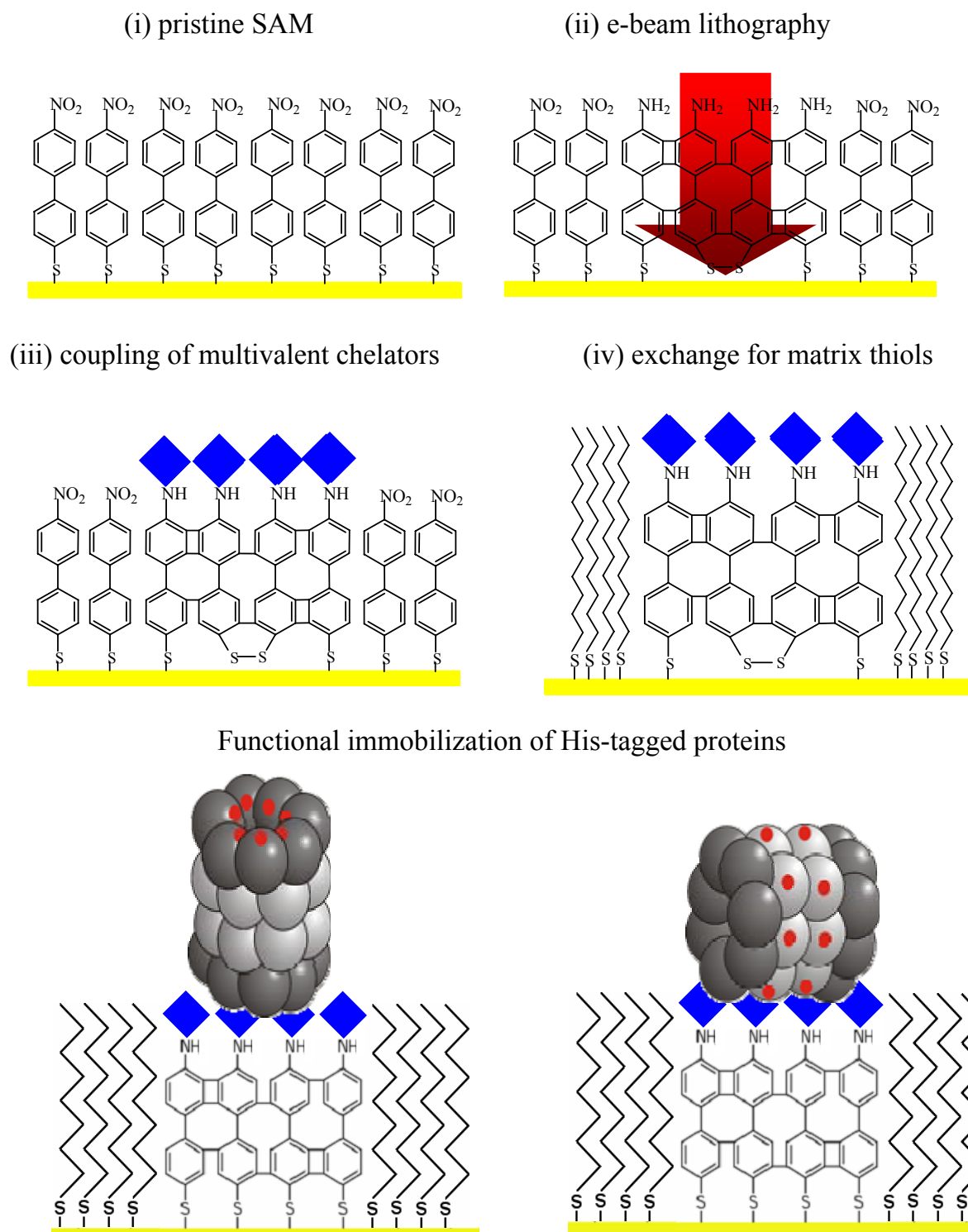
# **High-Affinity Protein Chip Fabrication by Chemical E-Beam Nanolithography**

## 1- Introduction

To study protein function and interaction, there is a high demand for specific, stable, locally immobilized, and functional protein arrays on solid substrates. In this chapter, we present a new concept to the fabrication of solid templates for laterally defined and functional immobilization of proteins for chip applications. The biochip fabrication is based on the combination of electron induced chemical lithography with aromatic self-assembled monolayers (SAMs) and the NTA/His-tag concept<sup>[102]</sup>, merging classical electron beam nanolithography (top-down) with molecular self-assembly (bottom-up) and chemical biology. Scheme 1a presents the different elemental steps of the protein chip assembly:

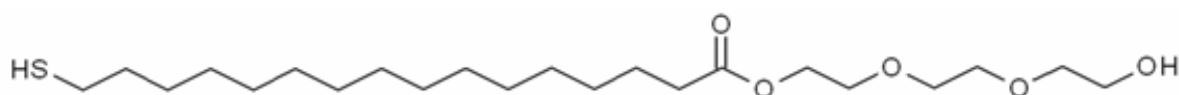
- i.** Formation of nitrobiphenyl thiol SAM: First, a densely packed monolayer of 4'-nitro-1,1'-biphenyl-4-thiol (NBT) was self-assembled on a gold surface.
- ii.** Chemical nanolithography: E-beam writing was used to locally reduce the terminal nitro groups to amino groups, while the aromatic layer is dehydrogenated and cross-linked. The generated well-ordered templates of amino groups can be used for specific covalent coupling of biological recognition units like tris-NTA.
- iii.** Chemical coupling of tris-NTA modules to reduced amino-terminated SAMs: The amino groups of the remaining and cross-linked biphenyl thiols are modified by coupling of *tert*-butyl protected carboxy-tris-NTA modules (Scheme 1c). After deprotection with TFA, the surfaces were applied for specific, high-affinity immobilization of His-tagged proteins.
- iv.** Exchange of non-cross-linked thiols by protein-repellent matrix thiols: This exchange reaction was aimed to improve the protein-repellent properties of the structured SAM. Non cross-linked NBTs were thermally desorbed and replaced by protein-repellent EG3 matrix thiol (Scheme 1b). Arrays with the grafted multivalent chelators result in the specific, high affine, oriented and reversible immobilization of His-tagged proteins or even protein complexes.

(a)

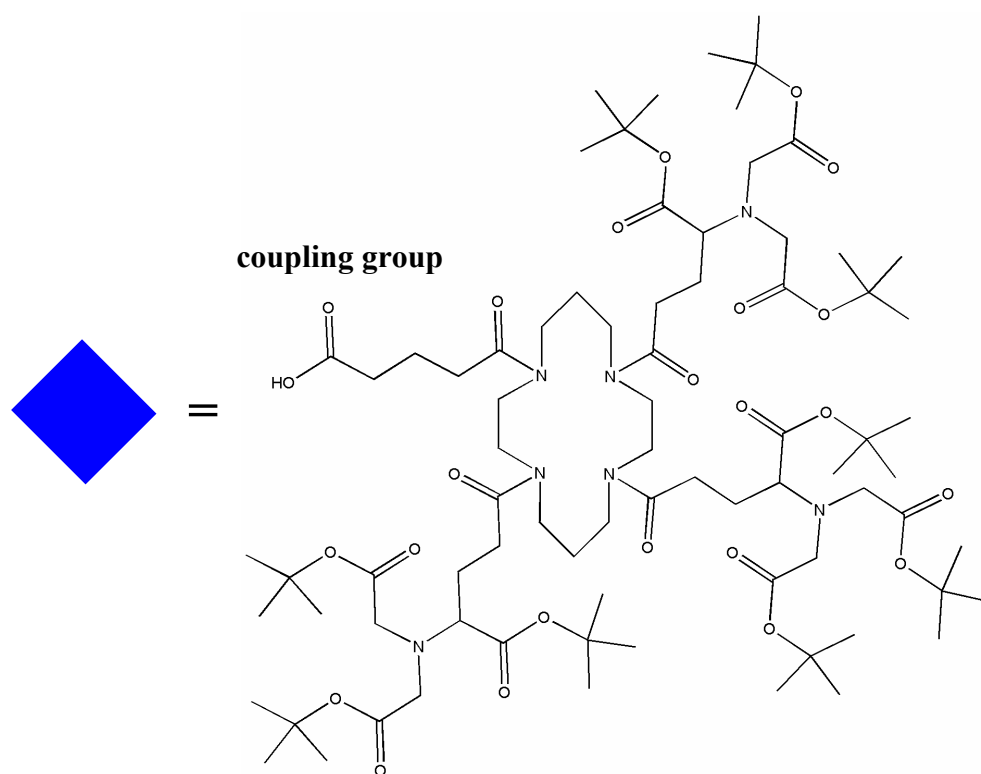


**Scheme 6-1.** (a) Schematic representation of the protein chip assembly, (i)-(iv); Controlled immobilization of His-tagged protein complexes (here: proteasome) in either end-on (v) or side-on (vi) orientation.

(b) matrix thiol



(C) multivalent chelator



Scheme 6-1. (b) Protein repellent EG3-OH matrix thiols. (c) Multivalent tris-NTA chelator with protected carboxyl functionality.

## 2- XPS measurements:

The XPS measurements of different steps of the protein chip assembly were carried out, the XP spectra of pristine is shown in Fig.6-1a. The spectra of e-beam irradiated ( $40 \text{ mC/cm}^2$ ) NBPT SAMs is shown in Fig.6-1b (steps (i)-(ii) in Scheme 1a). From the attenuation of the Au 4f signal (not shown), we calculated the thickness of the pristine SAM to  $12.5 \pm 0.8 \text{ \AA}$ . The S2p signal shows a doublet at binding energies (BEs) of 162.0 and 163.2 with a full width at half maximum (FWHM) of 0.9 eV, which is characteristic for thiolate<sup>[84]</sup>. The C1s signal of the NBPT SAM consists of a main peak, C1s(I), at 284.2 eV (FWHM=1.2 eV) that is assigned to the 10 adjacent carbon atoms in the aromatic rings, a C1s(II) peak at 285.3 eV (FWHM=1.4 eV) that originates from the carbon atoms in C-S and C-N bonds, and of aromatic shake-up satellites at 287.0 eV and 290.5 eV (FWHM=1.7 eV). The N1s and O1s signals at 405.5 eV (FWHM=1.4 eV) and 532.3 eV (FWHM=1.7 eV), respectively, are assigned to the SAMs terminal  $\text{NO}_2$  group. Derived from the XP spectra a somewhat higher, in comparison to the stoichiometrical ratio, value of nitrogen to oxygen atoms,  $\sim 1:2.5$ , was observed. It may be indicative for the formation of a co-adsorbate overlayer on the polar nitro groups during the air contact of the samples. The evaluation of the chemical composition of the monolayer and additional angle resolved XPS measurements indicate the formation of a densely packed NBPT SAM on polycrystalline Au surfaces and the surface location of the nitro groups.

Irradiation of NBPT SAMs with electrons results in the lateral cross-linking of adjacent aromatic molecules and in the conversion of the terminal nitro groups into the amino groups<sup>[36]</sup>. These changes can be seen in the XP spectra, Fig.6-1b. The N1s region shows the formation of a new signal at 399.0 eV, accompanied with a low intensity shoulder at 400.8 eV, and the nitro signal at 405.5 eV disappears completely. Similar to biphenylthiol SAMs upon irradiation<sup>[103]</sup> a broadening of the C 1s signals by  $\sim 0.3 \text{ eV}$  is observed. The S2p signal shows the formation of a second doublet at higher

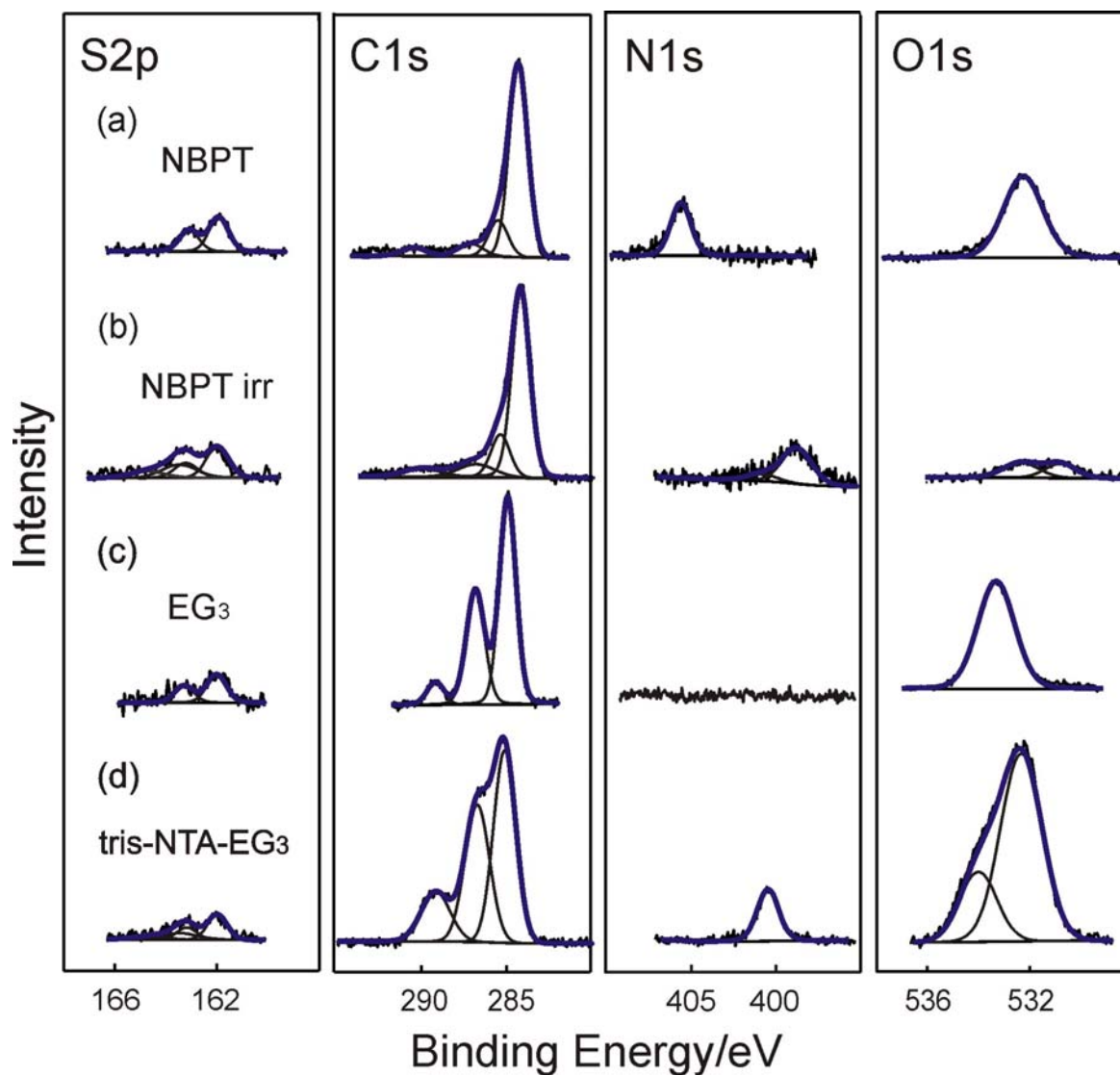


**Fig.6-1.** XPS spectra of the sulfur, carbon, nitrogen and oxygen regions of (a) NBPT SAM, (b) irradiated NBPT SAM ( $40\text{mC}/\text{cm}^2$ ), (c) EG<sub>3</sub>-OH SAM and (d) EG<sub>3</sub>-tris-NTA SAM.

binding energies ( $\sim 163.5$  and  $164.7$ , FWHM $\sim 1.5$  eV), which is indicative for the formation of sulfide or disulfide in the cross-linked SAM. The O1s signal decreases to  $\sim 20$  % of its initial value. As expected from the enhanced N:O ratio in the pristine SAM, the residual oxygen may result from co-adsorbate. The thickness of the SAM decreases by  $\sim 1$  Å, which is in agreement with the oxygen loss. It is interesting to that the air exposure of the irradiated NBPT SAMs results in an increase of their effective thickness by  $\sim 2$  Å, which is accompanied also by increase the O1s signal intensity to  $\sim 70$  % of its initial value, and a noticeable  $\sim 5$ % increase of the carbon intensity.

The nitrogen intensity is not affected by the air exposure implying possible incorporation of the oxygen and carbon atoms into the carbon skeleton of the cross-linked SAM. This effect was taken into account for further evaluation of the data. The ARXPS show the surface location of the amino groups.

Fig.6-1c shows XP spectra of an EG3-OH thiol monolayer. The S2p signal is a thiolate doublet at  $162.1$  eV and  $163.3$  eV (FWHM $=0.9$  eV). The carbon signal consists of three constituents: the C1s(I) peak at  $285.1$  eV (FWHM $=1.2$  eV) accounting for carbon atoms in the alkyl groups; the C1s(II) peak at  $287.0$  eV (FWHM $=1.3$  eV) accounting for carbon atoms in the tri(ethylene glycol) groups; and the C1s(III) peak at  $289.4$  eV (FWHM $=1.2$  eV) reflecting the carbon atom in the carboxyl group. The O1s signal is a single peak at  $533.3$  eV (FWHM $=1.7$  eV). The surface location of the tri(ethylene glycol) groups in the SAM is clearly shown from the C(I)/C(II) ratio, which is  $\sim 15:9$ , whereas the stoichiometrical ratio is  $15:6$ . The effective thickness of the EG3-OH SAM is  $26.1 \pm 1.1$  Å. This value is lower than the thickness of for an ideal EG3-OH monolayer with the helical conformation ( $\sim 28.5$  Å)

(evaluation has been made on the basis of the data presented in Ref.104), which may account for some structural defects in a real SAM.

To determine the positions of the characteristic XP peaks in tris-NTA units, Schema 1c, we studied EG3-tris-NTA SAMs as a reference. Due to steric reasons the formation of a densely packed monolayer is not expected. Hence, the S2p spectrum contains the thiolate doublet and sulfur species at higher binding energies. The effective thickness of the EG3-tris-NTA SAM corresponds only to  $26.8 \pm 1.4$  Å. The different XP peaks in Fig.6-1d are assigned to components in the tris-NTA units. The C1s signal at 285.1 eV (FWHM=1.6 eV), 286.8 eV (FWHM=1.7 eV) and 289.2 eV (FWHM=2.0 eV) are attributed to alkyl groups, carbon in C-N bonds and carboxyl groups, respectively. The higher FWHM values, in comparison to the similar signals in the EG3-OH SAM, results from highly disordered structure of the EG3-tris-NTA SAM. The O1s signal in the carboxyl groups is assigned to the BE of 532.4 eV (FWHM=1.9 eV). The N1s signal in the amino groups of the NTA units shows the BE of 400.5 eV (FWHM=1.5 eV), which is shifted by 1.5 eV to higher BE in comparison to the amino groups of the cross-linked aromatic SAM.

Using of the above spectroscopic information a detailed analysis of the steps (iii) and (iv) of the protein chip assembly is possible. Fig.6-2 presents a summary of the “exchange experiments” which were conducted at room temperature, Scheme 1a (iv). The XPS data show, that the pristine NBPT SAM can be completely exchanged in solution against the protein repellent EG3-OH SAM (where the pristine NBPT SAMs on the chip surface have been exchanged against matrix thiol in 1 mM solution of EG<sub>3</sub> in ethanol or DMF at room temperature). The effective thickness of the formed EG3-OH SAM ( $23.4 \pm 1.5$  Å) indicates a somewhat higher degree of disorder in the monolayer in comparison to the EG3-OH SAM prepared on a bare Au surface. As

judged from the changes of the effective thickness and disappearance of the N1s signal in the XP spectra, the complete exchange occurs within ~4-5 days, Fig.6-2. A simple 1<sup>st</sup> order kinetic equation describes the experimental data well and gives for the exchange rate constant a value of  $0.06 \pm 0.2 \text{ h}^{-1}$ .

$$-\partial(d(t)-d_{\text{NBPT}})/\partial t = k(d(t)-d_{\text{NBPT}})$$

where  $d(t)$  is the monolayer thickness as a function of time;  $t$  is the time;  $d_{\text{NBPT}}$  is the thickness of the NBPT monolayer at  $t=0$ ; and  $k$  is the exchange rate constant.

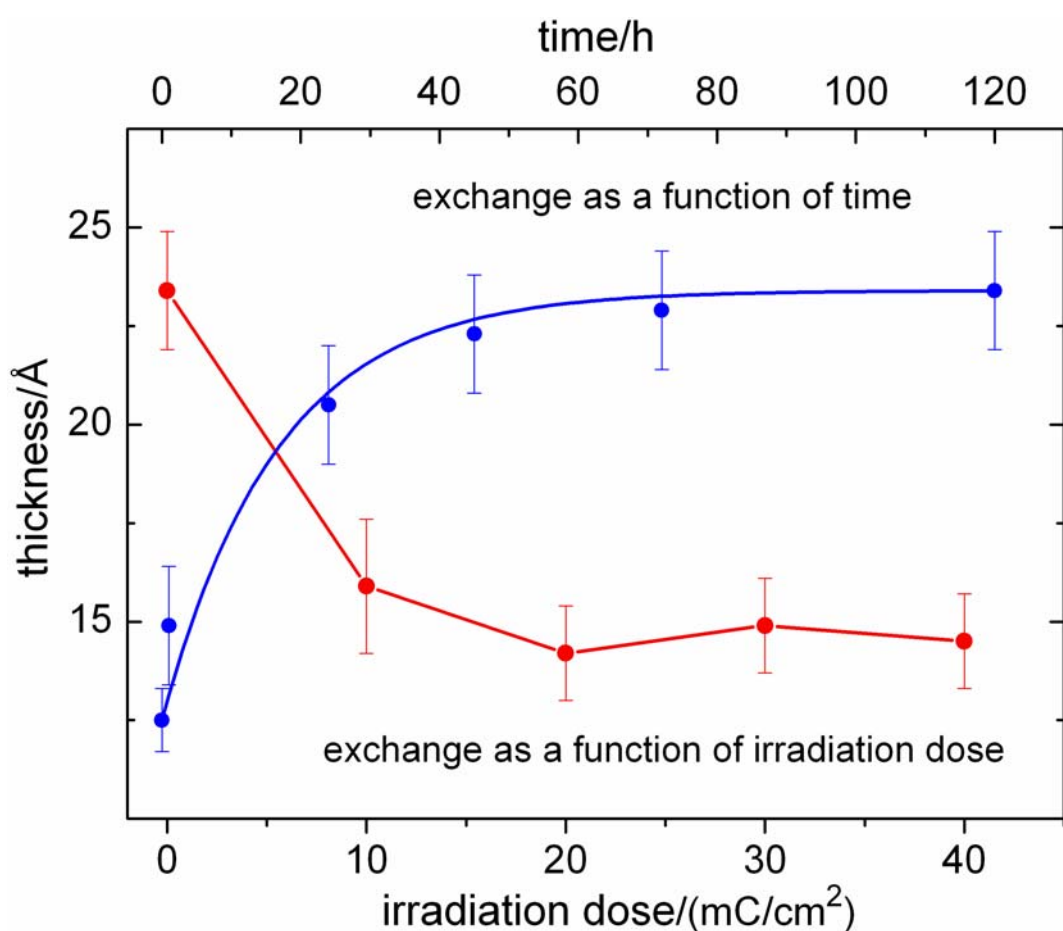


**Fig.6-2.** Exchange of the NBPT SAM against the protein resistant EG3-OH SAM in solution at room temperature as a function of time and irradiation dose.

Unlike the pristine SAM, the cross-linked monolayer shows a high resistance to the exchange with EG3-OH molecules. After 5 days in an EG3-OH solution, the XP spectra of SAMs with electron doses above  $10 \text{ mC/cm}^2$  are almost unchanged. Only a little broadening of the C1s signal and increase of the effective thickness by  $\sim 1.5 \text{ \AA}$  is observed, which obviously results from the incorporation of EG3-OH molecules to defects in the cross-linked SAM.

Fig.6-3 presents the results for grafting of tris-NTA units (Fig. 6-1c) on the amino terminated surfaces of electron irradiated NBPT SAMs. Above a dose of  $10 \text{ mC/cm}^2$  the thickness of the grafted layer was found to be  $\sim 6 \text{ \AA}$ . Such a dose dependent growth of the overlayer correlates well with the generation of amino groups in the underlying SAM upon irradiation. In view of the detailed spectroscopic information on the constituents of the tris-NTA units, their stoichiometry, the thickness of the grafted overlayer, Fig. 6-3a clearly shows the coupling of tris-NTA to the cross-linked SAM. The stoichiometry of the grafted overlayer derived from the XP spectra within a statistical model<sup>[105]</sup>, suggests a C:O:N ratio of 11.2:3.5:1, which correspond very good with the expected value of 11.1:3.4:1. The intensity ratio, between the N1s signal in tris-NTAs and in the cross-linked SAM, shows that the coupling of the multivalent chelator occurs at about each tenth molecule of the SAM. That corresponds to the formation of a monolayer of multivalent chelator on top of the cross-linked SAM as can be judged from the size of tris-NTA units. The chelating of Ni(II) ions to the deprotected NTA groups is confirmed by the appearance of a Ni2p<sub>3/2</sub> signal at 856.3 eV. In comparison to metallic nickel, the peak position is shifted by  $\sim 3.3 \text{ eV}$  to higher BEs<sup>[80]</sup>. The chelating efficiency of tris-NTA units evaluated from N1s and Ni2p<sub>3/2</sub> signals, is  $\sim 2.7$  Ni atoms per multichelator (the maximal theoretical value is 3).

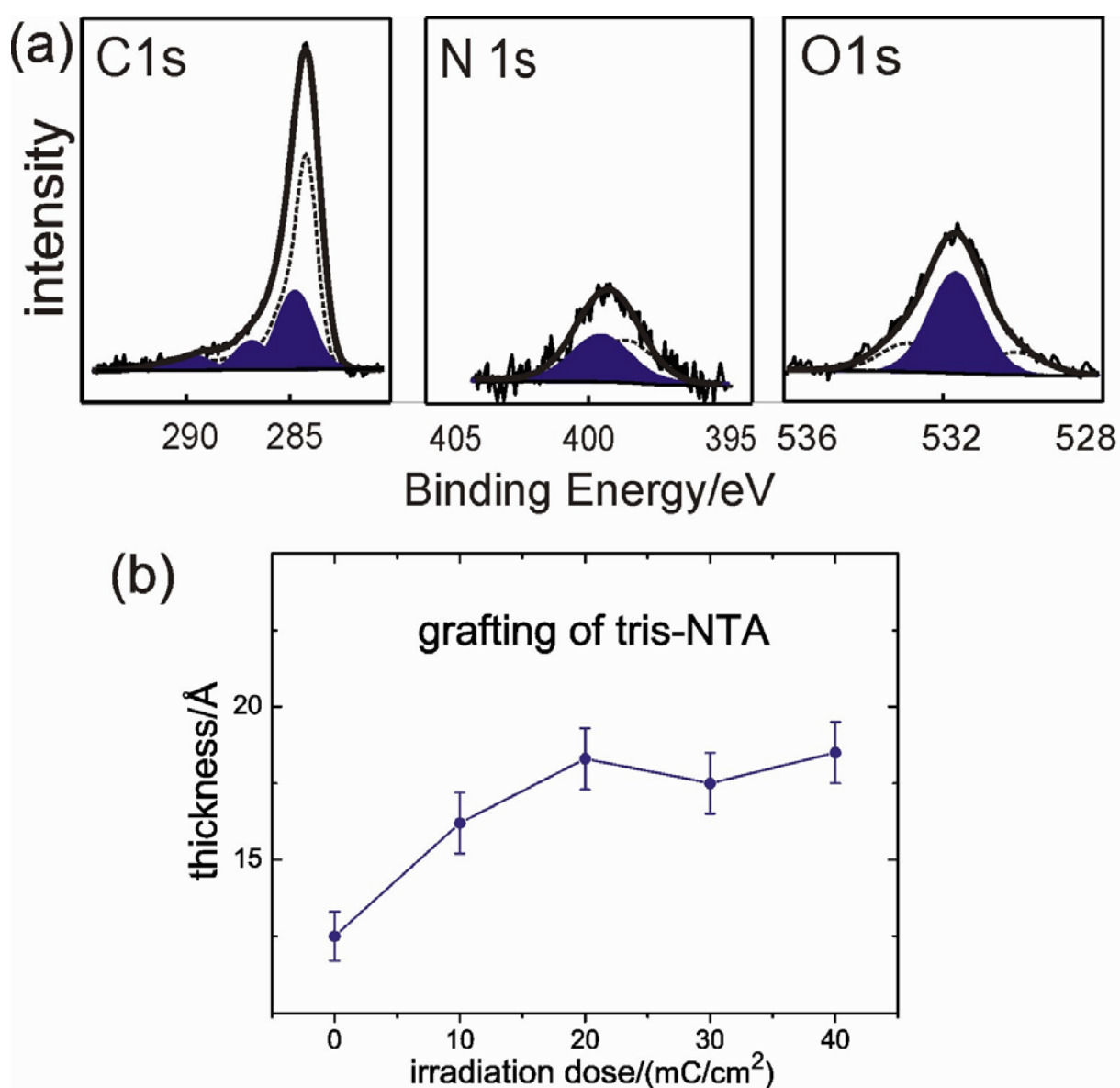


**Fig.6-3.** Grafting of the multivalent chelator on the amino terminated surface of the irradiated NBPT SAM (30 mC/cm<sup>2</sup>). (a) A detailed fit of the XPS data. (b) Electron dose dependent thickness of the grafted monolayer.

### 3- AFM Measurements:

The spectroscopic study of these elemental steps during protein chip fabrication confirms the efficiency of the presented new concept. We thus generated patterns with  $\sim 1 \mu\text{m}$  circles by electron beam lithography in NBPT SAMs. All protein chip assembly steps were followed by AFM. We further studied the dependency of the chip assembly on the applied electron dose. In agreement with the XPS data, the best topographic characteristics of the fabricated chips are achieved for electron doses from 20 to 40  $\text{mC}/\text{cm}^2$ . The spectroscopic study of these elemental steps during protein chip fabrication confirms the efficiency of the presented new concept. We thus generated patterns with An AFM image of the protein chip, Scheme 1a (iv), under physiological conditions is shown in Fig.6-4a. In the topography image, areas with coupled multivalent chelators are recognized as bright spots with a height of  $\sim 1 \text{ nm}$  in comparison to areas of the protein repellent EG3-OH thiol SAM. For demonstration of the protein chip functionality we employed the barrel-shaped 20S proteasome complex as a biological model system. This macromolecular protein complex has lateral dimensions of  $11 \times 15 \text{ nm}^2$  and can be easily detected by AFM<sup>[62]</sup>. Fig.6-4b shows a microarray of specifically immobilized His<sub>6</sub>-tagged proteasome complexes on the chip surface. Here, the His<sub>6</sub>-tags of the proteins were engineered to result in an end-on orientation, Scheme 1a (v). The AFM data show specific and oriented immobilization of the proteins on the chip surface. The line profiles along the immobilized protein chip was regenerated by imidazole and re-used for immobilization of fluorescence-labelled His<sub>10</sub>-tagged maltose-binding protein (His<sub>10</sub>-MBP). The fluorescence pattern in Fig.6-5 obtained by confocal laser scanning microscopy demonstrates, in addition to the AFM results, a specific and homogenous protein microarray.

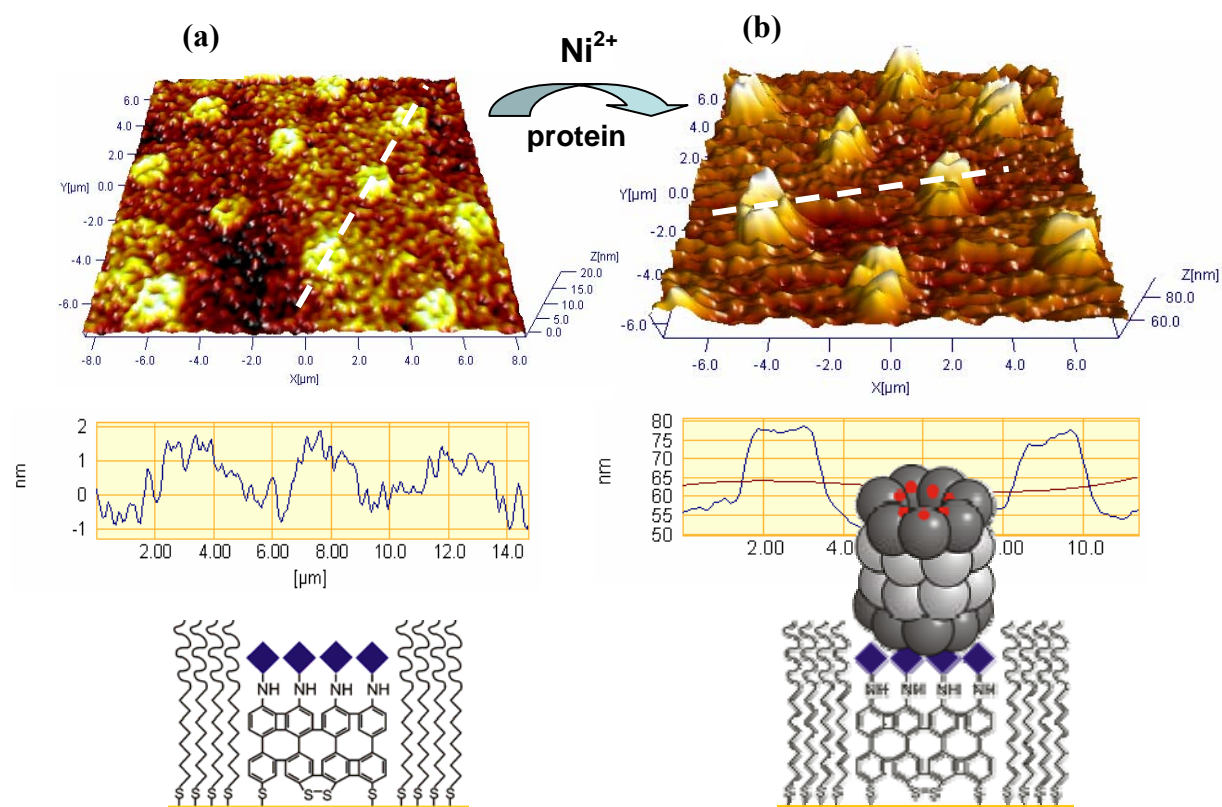


**Fig.6-4.** Controlled immobilization of proteins on the chip surface. (a) Topographic AFM image of the protein chip surface. (b) *In situ* AFM scan of an array of immobilized His<sub>6</sub>-proteasome complexes at micrometer scale.

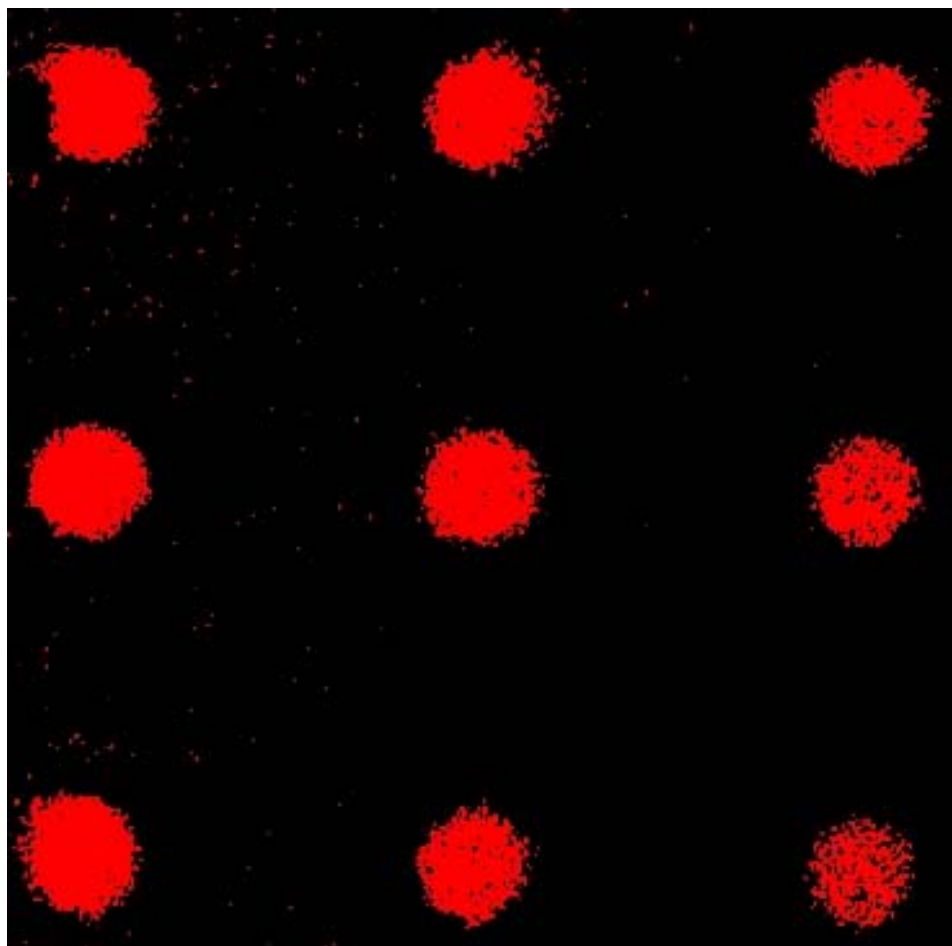


**Fig.6-5** Confocal laser scanning micrograph of specifically immobilized fluorescence-labelled proteins (His<sub>10</sub>-MBP) on the same chip surface.

In conclusion, we have introduced a methodology for the fabrication of protein chips based on the combination of electron beam lithography, molecular self-assembly principles, and biochemical tweezers for highly specific affinity capturing of His-tagged proteins. The functionality of the protein chips has been demonstrated by specific, homogeneous, oriented and reversible immobilization of His<sub>6</sub>-tagged proteins. The high affinity of the protein arrays is achieved by utilization of multivalent interactions in NTA/His-tag pairs. Since electron beam lithography is suitable to the fabrication of SAM nanostructures with lateral dimensions down to 10 nm, in outlook we suggest that this concept can be further developed for the function immobilization structured proteins arrays on solid substrates down to single molecular resolution.

## Summary

In this work, I have studied some characteristic and application of aromatic cross-linked self-assembled monolayers (SAMs). Aromatic Hydroxybiphenyl (HBP) SAMs can be cross-linked by e-beam irradiation and have been utilized as negative resist for e-beam patterning of silicon. I studied the sensitivity of HBP to e-beam irradiation. The necessary dose for complete cross linking of HBP was to be  $20\text{mC}/\text{cm}^2$ .

An extremely high thermal stability of electron cross-linked aromatic biphenyl derivative self-assembled monolayers (SAMs) is reported. Desorption of pristine Biphenylthiol SAMs occurs already at temperatures above 400K via C–S bond breaking and desorption thiolate. The pristine NBPT exhibit more stable than pristine BPT. Despite of similar bond cleavage in cross-linked SAMs, these remain on the surface up to 1000 K, which is the highest temperature reported for a SAM. Thermal processing of e-beam patterned biphenylthiol SAMs results in the fabrication of monomolecular pattern by selective thermal desorption. The reported results are not limited to the studied model system but can be extended to other aromatic SAM

One of the SAMs applications is the protein adsorption. We have introduced a methodology for the fabrication of protein chips based on the combination of electron beam lithography, molecular self-assembly principles, and biochemical tweezers for highly specific affinity capturing of His-tagged proteins. The functionality of the protein chips has been demonstrated by specific, homogeneous, oriented and reversible immobilization of His<sub>6</sub>-tagged proteins. The high affinity of the protein arrays is achieved by utilization of multivalent interactions in NTA/His-tag pairs. Since electron beam lithography is suitable to the fabrication of SAM nanostructures with lateral dimensions down to 10 nm, in outlook we suggest that this concept can be further developed for the function immobilization structured proteins arrays on solid substrates down to single molecular resolution.

**References :**

- (1) Smith, R.K.; Lewis, P.A.; Weiss, P.S., *Progress in Surface Science*, **75**, 1(2004).
- (2) Kesmodel, L.L.; Dubois, L.H.; Somorjai, G.A., *Chem. Phys. Lett.*, **56**, 267(1978).
- (3) Nuzzo, R.G.; Allara, D.L., *J am. Chem. Soc.*, **105**, 4481( 1983).
- (4) Sellers,H.; Ulman, A.; Shnidman,Y.; Eilers, J. E., *J. Am. Chem. Soc.* **115**,9389 (1993).
- (5) Tour, J. M.; Jones, L., II; Pearson, D.L.; Lamba, J. S.; Burgin, T.P.; Whitesides, G. M.; Allara, D. L.; Atre, S. V., *J. Am. Chem. Soc.*, **117**, 9529 (1995).
- (6) Dhirani, A.-A.; Zehner, W.; Hsung, R. P.; Guyot-Sionnest, P.; Sita, L., *J.Am. Chem. Soc.*, **118**, 3319(1996).
- (7) Tao, Y.-T.; Wu, C.-C.; Eu, J.-Y.; Lin, W.-L., *Langmuir*, **13**, 4018(1997).
- (8) Kang, J. F.; Jordan, R.; Ulman, A., *Langmuir*, **14**, 3983(1998).
- (9) Kang, J. F.; Liao, S.; Jordan, R.; Ulman, A., *J.Am. Chem. Soc.*, , **120**, 9662 (1998).
- (10) Himmel, H.-J.; Terfort, A.; Wöll, Ch., *J.Am. Chem. Soc.*,**120**, 12069 (1998).
- (11) Kang, J. F.; Ulman, A.,Liao, S.; Jordan, R.;Langmuir, **15**, 2095 (1999).
- (12) Ishida, T.; Choi, N.; Mizutani, W.; Tokumoto, H.; Kojima,I.; Azebara, H.; Hokari;; Akiba, U.; Fujihira, M., *Langmuir*, **15**, 6799 (1999).
- (13) Leung, T.Y. B.; Schwartz, P.; Scoles, G.; Schreiber, F.; Ulman. A., *Surf. Sci.*, **458**, 34 (2000).
- (14) Frey, S.; Stadler, V.; Heister, K.; Zharnikov, M.; Grunze, M.; Zeysing, B.; Terfort, A.; *Langmuir*, **17**, 2408(2001).
- (15) Ishida, T.; Mizutani, W.; Azebara, H.; Sato, F.; Choi, N.; Akiba, U.; Fujihira, M.,Tokumoto, H., *Langmuir*, **17**, 7459(2001).
- (16) Kang, J. F.; Ulman, A.,Liao, S.; Jordan, R.; Yang, G.; Liu,G.-Y.,*Langmuir*, **17**, 95 (2001).

- 
- (17) Fuxen, C.; Azzam, W.; Arnold, R.; Witte, G.; Terfort, A.; Wöll, Ch., *Langmuir*, **17**, 3689(2001).
- (18) Zharnikov, M.; Grunze, M., *J. Phys.: Condens. Matter*, **13**, 11333(2001).
- (19) Sabatani, E.; Cohen-Boulakia, J.; Bruening, M.; Rubinstein, I., *Langmuir*, **9**, 2974(1993).
- (20) Ulman, A., *Chem. Rev.*, **96**, 1533(1996).
- (21) Dulcey, C.S.; Georger, J.H.; Krauthamer, Jr. V.; Stenger, D.A.; Fare, T.L.; Calvert, J.M., *Science*, **252**, 551(1991).
- (22) Ada, E. T.; Hanley, L.; Etchin, S.; Melngailis, J.; Dressick, W.J.; Chen, M.S.; Calvert, J.M., *J. Vac. Sci. Technol.* **B 13**, 2189(1995).
- (23) Xia, Y.N., Whitesides, *Angew. Chem. Int. Ed. Engl.*, **37**,551(1998).
- (24) Perkins, F.K.; Dobisz, E.A.; Brandow, S.L.; Calvert, J.M., Kosakowski, J.E.; Marrian, C. R. K., *App. Phys. Lett.*, **68**, 550(1996).
- (25) Liu, G.Y.; Xu, S.; Cruchon-Dupeyrat, S., in *self-Assembled Monolayers of Thiols*, edited by Ulman, A., (Academic, San Diego, 1998), Vol. 24, pp. 81.
- (26) Lercel, M.J.; Whelan, C. S.; Craighead, H.G.; Seshadri, K.; Allara, D.L., *J. Vac. Sci. Technol.* **B 14**, 4085 (1996).
- (27) Lercel, M.J.; Craighead, H.G.; Parikh, A.N.; Seshadri, K.; Allara, D.L., *Appl. Phys. Lett.*, **68**, 1504(1996).
- (28) Harnett, C.K.; Satyalakshmi, K.M.; Craighead, H.G., *Appl. Phys. Lett.*, **76**, 2466(2000).
- (29) Götzhäuser, A.; Geyer, W.; Stadler, V.; Eck, W.; Grunze, M.; Edinger, K.; Weimann, Th.; Hinze, P., *J. Vac. Sci. Technol.* **B 18**, 3414 (2000).
- (30) Seshadri, K.; Froyd, K.; Parikh, A. N.; Allara, M.J.; Craighead, H.G., *J. Phys. Chem.*, **100**, 15900(1996).
- (31) Olsen, C.; Rowntree, P. A., *J. Chem. Phys.*, **108**, 3750(1998).
- (32) Zharnikov, M.; Geyer, W.; Götzhäuser, A.; Frey, S.; Grunze, M., *Phys. Chem. Chem. Phys.*, **1**, 3163(1999).

- (33) Lercel, M.L.; Redinbo, G.F.; Pardo, F.D.; Rooks, M.; Tiberio, R.C.; Simpson, P.; Craigheah, H.G.; Sheen, C.W.; Parikh, A.N.; Allara, D.L., *J. Vac. Sci. Technol.* **B 12**, 3663(1994).
- (34) David, C.; Müller, H.U.; Völkel, B.; Grounze, M., *Microelectron. Eng.*, **30**, 57(1996).
- (35) Geyer, W.; Stadler, V.; Eck, E.; Zharnikov, M.; Gölzhäuser, A.; and Grunze, M., *Appl. Phys. Lett.* **75**, 2401(1999).
- (36) Eck, W.; Stadler, V.; Geyer, W.; Zharnikov, M.; Gölzhäuser, A.; and Grunze, M., *Adv. Mater.*, **12**, 805(2000).
- (37) Xiao, X.; Hu, J.; Charych, D.H.; Salmeron, M., *Langmuir*, **12**, 235(1996).
- (38) Kim, H.I.; Graupe, M.; Oloba, O.; Koini, T.; Imaduddin, S.; Lee, T.R.; Perry, S.S., *Langmuir*, **15**, 3179(1999).
- (39) Scherer, J.; Vogt, M.R.; Magnussen, O.M.; Behm, R.J., *Langmuir*, **13**, 7045(1997).
- (40) Jennings, G.K.; Laibinis, P.E.; *Colloids Surf. A* **11**, 105(1996).
- (41) Ishibashia, M.; Itoh, M.; Nishihara, H.; Aramaki, K., *Electrochim. Acta*, **41**, 241(1996).
- (42) Zamborini, F.P.; Crookes, R.M., *Langmuir*, **14**, 3279(1998).
- (43) Feng, Y.; Teo, W.-K.; Siow, K.-S.; Gso, Z.; Tan, K.-L.; Hsieh, A.-K., *Electrochem. Soc.*, **144**, 55(1997).
- (44) Whitesides, G.M.; Laibinis, P.E., *Langmuir*, **6**, 87(1990).
- (45) Wenzl, I.; Yam, C.M.; Barriet, D.; Lee, T.R., *Langmuir*, **19**, 10217(2003).
- (46) Colorado, R. Jr.; Lee, T.R., *Langmuir*, **19**, 3288(2003).
- (47) Love, J.C.; Estroff, L.A.; Kriebel, J.K.; Nuzzo, R.G.; Whitesides, G.M., *Chem. Rev.*, (Washington, D.C.) **105**, 1103(2005).
- (48) Bain, C.D.; Troughton, E. B.; Tao, Y.-T.; Ewall, J.; Whitesides, G.M.; Nuzzo, R.; *J. Am. Chem. Soc.*, **111**, 321 (1989).
- (49) Kim, T.; Chan, K. C.; Crooks, R. M., *J. Am. Chem. Soc.* **119**, 186(1997).
- (50) Clegg, R. S.; Reed, S. M.; Hutchison, J. E., *J. Am. Chem. Soc.* **120**, 2486 (1998).

- 
- (51) Shon Y.-S.; Lee, T. R.; *J. Phys. Chem. B* **104**, 8192 (2000).
- (52) Jennings, G. K.; Laibinis, P. E.; *J. Am. Chem. Soc.* **119**, 5208 (1997).
- (53) Küller, A.; Eck, W.; Stadler, V.; Geyer, W.; Götzhäuser, A.; *Appl. Phys. Lett.* **82**, 3776 (2003).
- (54) Eck, W.; Küller, A.; Grunze, M.; Völkel, B.; Götzhäuser, A.; *Adv. Mater.*, **17**, 2583 (2005).
- (55) Biebricher, A.; Paul, A.; Tinnefeld, P.; Götzhäuser, A.; Sauer, M.; *J. Biotechnology* **112**, 97(2004).
- (56) Götzhäuser, A.; Eck, W.; Geyer, W.; Stadler, V.; Weimann, T.; Hinze, P.; Grunze, M.; *Adv. Mater.*, **13**, 806 (2001).
- (57) Geyer, W.; Stadler, V.; Eck, W.; Götzhäuser, A.; Grunze, M.; Sauer, M.; Weimann, T.; Hinze, P.; *J. Vac. Sci. Technol. B.* **19**, 2732(2001).
- (58) Schmelmer, U.; Jordan, R.; Geyer, W.; Eck, W.; Götzhäuser, A.; Grunze, M.; Ulman, A.; *Angewandte Chemie* **115**, 577 (2003).
- (59) Zhu, H.; Snyder, M.; *Curr. Opin. Chem. Biol.* **7**, 55 (2003).
- (60) Piehler, J.; Beuttler, M.; Guckenberger R.; Tampé, R.; *Nat. Nanotechn.* **2007**, in press.
- (61) Southern, E.; Mir, K.; Shchepinov, M.; *Nature Genet.* **21**, 5 (1999).
- (62) Tinazli, A.; Tang, J.; Valiokas, R.; Picuric, S.; Lata, S.; Piehler, J.; Liedberg, B.; Tampé, R.; *Chem. Eur. J.*, **11**, 5249 (2005).
- (63) Lata, S.; Reichel, A.; Brock, R.; Tampé, R.; Piehler, J.; *J. Am. Chem. Soc.*, **127**, 10205(2005).
- (64) Barr, T.L.; *Modern ESCA: The principles and practice of x-ray photoelectron spectroscopy*, CRC Press: Boca Raton, 1994.
- (65) Einstein, A.; *Ann. Phys.*, **17**, 132(1905).
- (66) Weimer, J.; *methods in Material Research: X-ray photoelectron spectroscopy*. (John Wiley and Sons Ltd, New York, NY, 2002).
- (67) Reilman, R.F.; Msezane, A.; Manson, S.T.; *J. Electron Spectrosc.*, **8**, 389(1976).
- (68) Scofield, J.H.; *J. Electron Spectrosc.*, **8**, 129(1976).

- (69) Ertl, G.; Küppers, J.; "Low energy electrons and surface chemistry", VCH Verlagsgesellschaft mbH: Weinheim, 1985.
- (70) Binnig, G.; Quate, C.F.; Gerber, C.H., *Phys. Rev. Lett.*, **56**, 930 (1986).
- (71) Drake B.; Prater C.B.; Weisenhorn A.L.; Gould S.A.C.; Albercht, T.R.; Quate C.F.; Cannel, D.S.; Hansma, H.G.; Hansma, P.; *Science*, **243**, 1586, (1989).
- (72) Hansma, P.K.; Cleveland J.P.; Radmacher, M.; Walters, D.A.; Hillner, P.E.; Bezanilla, M.; Fritz, M.; Vie, D.; Hansma, H.G.; Prater, C.B.; Massie, J.; Fukunaga, L.; Gurley, J.; Elings, V.; *Appl. Phys. Lett.*, **64**, 1738, (1994).
- (73) Muller, D.J.; Schabert, F.A.; Buldt, G.; Engel, A., *J. Biophys.*, **86**, 1681 (1995).
- (74) Putman, C.A.J.; Vanderwerf, K.O.; Degrooth, B.G.; Vanhulst, N.F.; Greve, J., *Appl. Phys. Lett.*, **64**, 2454 (1994).
- (75) Butt, H.J., *J. Biophys.*, **60**, 1438, (1991).
- (76) Shao, Z.; Yang, J., *Q. rev. Biophys.*, **28**, 195 (1995).
- (77) Rugar, D.; and Hansma, P.K., *Phys. Today*, **43**, 23 (1990).
- (78) Richard, B.C.; Evans, C. A.; Wilson, S. Jr.m, "Encyclopedia of materials characterization", *Surfaces, Interfaces, thin film*.
- (79) Aebi, U.; Pollard, T.D., *J. Electron Microsc. Tech.* **7**, 33 (1987).
- (80) NIST X-ray photoelectron spectroscopy Database 20, (Version 3.4, Web Version, 2003).
- (81) Sherwood, P.M.A., "Practical Surface Analysis, Auger and X-ray Photoelectron Spectroscopy, 2<sup>nd</sup> ed", Wiley, New York 1991.
- (82) Canster D.g., Hinds, K.; Grainger, D.W., *Langmuir*, **12**, 5083 (1996).
- (83) Ishida, T.; Hara, M.; Kojima, I.; Tsuneda, S.; Nishida, N.; Sasabe, H.; Knoll, W., *Langmuir*, **14**, 2092 (1998).
- (84) Heister, K.; Zharnikov, M.; Grunze, M.; Johanson, L.S.O., *J. Phys. Chem. B*, **105**, 4058 (2001).
- (85) Ishida, T.; Choi, N.; Mizutani, W.; Tokumoto, H.; Kojima, I.; Azebara, H.; Akiba, U.; Hokari, H.; Fujihira, M., *Langmuir*, **15**, 6799 (1999).

- 
- (86) Schoenfish, M. H.; Pemberton, J. E., *J. Am. Chem. Soc.*, **120**, 4502(1998).
- (87) Frey, S.; Rong, H.-T.; Heister, K.; Yang, Y.-J.; Buck, M.; Zharnikov, M., *Langmuir*, **18**, 3142(2002).
- (88) Bierbaum, k.; Kinzler, M.; Wöll, C.; Grunz, M.; Hähner, G.; Heid, S.; Effenberger, F., *Langmuir*, **11**, 512(1995).
- (89) Pashutski, A.; Folman, M., *Surface Science*, **216**,395(1989).
- (90) Wagner, A. J.; Han, K.; Vaught, A. L.; Fairbrother, D. H., *J. Phys. Chem. B* **104**, 3291(2000).
- (91) Heister, K.; Zharnikov, M.; Grunze, M.; Johansson L. S. O.; Ulman, A. *Langmuir*, **17**, 8(2001).
- (92) Rieke, P. C.; Baer, D. R.; Fryxell, G. E.; Engelhard M. H.; Porter, M. S., *J. Vac. Sci. Technol. A* **11**, 2292(1993).
- (93) Frydman, E.; Cohen, H.; Maoz, R.; Sagiv, J.; *Langmuir* ,**13**,5089(1997).
- (94) Moon, J. H.; Kim, K-J.; Kang, T-H.; Kim, B.; Kang, H.; Park, J. W., *Langmuir*, **14**, 5673(1998).
- (95) La, Y-H.; Kim, H. J.; Maeng, I. S.; Jung, Y. J.; Park, J. W., *Langmuir*, **18**, 301(2002).
- (96) La, Y-H.; Kim, H. J.; Maeng, I. S.; Jung, Y. J.; Park, J. W., *Langmuir* **18**, 2430(2002).
- (97) Laibinis, P. E.; Graham, R. L.; Biebuyck, H. A.; Whitesides, G. M., *Science* **254**, 981(1991).
- (98) Zharnikov, M.; Grunze, M., *J. Vac. Sci. Technol. B* **20**, 1793(2002).
- (99) Yang, X. M.; Peters, R. D.; Kim, T. K.; Nealey, P. F.; Brandow, S. L.; Chen, M-S.; Shirley, L. M.; Dressick, W. K., *Langmuir*, **17**, 228(2001).
- (100) Han, S.W.; Lee, I.; Kim, K., *Langmuir*,**18**,182(2002).
- (101) Mendes, P. M.; Chen, Yu; Palmer, R.E.; Nikitin, K.; Fitzmaurice, D.; Preece, J. A., *J.Phys.:Condens. Matter.*, **15**, S3047(2003).
- (102) Hochuli, E., *Genet. Eng.*, **12**, 87 (1990).

- 
- (103) Turchanin, A.; El-Desawy M.; Götzhäuser, A., *Appl. Phys. Lett.*, **90**, 053102. (2007).
- (104) Harder, P.; Grunze, M.; Dahint, R.; Whitesides, G.M.; Laibinis, P. E., *J. Phys. Chem. B*, **102**, 426(1998).
- (105) *Surface Analyses by Auger and X-ray Photoelectron Spectroscopy*, ed. D. Briggs and J.T. Grant (Surface Spectra Limited, Chichester, 2003).

## Acknowledgement

I wish to express my deepest thanks to my supervisor Prof. Dr. Armin Gölzhäuser for his kind invitation to attend his group, the providing of interest research topic, financial support and helpful discussion. Without his patience, encouragement and all the helps, I would not have come so far in my Ph.D.

I would like to express my gratitude and appreciation to Dr. Andrey Turchanin. This thesis would not have been possible without him. He was the driving force behind the ideas for this work and for his great efforts for suggesting and his valuable guidance and illuminating discussions.

I would like to thank Dr. Berthold völkel for providing me all material which I need and many useful discussions.

Special thanks to Dr. Alexander Küller who the first person learning me how to prepare the SAMs and for his useful discussions.

I would like to thank Dr. André Beyer for helping me correcting the thesis.

I would like to thank our secretary Mrs. Ursula Lorentzen for her helping and her advices.

My thanks to my colleagues, Christoph T. Nottbohm, Dirk Weber, Ihsan Amin, Dr. Laxman Kankate, Nils Mellech, Heiko Muzik, Mark Schnietz, Henning Vieker, and Xianghui Zhang for their helping and shared good times with them. I wish you all the best and wonderful life.